

Nanomechanics and scanning probe microscopy with nanowires

Inauguraldissertation

zur

Erlangung der Würde eines Doktors der Philosophie

vorgelegt der

Philosophisch-Naturwissenschaftlichen Fakultät
der Universität Basel

von

Davide Cadeddu

aus Mailand, Italien

Basel, 2018

Genehmigt von der Philosophisch-Naturwissenschaftlichen Fakultät
auf Antrag von

Prof. Dr. Martino Poggio

Prof. Dr. Christian Degen

Basel, den 27/2/2018

Prof. Dr. Martin Spiess
Dekan

*We do what we must
because we can.*

Contents

Introduction	v
1 Nanomechanics	3
1.1 Introduction	3
1.2 Euler-Bernoulli Beam equation	3
1.2.1 Lagrangian of motion	3
1.3 Planar motion	5
1.3.1 Strain-curvature relation	5
1.3.2 Free vibration	7
1.4 Third order terms	10
1.4.1 Inextensional beam	10
1.4.2 Nonlinear equation of motion	11
1.4.3 Frequency response	14
1.5 Orthogonal flexural modes	15
1.5.1 System rotation	15
1.5.2 Lagrangian of motion	17
1.5.3 Nonlinear equations of motion	18
1.5.4 Adimensional equations	21
2 Nanowires Nanomechanics	25
2.1 Introduction	25
2.2 GaAs Nanowires	25
2.3 Displacement detection	26
2.3.1 Introduction	26
2.3.2 Optical fiber interferometer	27
2.4 Experimental results	29
2.4.1 Setup	29
2.4.2 Linear and nonlinear response	30
2.4.3 Mechanical Mixing	32
2.4.4 Mode Coupling	34
2.4.5 Mode coupling in the time domain	36
2.4.6 Frequency swept Pump-probe measurements	37

2.4.7	Amplitude swept Pump-probe measurements	39
2.5	Mechanical Logic	40
2.6	Vectorial scanning with GaAs nanowires	41
2.6.1	Introduction	41
2.6.2	Two-mode scanning probe microscopy	43
2.7	Coherent dynamics in a NW	44
3	Optomechanics with photonic wires	49
3.1	Introduction	49
3.2	Photonic Trumpet	49
3.3	Experimental Results	51
3.3.1	Resonant spectroscopy of a QD coupled to a mechanical resonator	51
3.3.2	Resonance Fluorescence noise spectrum	53
3.3.3	FEM simulations	55
3.3.4	Auto-correlation function	56
3.3.5	Quantum dot position determination	57
3.3.6	Measurement on a second QD	59
3.4	Discussion	60
4	Fiber-coupled QD	65
4.1	Introduction	65
4.2	Fabrication	67
4.3	Characterization	67
4.3.1	Discussion	70
4.3.2	Potential applications	71
4.4	Electric Field sensing with QDs	72
4.4.1	Setup	72
4.4.2	FEM Simulations	74
4.4.3	2D mapping of local Electric Field	76
4.4.4	Optimal wire geometry for sensing	80
4.4.5	Discussion	81
5	Conclusion and Outlook	85
A	Appendix A	91
A.1	Dielectric wire in uniform field	91
A.1.1	$E_0 \perp z$	91
A.1.2	$E_0 \parallel z$	92
A.2	General case	94
B	Appendix B	95
B.1	6 axis scanning NWs Microscope	95

References	95
Curriculum Vitae	115
Acknowledgments	117

Introduction

In the last few years, nanowires (NWs) gathered more and more interest in an incredible variety of scientific and technologic applications. Due to their versatility and unique characteristics NWs are considered key in new generation electronic and energy harvesting devices, study of quantum effects, and sensing.

In particular, self-assembled NW crystals have emerged as particularly promising mechanical transducers. They can be grown into nearly defect-free nanomechanical resonators with exceptional properties, including small motional mass and low dissipation. Near structural perfection results in low mechanical dissipation and therefore high thermally limited force sensitivity. Additionally, their small motional mass both enables the detection of atomic-scale adsorbates and results in relatively high mechanical resonance frequencies, decoupling the resonators from common sources of noise, and should permit improved sensitivity in mass-sensing and scanning probe applications [1–4]. When brought close to a surface, NWs experience extremely low non-contact friction [5] making near-surface ($< 100\text{nm}$) force sensitivities around $1 \text{ aN} / \sqrt{\text{Hz}}$. As a result, NWs have been used as force transducers in nuclear magnetic resonance force microscopy [2] and may be amenable to other ultrasensitive microscopies such as Kelvin probe force microscopy [6] or for the spectroscopy of small friction forces [7].

Moreover, advances in the control of growth and lithography processes allow NWs to be grown as heterostructures, which makes them a very practical monolithic platform for studies of nanoscale hybrid systems. Different materials and/or diverse crystalline structures can be used in radial and axial heterostructures giving total control of the properties and functionalities of the NWs. Under particular growth conditions, for example, self assembled quantum dots (QDs) can be embedded in semiconductor NWs creating an optimal system candidates for quantum photonics applications such as single photon sources and nano-sensing.

Semiconductor QDs are of particular interest due to their excellent qualities as single photon emitters such as high brightness, narrow emission lines and high fidelity anti-bunching. These properties combine well with the unique one dimensional structure and high refractive index of semiconductor

NWs that naturally facilitates low loss optical waveguiding, resulting in a single system very attractive as single photon source.

Additionally, it has been recently demonstrated how the optical transitions of an embedded QD is intrinsically coupled to the motion of the hosting NW through strain [8, 9]. Coupling a nano-scale quantum system to a microscopic mechanical resonator offers a new degree of freedom with potential applications in precision sensing and quantum information [10]. On the one hand, the mechanical resonator can be controlled via the quantum system, enabling “phonon lasing” [11, 12] or cooling towards the mechanical ground state [11, 13]. On the other hand, the quantum system can be controlled via the mechanical system, offering the perspective of non-demolition read-out via a precise measurement of the oscillator’s position [12] and applications in precision sensing.

With this thesis, we aim to study and exploit some of the features that make NWs extremely interesting for scanning probe experiments. We begin studying the dynamics of as-grown GaAs NWs, observing that for already moderate driving amplitudes their motion stops to be linear and follows the dynamics of a Duffing oscillator instead. Conventionally, in scanning probe experiments oscillatory motion of the cantilever is driven with amplitudes small enough to remain in the linear dynamical regime. However this linear dynamic range is often quite limited in nanoscale oscillators [14–16] due to a number of reasons [17, 18], including the resonator geometry, nonlinear damping [19, 20], the presence of external potentials, and nonlinear boundary conditions [21, 22]. While the nonlinear dynamics occurring when this range is exceeded complicate the analysis of sensing experiments and are therefore generally avoided or compensated for [23], nonlinearities can also give rise to a host of useful effects, such as signal amplification [24, 25], noise squeezing [26], and frequency mixing [27]. We proceed to prove how the nonlinear dynamics of NW cantilevers can enable some of these effects at the nanoscale in mechanical form and have the potential to enhance the performance of cantilever-based sensors.

Thereafter, we observe how a small asymmetry in the cross section of these NWs splits the flexural modes into orthogonal doublets nearly degenerate in frequency. When the NW is scanned over a sample in the pendulum geometry, these modes can be used for the simultaneous detection of in-plane forces and spatial force derivatives along two orthogonal directions [28] enabling the investigation of inherently 2D effects, such as the anisotropy or non-conservative character of specific interaction forces. We then provide evidence of the coupling of these modes when driven in the nonlinear regime showing how the frequency of one mode becomes dependent on the amplitude of the other following a quadratic behaviour. The coupling of mechanical modes has various applications including in frequency and am-

plitude modulation [29], improving mechanical quality factors [30], in several parametric amplification schemes, and in the implementation of mechanical logic [31,32]. Mode coupling may also be used in the enhancement of mechanically detected mass, charge and force sensitivity [28,33]. For these reasons, such coupling has been studied in numerous top-down fabricated nanomechanical systems, including single [34,35] and double beam structures [29,36] and membranes [37,38]. In one example, grown carbon nanotubes have been observed to exhibit coupling between flexural modes of different orders [39]. But these modes are not perpendicular to each other, nor are such nanotubes usable as singly-clamped cantilever force transducers. Although orthogonal modes have been observed in grown NWs, [1, 28], coupling has not been demonstrated or put to use before.

Next, we study the strain mediated coupling in a nanowire hybrid system. The hybrid system studied here consists of a GaAs photonic wire and a semiconductor QD embedded close to its clamping point. We demonstrate the resonant optical driving of the QD transition in such a structure. The noise spectrum of the resonance fluorescence signal, recorded in the single-photon counting regime, reveals a coupling to mechanical modes of different types. We measure a sensitivity to displacement of $65 \text{ fm}/\sqrt{\text{Hz}}$ limited by charge noise in the device. Finally, we use thermal excitation of the different modes to determine the location of the QD within the wire.

This coupling, however, also provides an extra channel of dephasing for the QD emission, effectively reducing the appeal of this system as a reliable single photon source. Our idea has been to develop a new device, capable of limiting the dephasing and at the same time taking advantage of the design of the photonic wire, eliminating completely the need of complex optical setups for the photon collection. By means of micromanipulators we proceed to directly connect the facet of a photonic wire to the core of a single mode optical fiber essentially producing a QD fiber-pigtail. We demonstrate a photon collection efficiency at the output of the fiber of 5.8% and suggest realistic improvements for the implementation of a useful device in the context of quantum information.

The photonic wire provides another crucial feature to this configuration: positioning a sensitive element such as a QD at the end of a sharp tip, combined with a direct coupling to the optical fiber, opens the gates for applications in scanning probe experiments. We will then proceed to demonstrate how this device can be directly translated into a sensor for local electric fields. Many techniques have already established themselves as sensitive electric field detectors capable of reaching sub-elementary charge sensitivity and sub-nanometer spatial resolution such as electrostatic force microscopy (EFM) [40, 41], scanning Kelvin probe force microscopy (KPFM) [42], sensing based on nitrogen-vacancy centers in diamond [43], and scanning single

electron transistors (SETs) [44, 45]. More recently a new technique has been developed which uses a noncontact atomic force and scanning tunneling microscope (STM) functionalized with a single molecule to image the dipole field of an adatom on a surface [46] that is, effectively, the first demonstration of scanning QD microscopy (SQDM). With this technique it is possible to produce three-dimensional images of the local electrostatic potential with subnanometer resolution by recording single-electron charging events of a molecular QD. However this technique remains fragile due to its reliance on a single molecule and, in addition, is limited to STM conditions of ultra-high vacuum. An electric field sensor based on an optically addressable QD, on the other hand, has not been realized before. In this thesis we provide the proof-of-principle of such a device. Our first results encourage future experiments in this direction, suggesting direct improvements to our device that could eventually lead to reach a sensitivity comparable with scanning SETs, that still remain the most sensitive devices available yet. However, scanning SETs typically operate below 1 kHz due to the high intrinsic resistance of the SET and the capacitive load of the leads. This slow operation speed also exposes the sensor to $1/f$ charge noise which limits its sensitivity to $10^{-4} e/\sqrt{\text{Hz}}$ within 100 nm of the probe [47]. Our device, instead, would grant a much wider bandwidth, up to 1 GHz, only limited by the emission rate of the QD.

Thesis Outline

Chapter 1 introduces general nanomechanics background necessary to understand the motion of a cantilevered beam. Starting from the most simple case and moving to the more complex situation where the equations of motion become nonlinear and the flexural modes cannot be considered independent anymore.

Chapter 2 shows experimental evidence of the theory developed in the first chapter and shows possible applications of the implications for GaAs NWs. Starting from inducing and detecting Duffing nonlinearities in the motion of the NWs to see evidence of mode coupling in time dependent ringdown experiments. Last, we present an application for the NWs as vectorial scanning force sensors.

Chapter 3 moves the focus to the strain-mediated coupling between the thermal motion of tapered NWs and the emission of embedded quantum dots. With the help of finite element simulations, we are able to locate the position of each dot within the cross-section of the wire.

Chapter 4 describes the implementation of a compact and robust fiber-coupled single photon source and the proof of principle of an application as a

scanning probe for electric field sensing. Last, we suggest possible optimization of the geometry of the wire based on the screening effect of the field at the dot position as a consequence of the shape and composition of our probe. **Chapter 5** provides the conclusion of the thesis reporting the main results and giving an outlook for improvements of the future experiments inspired by this work.

1 | Nanomechanics

1.1 Introduction

In this chapter we derive the equations of motion and the frequency response of a single driven damped cantilever beam. We start from the Euler-Bernoulli free vibration equation describing the mode shape and time evolution of the oscillation of the beam and arrive at the end to describe the nonlinear flexural-flexural vibrations of the beam following the approach used by Crespo da Silva and Glynn [48, 49].

1.2 Euler-Bernoulli Beam equation

We start considering a cantilever beam undergoing small displacement. In this case we can refer to the Euler-Bernoulli beam theory to describe its motion. The theory, put together around 1750 by Leonhard Euler and Daniel Bernoulli, treats the case of a beam undergoing small deflection subjected to small lateral loads, allowing us to neglect effects of warping and shear deformation.

We consider a straight and uniform beam with length L and mass per unit length m with a cross sectional area $A = h_d b_d$. A schematic of the beam is shown in Fig.1.1. Additionally to the inertial (x, y, z) coordinate system, we can define a new local coordinate system (ξ, η, ζ) at arclength s where the axis ξ and η are always along the main directions of the cross section as shown in the inset in Fig.1.1. Here z and ζ are representing the neutral axis of the beam before and after the displacement, respectively. In general, each cross section of the beam undergoes an elastic displacement and a rotation.

1.2.1 Lagrangian of motion

Hamilton's principle [50] states that, of all the varied paths satisfying the prescribed initial and final configurations, the true evolution of the system extremizes the action functional $I = \int_{t_1}^{t_2} \mathcal{L} dt$ where t_1 and t_2 denote the initial and final time instants. By also including the work done by non-conservative

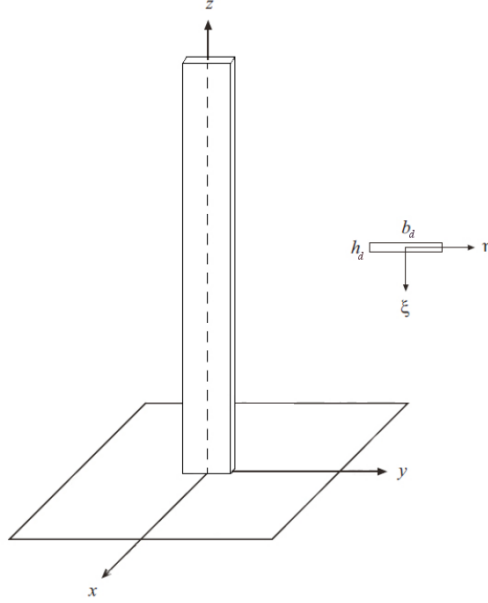


Figure 1.1 | A single clamped beam of length L and cross-sectional area A aligned along the z axis.

forces within the integrand, we get the extended Hamilton principle. Using the variation of the functional I and the fact that the variation and integral operators commute, we can write for the actual path:

$$\delta I = \int_{t_1}^{t_2} (\delta \mathcal{L} + \delta W_{nc}) dt = 0, \quad (1.1)$$

where \mathcal{L} is the Lagrangian of the system and W_{nc} denotes the work done by non-conservative forces, such as damping, external forces and moments. The Lagrangian \mathcal{L} is defined as:

$$\mathcal{L} \equiv T_k - V_p = \int_0^L \ell ds, \quad (1.2)$$

where T_k is the total kinetic energy, V_p is the potential energy, and we define ℓ as the specific Lagrangian. The total kinetic energy is composed of the sum of a translational and a rotational part. If we consider beam whose torsional rigidity is relatively higher than the flexural rigidity (true for long beams with near square or near circular cross sections like the nanowires used in our experiments), then the rotational contribution is negligible.

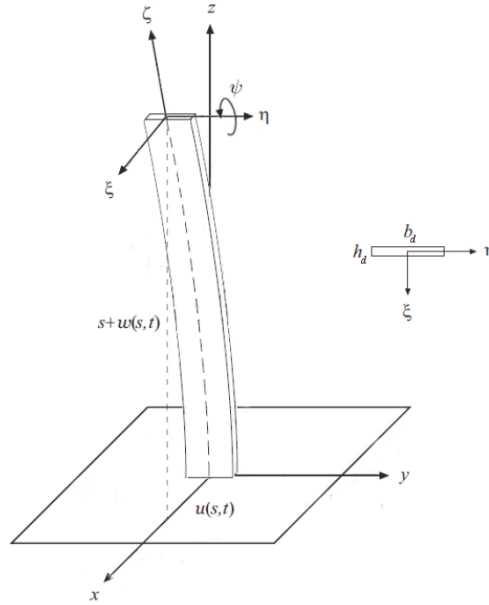


Figure 1.2 | Cantilever beam flexural vibration in the xz plane.

1.3 Planar motion

If we first consider the simple case where the cantilever is free to oscillate only in the xz plane and/or when the applied load is only in the x direction, then the motion is described by the one dimensional displacement function $u(s, t)$ along the x axis where s indicates the coordinate along the neutral axis of the beam. We can write the translational kinetic part as:

$$T_k = \frac{1}{2} m \int_0^L \dot{u}^2 ds, \quad (1.3)$$

where the dot stands for the time derivative $\partial/\partial t$.

1.3.1 Strain-curvature relation

The potential energy of our system is given by the strain energy U . Deformations of the material due to relative displacements will produce strain inside our beam while rigid-body translations and rotations will not produce any strain. Next, we will derive an expression for the strain energy in our system in terms of the displacement. Strain is defined as a second-rank tensor of the form [51]:

$$\epsilon_{ij} = \frac{1}{2} \left(\frac{\partial u_i}{\partial r_j} + \frac{\partial u_j}{\partial r_i} \right), \quad (1.4)$$

where r_i $i = 1, 2, 3$ are the components of the position vector \mathbf{r} and $\mathbf{u} = \{u, v, w\}$. Note that strain is symmetric when the indices are reversed such as $\epsilon_{ij} = \epsilon_{ji}$. The diagonal elements ($i = j$) are called normal strains and they represent deformation for displacements along the same directions while the off-diagonal elements ($i \neq j$) are so called shear strain and they are mainly due to torsion. When external forces are applied, a deformation is produced and it will give rise to forces internal the material. These internal forces lead to the definition of stress tensor σ_{ij} which elements represent the forces per unit area acting locally on the surface of a volume element of the material in different directions. Note that the elements σ_{ij} can be negative or positive corresponding to compressive or tensile stress, respectively. For homogeneous and isotropic materials (like the ones treated in this thesis are assumed to be) the stress is related to the strain through the Young's modulus E_Y and the Poisson's ratio ν_P . Under our assumption that the deflection is small and only along x , the stress results almost entirely uniaxial along the z and the only non zero element of the tensor is σ_{33} . In this case the strain tensor assumes the diagonal form:

$$\epsilon_{ij} = \begin{bmatrix} -\nu_P \sigma_{33}/E_Y & 0 & 0 \\ 0 & -\nu_P \sigma_{33}/E_Y & 0 \\ 0 & 0 & \sigma_{33}/E_Y \end{bmatrix} \quad (1.5)$$

For the moment we are going to neglect the smaller Poisson effect in order to maintain a simple description of the strain so that, in first approximation, the strain energy can then be written as:

$$U = \frac{1}{2} \int_0^L \left(\iint_A \sigma_{33} \epsilon_{33} d\xi d\eta \right) ds. \quad (1.6)$$

Next, we note that the bending of the beam along the x direction can be described by just the displacement $u(s, t)$ and by a rotation around the η axis (in this case parallel to y) of an angle ψ , that, in the case of small angles accounted in the Euler-Bernoulli theory, can be expressed as $\psi = u'$, where the prime stands for the spatial derivative $\partial/\partial s$. We can relate the uniaxial strain with the curvature vector $\boldsymbol{\kappa}(s, t)$ of the beam and with the distance from the neutral axis and write an expression that in this simple case is $\epsilon_{33} = -\xi \kappa_\eta$, where $\kappa_\eta = \psi'$ is the component along η of the curvature. By consequence, we can also express the uniaxial strain as a function of the displacement as:

$$\epsilon_{33} = -\xi \frac{\partial^2 u}{\partial s^2}. \quad (1.7)$$

Given that $\sigma_{33} \approx E_Y \epsilon_{33}$ and substituting the expression obtained for the strain into Equation 1.6 we can write:

$$U = \frac{1}{2} \int_0^L \left(\iint_A E_Y \kappa_\eta^2 \xi^2 d\xi d\eta \right) ds, \quad (1.8)$$

and by using the fact that the curvature is not a function of ξ or η , we can reduce the Equation 1.8 to:

$$V_p = U = \frac{1}{2} \int_0^L D_\eta \kappa_\eta^2 ds, \quad (1.9)$$

where we defined the bending stiffness $D_\eta = E_Y I_\eta$, where $I_\eta = \iint_A \xi^2 d\xi d\eta$ is the the area moment of inertia relative to the η direction. In conclusion, we can write an expression for the specific Lagrangian, which is given by:

$$\ell = \frac{1}{2} m \dot{u}^2 - \frac{1}{2} D_\eta \kappa_\eta^2. \quad (1.10)$$

1.3.2 Free vibration

We now have an explicit expression for the specific Lagrangian function that describes our system in the most simple configuration. Let's, for the moment, not take into account non-conservative forces, meaning that there is no forcing of the system and we neglect the damping (granted that our resonator has a high quality factor Q). If we express the curvature in terms of the displacement u , then ℓ results to be function of \dot{u} and u'' , and the Euler-Lagrange equation is then given by:

$$-\frac{\partial}{\partial t} \frac{\partial \ell}{\partial \dot{u}} + \frac{\partial^2}{\partial s^2} \left(\frac{\partial \ell}{\partial u''} \right) = 0. \quad (1.11)$$

By substituting the expression of ℓ , we obtain then the following differential equation:

$$m \ddot{u} + D_\eta u'''' = 0, \quad (1.12)$$

with the following boundary conditions for the fixed and free end of the beam:

$$u(0, t) = 0; u'(0, t) = 0; u''(L, t) = 0; u'''(L, t) = 0. \quad (1.13)$$

The general solution for the displacement $u(s, t)$ can then be expressed as a sum of harmonic vibrations of the form:

$$u(s, t) = \sum_n u_n(s) e^{-i\omega_n t}, \quad (1.14)$$

Mode n	β_n	ω_n/ω_0
0	1.875	1.000
1	4.694	6.267
2	7.855	17.547
$n \geq 3$	$(n + 1/2)\pi$	$((n + 1/2)\pi/\beta_0)^2$

Table 1.1 | Values of β_n for the first few flexural modes with the corresponding eigenfrequencies normalized to ω_0 .

where each value of n corresponds to a different mode with a different oscillation frequency and different displacement profile u_n . The latter can be obtained by solving the equation:

$$D_\eta u_n'''' - m\omega_n^2 u_n = 0, \quad (1.15)$$

which solutions are in the form:

$$u_n(s) = A_1 \cos\left(\frac{\beta_n}{L}s\right) + A_2 \sin\left(\frac{\beta_n}{L}s\right) + A_3 \cosh\left(\frac{\beta_n}{L}s\right) + A_4 \sinh\left(\frac{\beta_n}{L}s\right), \quad (1.16)$$

where we define $\beta_n := L(m\omega_n^2/D_\eta)^{1/4}$.

With the boundary conditions found before, the frequencies are obtained solving

$$\cos \beta_n \cosh \beta_n + 1 = 0. \quad (1.17)$$

The first few roots with the respective relative frequencies are shown in the Table 1.1.

The mode shape for the n -th mode, which describe the spatial displacement of the neutral axis as a function of the arclength s , is given by:

$$u_n(s) = A_1 \left[\left(\cosh\left(\frac{\beta_n}{L}s\right) - \cos\left(\frac{\beta_n}{L}s\right) \right) + \frac{\cos \beta_n + \cosh \beta_n}{\sin \beta_n + \sinh \beta_n} \left(\sin\left(\frac{\beta_n}{L}s\right) - \sinh\left(\frac{\beta_n}{L}s\right) \right) \right]. \quad (1.18)$$

The profile of the oscillation amplitude for the first 3 modes is plotted in Fig. 1.3.

Last, it is important to note that the exact same derivation can be made for the displacement v when the oscillation is happening only along the y

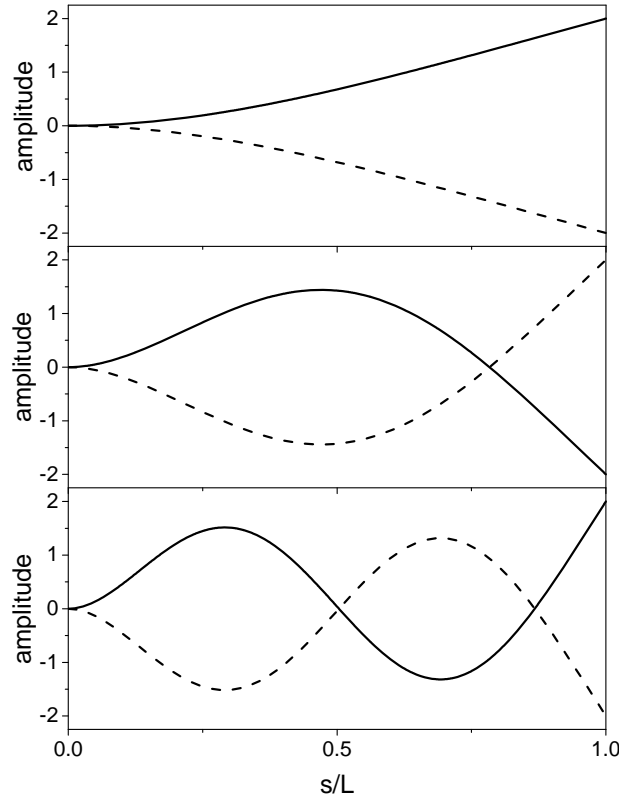


Figure 1.3 | Amplitude of oscillation u_n as a function of the normalized arclength for the first three flexural modes of a cantilever.

direction. In this case, the bending will be described by an angle θ around the x axis (that would be parallel with ξ in this case) with the only difference that a positive counterclockwise angle will produce a negative displacement (along the negative y axis). When the cross section is not symmetric, the mode shape will anyway be the same in both direction, while the frequency will be different, as it depends on the bending stiffness which depends itself on the geometry of the cross section. As an example, for the case of a rectangular cross section, we obtain $I_\eta = b_d h_d^3/12$ and $I_\xi = b_d^3 h_d/12$ for the motion along the x and y respectively. We can then calculate the the corresponding frequencies that are given by:

$$\omega_{n,x} = \beta_n^2 \sqrt{\frac{E_Y A h_d}{12m L^2}}, \quad (1.19)$$

$$\omega_{n,y} = \beta_n^2 \sqrt{\frac{E_Y A b_d}{12m L^2}}. \quad (1.20)$$

From 1.20 results clear that if $h_d < b_d$ then $\omega_{n,x} < \omega_{n,y}$. Instead, in the case

of any symmetric cross-section around the center, the moments of area I_ξ and I_η are equal and, by consequence, the frequencies are doubly degenerate. Also, the direction of oscillation will result completely arbitrary. That is true also for a circular cross-section and for the specific case of a regular hexagonal cross-section, as the one of the nanowires investigated in Chapter 2. In this case $I_\xi = I_\eta = 5\sqrt{3}/16h_d^4$ and the frequencies result:

$$\omega_n = \beta_n^2 \sqrt{\frac{5E_Y A h_d}{24m L^2}}. \quad (1.21)$$

In reality, however, it is impossible to have a true symmetric cross-section, as small asymmetries are inevitable. Even a very small asymmetry will lift the degeneracy and the modes in the two orthogonal directions will have a different spectral signature.

1.4 Third order terms

In this section we will start considering what happens when the amplitude of displacement cannot be considered small anymore. We will relax some of our assumptions and see how the motion of the beam can be described with a third order equation. If we would proceed in the same way as the previous section, we would obtain differential equations valid for an arbitrarily large displacement as long as the strain remains small. However, the boundary-value problem does not grant a closed-form solution as the equations become transcendental. We will instead expand the nonlinear terms in polynomials of third order.

For simplicity, we will now still consider the motion only along the direction x and only consider the most general case in the next section.

1.4.1 Inextensional beam

When the displacement of the beam becomes moderate, then angle of bending cannot be considered small anymore and our approximation $\psi \approx u'$ is no longer valid. We have to write the full expression considering that the bending will also produce a displacement w in the z direction. From the geometry of the problem (see also Fig.1.4 as a reference) we can write:

$$\tan \psi = \frac{u'}{1 + w'}. \quad (1.22)$$

Since we assume that our beam is inextensible (assumption that would not be valid of course for a doubly clamped beam), the displacements on the plane are related. To find this relation we look at the deformation of an

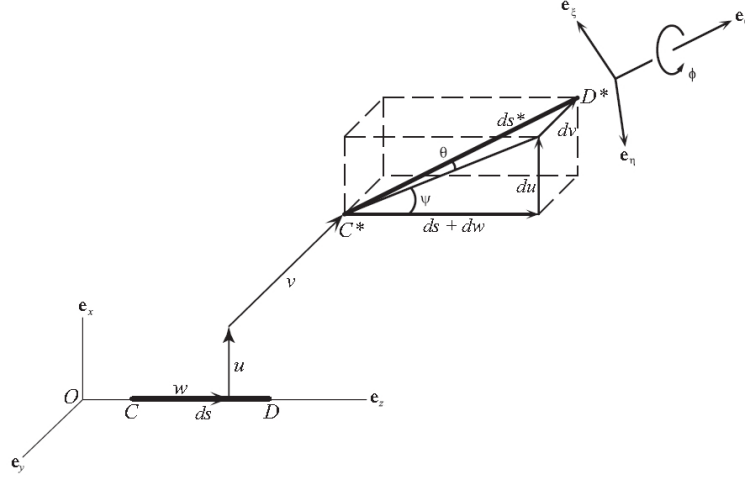


Figure 1.4 | A segment of the neutral axis \mathbf{CD} moves to $\mathbf{C}^*\mathbf{D}^*$ upon deformation. By imposing no strain on the neutral axis we can find a relation between the displacements in order to satisfy the assumption of inextensibility of the beam.

element \mathbf{CD} of the neutral axis of length ds and located at a distance s from the origin O of the (x, y, z) system. Upon deformation, \mathbf{CD} moves to $\mathbf{C}^*\mathbf{D}^*$ with displacement components (u, v, w) and $(u + du, v + dv, w + dw)$ for \mathbf{C} and \mathbf{D} respectively. The strain at point \mathbf{C} can then be calculated as:

$$\epsilon_s = \frac{ds^* - ds}{ds} = \sqrt{u' + v' + (1 + w')^2} - 1. \quad (1.23)$$

The requirement of the neutral axis to be inextensible implies that there is no strain so we can set $\epsilon_s = 0$. Since, for the moment, we are not considering deformation in the y direction, the inextensibility constraint equation reduces to:

$$u'^2 + (1 + w')^2 = 1. \quad (1.24)$$

To include the inextensibility constraint in the Lagrangian of motion, we utilize a Lagrangian multiplier $\lambda_L(s, t)$. This multiplier can be interpreted as an axial force necessary to keep the neutral axis inextensible.

1.4.2 Nonlinear equation of motion

While the expression for the potential energy stays unvaried from the previous case, we need to include also the contribution of the displacement w in the kinetic part, resulting in:

$$T_k = \frac{1}{2}m \int_0^L (\dot{u}^2 + \dot{w}^2) ds. \quad (1.25)$$

The specific Lagrangian can be written then in the explicit form:

$$\ell = \frac{1}{2}m(\dot{u}^2 + \dot{w}^2) - \frac{1}{2}D_\eta \kappa_\eta^2 + \frac{1}{2}\lambda_L[1 - u'^2 - (1 + w'^2)]. \quad (1.26)$$

Note that the specific Lagrangian is a function of x_i where $\mathbf{x} = \{\dot{u}, \dot{w}, \psi, \psi', \lambda_L\}$ and can be expressed like:

$$\delta\ell = \sum_i \frac{\partial\ell}{\partial x_i} \delta x_i. \quad (1.27)$$

We note that ψ is not an independent variable and its variation can be expressed in terms of u and w using Eq. 1.22. Last, before rewriting the Euler-Lagrange equations, we also introduce the work done by non-conservative forces that we can express like:

$$\delta W_{nc} = \int_0^L \left((Q_u - c_u \dot{u}) \delta u + (Q_w - c_w \dot{w}) \delta w \right) ds, \quad (1.28)$$

where Q_u and Q_w are general external forces applied on the beam along the x and z directions, respectively, and c_u and c_w are the corresponding damping coefficients. By substituting Eq.1.27 and 1.28 into Eq.1.1 and integrating by parts we obtain the following equation for the variation of the functional I :

$$\begin{aligned} \delta I = & \int_{t_1}^{t_2} \left\{ \int_0^L \left(-\frac{\partial}{\partial t} \frac{\partial\ell}{\partial\dot{u}} + \frac{\partial}{\partial s} G_u + Q_u - c_u \dot{u} \right) \delta u ds \right. \\ & + \int_0^L \left(-\frac{\partial}{\partial t} \frac{\partial\ell}{\partial\dot{w}} + \frac{\partial}{\partial s} G_w + Q_w - c_w \dot{w} \right) \delta w ds \\ & \left. + \left[-G_u \delta u - G_w \delta w + H_u \delta u' + H_w \delta w' \right]_{s=0}^L \right\} dt = 0, \end{aligned} \quad (1.29)$$

where

$$G_u = \left(\frac{\partial^2\ell}{\partial s \partial \psi'} - \frac{\partial\ell}{\partial\psi} \right) \frac{\partial\psi}{\partial u'} + \lambda_L u', \quad (1.30)$$

$$G_w = \left(\frac{\partial^2\ell}{\partial s \partial \psi'} - \frac{\partial\ell}{\partial\psi} \right) \frac{\partial\psi}{\partial w'} + \lambda_L(1 + w'), \quad (1.31)$$

and

$$H_q = \frac{\partial\ell}{\partial\psi'} \frac{\partial\psi}{\partial q'}, \quad (q = u, w). \quad (1.32)$$

Eq. 1.29 is valid for any arbitrary $\delta u, \delta w$ implying that the individual integrands must be zero. We need now to solve the equations:

$$m\ddot{u} + c_u\dot{u} - Q_u = G'_u, \quad (1.33)$$

$$m\ddot{w} + c_w\dot{w} - Q_w = G'_w, \quad (1.34)$$

and the two point boundary condition equation:

$$\left[-G_u\delta u - G_w\delta w + H_u\delta u' + H_w\delta w' \right]_{s=0}^L = 0. \quad (1.35)$$

As stated before, to solve the equations and obtain the boundary conditions, we need to expand nonlinear terms into polynomials. Remembering that $\tan^{-1} x = x - \frac{1}{3}x^3 + \dots$, we can write:

$$w' = (1 - u'^2)^{1/2} - 1 = -\frac{1}{2}u'^2 + \dots \quad (1.36)$$

$$\psi = \tan^{-1} \frac{u'}{1 + w'} = \tan^{-1} \left[u'(1 - u'^2)^{-1/2} \right] = u' \left(1 + \frac{1}{6}u'^2 \right) + \dots \quad (1.37)$$

Substituting these expressions into Eq. 1.33 and 1.34 and retaining only the terms up to order three, we obtain:

$$m\ddot{u} + c_u\dot{u} - Q_u = \left[-D_\eta \left(u''' + u'u''^2 \right) + \lambda_L u' \right]', \quad (1.38)$$

$$m\ddot{w} + c_w\dot{w} - Q_w = \left[D_\eta (u'''u') + \lambda_L(1 + w') \right]'. \quad (1.39)$$

However, for a weakly damped system like our beam, the damping c_w turns out to be very small and will be thus neglected. By using the relevant conditions at the border $w(0, t)$ and $G_w(L, t) = 0$ (from Eq. 1.35), we obtain, from Eq. 1.36 and 1.39:

$$w = -\frac{1}{2} \int_0^s u'^2 ds, \quad (1.40)$$

$$\lambda_L = -D_\eta u''''u' - \frac{1}{2}m \int_L^s \frac{\partial^2}{\partial t^2} \left(\int_0^s u'^2 ds \right) ds - \int_L^s Q_w ds. \quad (1.41)$$

If we now assume that the acting forces are directed only along x so that $Q_w = 0$ and substitute 1.40 and 1.41 in Eq. 1.38 and keep terms up to the third order we find:

$$\begin{aligned}
& m\ddot{u} + c_u\dot{u} + D_\eta u'''' + D_\eta [u'(u'u'')]'' \\
& + \frac{1}{2}m \left[u' \int_L^s \frac{\partial^2}{\partial t^2} \left(\int_0^s u'^2 ds \right) ds \right]' = Q_u,
\end{aligned} \tag{1.42}$$

where the last two terms on the left side of the equation represent the geometric nonlinearity and the nonlinear inertia, respectively. It is important to note that while both geometric and inertia nonlinearity are considered, their relative contribution changes with the mode number. As a result, the geometric nonlinearity, which is of the hardening type, is dominant for the first flexural mode while the inertia nonlinearity, which is of the softening type, is dominant for the second and higher order flexural modes. In Chapter 2, we focus entirely on the first flexural mode of our resonator and by consequence we will now not consider the nonlinear inertia term.

1.4.3 Frequency response

We now focus on the dependence of the amplitude of oscillation on the frequency of excitation. To do that, we look at the time dependent part of Eq. 1.42 neglecting the nonlinear inertial term. We use the fact that we can write the displacement in the form $u(s, t) = u_n(s)a(t)$ and for a given arclength s we can divide both sides of the equation by $u_n(s)$. In this case we can rewrite equation 1.42 as the so called Duffing equation:

$$\ddot{a} + \gamma\dot{a} + \omega_\xi^2 a + \alpha a^3 = Q_u^*(t), \tag{1.43}$$

where we introduced $\gamma = c_u/m$, α is the nonlinear Duffing coefficient and Q_u^* is the normalized external excitation. By treating the cubic term as a perturbation of a single harmonic oscillator and assuming a general solution in the form of:

$$a(t) = Z \cos(\omega t + \phi_p), \tag{1.44}$$

we can substitute Eq.1.44 into equation 1.43, keeping only terms at frequency ω and squaring both sides of the equation, we can extract the amplitude of oscillation Z as a function of the forcing frequency ω from the implicit equation:

$$Z^2 \left(\omega^2 - \omega_\xi^2 - \frac{3}{4}\alpha Z^2 \right)^2 + (\gamma Z \omega)^2 = Q_u^{*2}. \tag{1.45}$$

The values of Z/Q_u^* as a function of ω/ω_ξ are plotted in Fig.1.5(a) for different values of the cubic coefficient α . Note that for $\alpha = 0$ the equation is equivalent to the one describing a simple harmonic oscillator and the frequency response can be approximated with a lorentzian centered at ω_ξ .

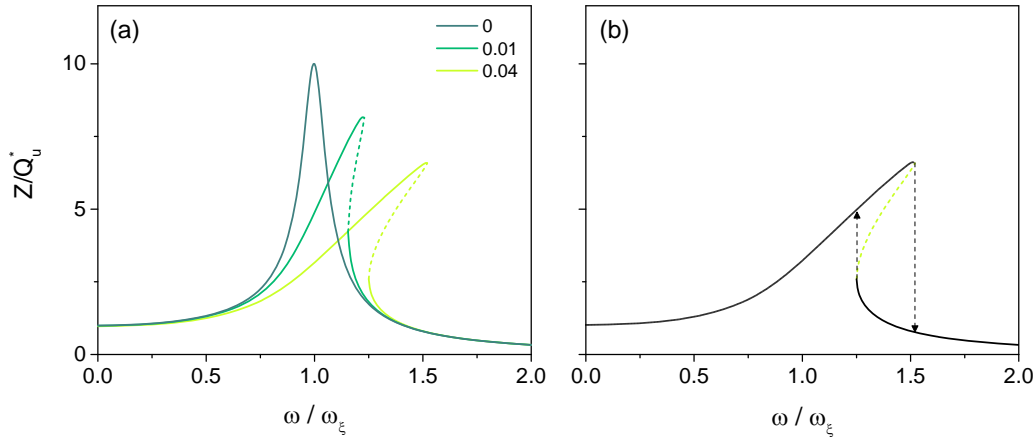


Figure 1.5 | (a) Amplitude of oscillation Z/Q_u^* as a function of normalized frequency ω_ξ/ω plotted for different values of the duffing coefficient α . (b) Frequency hysteresis due to instability of the solution indicated by the dotted line.

When α reaches high values, for some values of ω there are three solutions for the amplitude Z one of which, however, is unstable. The history of the resonator sets what solution is the valid one, resulting in an hysteresis loop when the forcing frequency is swept, as highlighted in Fig. 1.5(b).

1.5 Orthogonal flexural modes

In the last section of this Chapter we consider the more general case where the beam is free to oscillate in any direction. While the the description of the system becomes more complex, the procedure to find the expression for the components of the displacement of interest, namely $u(s, t)$ and $v(s, t)$, remains similar to the one in section 1.4.

1.5.1 System rotation

Since the neutral axis does not bend anymore only by an angle $\psi(s, t)$, the reference system (ξ, η, ζ) with origin in the centroid of the cross-section is now obtained by applying three consequent rotations of counterclockwise angles ψ, θ and ϕ to the inertial system (x, y, z) so that

$$\{\mathbf{e}_\xi, \mathbf{e}_\eta, \mathbf{e}_\zeta\}^T = [T_\phi][T_\theta][T_\psi]\{\mathbf{e}_x, \mathbf{e}_y, \mathbf{e}_z\}^T, \quad (1.46)$$

where:

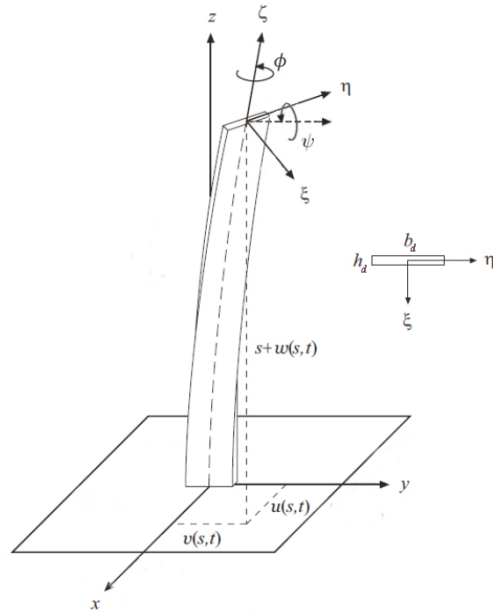


Figure 1.6 | Cantilever beam undergoing flexural-flexural-torsional vibrations

$$[T_\psi] = \begin{bmatrix} \cos \psi & 0 & -\sin \psi \\ 0 & 1 & 0 \\ \sin \psi & 0 & \cos \psi \end{bmatrix}, \quad (1.47)$$

$$[T_\theta] = \begin{bmatrix} 1 & 0 & 0 \\ 0 & \cos \theta & \sin \theta \\ 0 & -\sin \theta & \cos \theta \end{bmatrix}, \quad (1.48)$$

$$[T_\phi] = \begin{bmatrix} \cos \phi & \sin \phi & 0 \\ -\sin \phi & \cos \phi & 0 \\ 0 & 0 & 1 \end{bmatrix}. \quad (1.49)$$

By consequence, the curvature of the beam can be written as:

$$\boldsymbol{\kappa}(s, t) = \kappa_\xi \mathbf{e}_\xi + \kappa_\eta \mathbf{e}_\eta + \kappa_\zeta \mathbf{e}_\zeta, \quad (1.50)$$

where each component is now given by:

$$\kappa_\xi \equiv \frac{\partial \mathbf{e}_\zeta}{\partial s} \cdot \mathbf{e}_\eta = \psi' \cos \theta \sin \phi + \theta' \cos \phi, \quad (1.51)$$

$$\kappa_\eta \equiv \frac{\partial \mathbf{e}_\zeta}{\partial s} \cdot \mathbf{e}_\xi = \psi' \cos \theta \cos \phi - \theta' \sin \phi, \quad (1.52)$$

$$\kappa_\zeta \equiv \frac{\partial \mathbf{e}_\xi}{\partial s} \cdot \mathbf{e}_\eta = \phi' - \psi' \sin \theta. \quad (1.53)$$

Note that in the simple case that $\theta = \phi = 0$, we find back the simple case of the planar motion along x and $\kappa_\eta = \psi'$. In the same way, if $\psi = \phi = 0$ then the only non zero component is $\kappa_\xi = \theta'$ and the beam bends only along the y axis.

1.5.2 Lagrangian of motion

Also in this case we aim to find the full expression of the specific Lagrangian before finding the stationary point of the functional I . The kinetic energy of the system is simply given by:

$$T_k = \frac{1}{2} m \int_0^L (\dot{u}^2 + \dot{v}^2 + \dot{w}^2) ds. \quad (1.54)$$

The bending in x and y still produces uniaxial strain along z :

$$\epsilon_{33} = \eta \kappa_\xi - \xi \kappa_\eta, \quad (1.55)$$

where the opposite sign is due to the fact that positive values of θ produce negative displacement v that results in tensile strain. The torsion of the beam instead produces shear strain γ_{ij} that now we need to consider and is given by:

$$\epsilon_{13} = \frac{1}{2} \gamma_{13} = \xi \kappa_\zeta \quad (1.56)$$

$$\epsilon_{23} = \frac{1}{2} \gamma_{23} = -\eta \kappa_\zeta \quad (1.57)$$

while the other components of the strain tensor remain zero or negligible. The strain energy is now given by:

$$U = \frac{1}{2} \int_0^L \left\{ \iint_A (\sigma_{33} \epsilon_{33} + \sigma_{23} \gamma_{23} + \sigma_{13} \gamma_{13}) d\xi d\eta \right\} ds. \quad (1.58)$$

By assuming $\sigma_{13} \approx G \gamma_{13}$ and $\sigma_{23} \approx G \gamma_{23}$ where G is the shear modulus, and using again the fact that $\sigma_{33} \approx E_Y \epsilon_{33}$, we can rewrite the potential energy of our beam as:

$$U = \frac{1}{2} \int_0^L (D_\xi \kappa_\xi^2 + D_\eta \kappa_\eta^2 + D_\zeta \kappa_\zeta^2) ds, \quad (1.59)$$

where:

$$\begin{aligned} D_\xi &= E_Y \iint_A \eta^2 d\xi d\eta, \\ D_\eta &= E_Y \iint_A \xi^2 d\xi d\eta, \\ D_\zeta &= G \iint_A (\xi^2 + \eta^2) d\xi d\eta. \end{aligned} \quad (1.60)$$

Here, the first two terms are representing the bending stiffness, and the third one the torsional one. The last term we need to include in the Lagrangian is the the inextensionality constraint that can be extracted from Eq. 1.23 and becomes:

$$(1 + w')^2 + v'^2 + u'^2 = 1. \quad (1.61)$$

Finally, we can write the overall specific lagrangian as:

$$\begin{aligned} \ell &= \frac{1}{2} m (\dot{u}^2 + \dot{v}^2 + \dot{w}^2) - \frac{1}{2} (D_\xi \kappa_\xi^2 + D_\eta \kappa_\eta^2 + D_\zeta \kappa_\zeta^2) \\ &+ \frac{1}{2} \lambda_L [1 - u'^2 - v'^2 - (1 + w')^2]. \end{aligned} \quad (1.62)$$

1.5.3 Nonlinear equations of motion

The only independent vairables in this case are u , v , w , and ϕ while all the variation of other variables can be expressed as a function of those. From Fig.1.4 we can extract an explicit expression for the angle θ :

$$\tan \theta = -\frac{v'}{\sqrt{u'^2 + (1 + w')^2}}. \quad (1.63)$$

By introducing the last non-conservative forces $Q_v - c_v \dot{v}$ and $Q_\phi - c_\phi \dot{\phi}$, and following the same procedure as explained in section 1.4.2, we can write the expression for the variation of the functional I , integrate by parts and set to zero the individual integrands, obtaining the following equations:

$$m\ddot{u} + c_u \dot{u} - Q_u = G'_u, \quad (1.64)$$

$$m\ddot{v} + c_v \dot{v} - Q_v = G'_v, \quad (1.65)$$

$$m\ddot{w} + c_w \dot{w} - Q_w = G'_w, \quad (1.66)$$

$$Q_\phi - c_\phi \dot{\phi} = J'_\phi, \quad (1.67)$$

$$\left[-G_u \delta u - G_u \delta u - G_u \delta u + H_u \delta u' + H_v \delta v' + H_w \delta w' + \frac{\partial \ell}{\partial \phi'} \delta \phi \right]_{s=0}^L = 0, \quad (1.68)$$

where we used the compact form:

$$\begin{aligned} G_u &= J_\psi \frac{\partial \psi}{\partial u'} + J_\theta \frac{\partial \theta}{\partial u'} + \lambda_L u', \\ G_v &= J_\theta \frac{\partial \theta}{\partial v'} + \lambda_L v', \\ G_w &= J_\psi \frac{\partial \psi}{\partial w'} + J_\theta \frac{\partial \theta}{\partial w'} + \lambda_L (1 + w'), \end{aligned} \quad (1.69)$$

and

$$\begin{aligned} J_k &= \frac{\partial^2 \ell}{\partial t \partial k} + \frac{\partial^2 \ell}{\partial s \partial k'} - \frac{\partial \ell}{\partial k} \quad (k = \psi, \theta, \phi), \\ H_q &= \frac{\partial \ell}{\partial \psi'} \frac{\partial \psi}{\partial q'} + \frac{\partial \ell}{\partial \theta'} \frac{\partial \theta}{\partial q'} \quad (q = u, v, w). \end{aligned} \quad (1.70)$$

Now we can again expand the expressions of the displacement w and of the angles ψ and θ into polynomials up to order three:

$$w' = (1 - u'^2 - v'^2)^{1/2} - 1 = -\frac{1}{2}(u'^2 + v'^2) + \dots \quad (1.71)$$

$$\begin{aligned} \psi &= \tan^{-1} \frac{u'}{1 + w'} = \tan^{-1} \left[u'(1 - u'^2 - v'^2)^{-1/2} \right] \\ &= u' \left(1 + \frac{1}{6}u'^2 + \frac{1}{2}v'^2 \right) + \dots \end{aligned} \quad (1.72)$$

$$\begin{aligned} \theta &= \tan^{-1} \frac{-v'}{[(1 + w')^2 + u'^2]} = \tan^{-1} \left[-v'(1 - v'^2)^{-1/2} \right] \\ &= v' \left(1 + \frac{1}{6}v'^2 \right) + \dots \end{aligned} \quad (1.73)$$

By substituting eq.1.72 and 1.73 into 1.53 we find $\kappa_\zeta = \phi' + u''v'$. We note that in our case ϕ does not represent the twist angle of the beam with respect to the neutral axis, also indicating that a non-zero angle ϕ does not guarantee the presence of torsion along the beam [52]. We can define the twist angle γ_t as:

$$\gamma_t \equiv \phi + \int_0^s u''v' ds, \quad (1.74)$$

so that $\kappa_\zeta = \gamma_t'$. By substituting Eq. 1.71 - 1.74 into Eq. 1.66 - 1.35 with the relevant boundary conditions $w(0, t) = 0$, $G_w(L, t) = 0$, $\gamma_t(0, t) = 0$, and $\gamma_t'(L, t) = 0$ we can write:

$$w = -\frac{1}{2} \int_0^s (u'^2 + v'^2) ds, \quad (1.75)$$

$$\begin{aligned} \lambda_L &= -D_\eta u'''' u' - D_\xi v'''' v' \\ &\quad - \frac{1}{2} m \int_L^s \left[\int_0^s \frac{\partial^2}{\partial t^2} (u'^2 + v'^2) ds \right] ds - \int_L^s Q_w ds, \end{aligned} \quad (1.76)$$

$$\gamma_t = -\frac{D_\xi - D_\eta}{D_\zeta} \int_0^s \int_L^s u'' v'' ds ds. \quad (1.77)$$

We can now use Eq. 1.75 - 1.77, Eq.1.64 and 1.65 and the boundary condition equations, keeping terms up to the third order and obtain:

$$\begin{aligned} m\ddot{u} + c_u \dot{u} + D_\eta u'''' &= Q_u + \left\{ (D_\xi - D_\eta) \left[v'' \int_L^s u'' v'' ds - v'''' \int_0^s u'' v' ds \right] \right. \\ &\quad \left. - \frac{(D_\xi - D_\eta)^2}{D_\zeta} \left(v'' \int_0^s \int_L^s u'' v'' ds ds \right)' \right\}' - D_\eta \left\{ u'(u' u'' + v' v'')' \right\}' \\ &\quad - \frac{1}{2} m \left\{ u' \int_L^s \frac{\partial^2}{\partial t^2} \left[\int_0^s (u'^2 + v'^2) ds \right] ds \right\}' - \left(u' \int_L^s Q_w ds \right)', \end{aligned} \quad (1.78)$$

$$\begin{aligned} m\ddot{v} + c_v \dot{v} + D_\xi v'''' &= Q_v - \left\{ (D_\xi - D_\eta) \left[u'' \int_L^s u'' v'' ds - u'''' \int_0^s v'' u' ds \right] \right. \\ &\quad \left. + \frac{(D_\xi - D_\eta)^2}{D_\zeta} \left(u'' \int_0^s \int_L^s u'' v'' ds ds \right)' \right\}' - D_\eta \left\{ v'(u' u'' + v' v'')' \right\}' \\ &\quad - \frac{1}{2} m \left\{ v' \int_L^s \frac{\partial^2}{\partial t^2} \left[\int_0^s (u'^2 + v'^2) ds \right] ds \right\}' - \left(v' \int_L^s Q_w ds \right)', \end{aligned} \quad (1.79)$$

with the following boundary conditions:

$$u(0, t) = 0, \quad v(0, t) = 0, \quad u'(0, t) = 0, \quad v'(0, t) = 0, \quad (1.80)$$

$$u''(L, t) = 0, \quad v''(L, t) = 0, \quad u'''(L, t) = 0, \quad v'''(L, t) = 0. \quad (1.81)$$

While only cubic nonlinear terms are considered, we can distinguish the terms with the second time derivatives in Eq. 1.78 and 1.79 that represent nonlinear inertia. All the other nonlinear terms are of the geometric nonlinearity type and originate from the potential energy stored in bending. There is one last remark that we can make from this equation of motion: if $D_\xi = D_\eta$ then there's no coupling between the flexural and torsional modes in the beam.

1.5.4 Adimensional equations

It is possible to rewrite the equations 1.78 and 1.79 in a dimensionless form by substituting $\tilde{s} = s/L$, $\tilde{u}_n = u_n/h_d$, $\tilde{v}_n = v_n/h_d$, $\tilde{c}_u = c_u L^4/(D_\eta \tau_s)$ and scaling time with $\tau_s = L^2 \sqrt{m/D_\eta}$. By using the fact that $u_n(s) = v_m(s)$ when $n = m$ we can apply the Galerking procedure for the first flexural mode in both directions $\tilde{u}(\tilde{s}, \tilde{t}) = \tilde{u}_1(\tilde{s})a(\tilde{t})$, $\tilde{v}(\tilde{s}, \tilde{t}) = \tilde{v}_1(\tilde{s})b(\tilde{t})$ giving us the simplified form:

$$\begin{aligned} & \ddot{a} + \tilde{c}_u \dot{a} + \omega_\xi^2 a + C_1 \left(\frac{h_d}{L}\right)^2 a^3 \\ & + \left(C_1 + \left(1 - \frac{D_\eta}{D_\xi}\right) C_2 - \frac{D_\xi}{D_\zeta} \left(1 - \frac{D_\eta}{D_\xi}\right)^2 C_3 \right) \left(\frac{h_d}{L}\right)^2 ab^2 \\ & + C_4 \left(\frac{h_d}{L}\right)^2 a(\dot{a}^2 + a\ddot{a} + \dot{b}^2 + b\ddot{b}) = C_5 Q_u, \end{aligned} \quad (1.82)$$

$$\begin{aligned} & \ddot{b} + \tilde{c}_v \dot{b} + \omega_\eta^2 b + C_1 \left(\frac{h_d}{L}\right)^2 b^3 \\ & - \left(C_1 + \left(1 - \frac{D_\eta}{D_\xi}\right) C_2 - \frac{D_\xi}{D_\zeta} \left(1 - \frac{D_\eta}{D_\xi}\right)^2 C_3 \right) \left(\frac{h_d}{L}\right)^2 a^2 b \\ & + C_4 \left(\frac{h_d}{L}\right)^2 b(\dot{a}^2 + a\ddot{a} + \dot{b}^2 + b\ddot{b}) = C_5 Q_v, \end{aligned} \quad (1.83)$$

where we defined the coefficients (remembering that $\tilde{u}_1 = \tilde{v}_1$):

$$C_1 = \int_0^1 \tilde{u}_1 \left(\tilde{u}_1' (\tilde{u}_1 \tilde{u}_1'') \right)' d\tilde{s} = 40.41, \quad (1.84)$$

$$C_2 = \int_0^1 \tilde{u}_1 \left(\tilde{u}_1' \int_0^{\tilde{s}} \int_1^{\tilde{s}_1} (\tilde{u}_1')^2 d\tilde{s}_2 d\tilde{s}_1 \right)' d\tilde{s} = 4.60, \quad (1.85)$$

$$\begin{aligned} C_3 = & \left[\int_0^1 \tilde{u}_1 \left(\tilde{u}_1'' \int_1^{\tilde{s}_1} \tilde{u}_1'' \tilde{u}_1'' ds_1 \right)' ds \right] \\ & - \left[\int_0^1 \tilde{u}_1 \left(\tilde{u}_1''' \int_0^{\tilde{s}_1} \tilde{u}_1'' \tilde{u}_1' ds_1 \right)' ds \right] = -20.11, \end{aligned} \quad (1.86)$$

$$C_4 = \int_0^1 \tilde{u}_1 \left(\left(\tilde{u}_1'' \int_0^{\tilde{s}} \int_1^{\tilde{s}_1} \tilde{u}_1'' \tilde{u}_1'' ds_2 ds_1 \right)' \right)' ds = 16.60, \quad (1.87)$$

$$C_5 = \int_0^1 \tilde{u}_1 d\tilde{s} = 0.78. \quad (1.88)$$

A few interesting notes can be made on this pair of equations. The geometrical coupling between the two modes arises from the terms in ab^2 and a^2b for the first and second equation, respectively. This produces a shift of the resonance of one mode proportional to the square of the amplitude of the other mode. In the limiting case when the two modes are degenerate (i.e. $D_\xi = D_\eta$) the coupling is set only by the positive coefficient C_1 . However, the ratio D_η/D_ξ can be adjusted by changing the cross section of the beam. By doing this it is possible to change the sign of the nonlinear coupling coefficient.

2 | Nanowires Nanomechanics

2.1 Introduction

In this chapter we present the results of the study of the motion of several as-grown GaAs nanowires still attached to their GaAs growth substrate. We observe that, upon driving the periodic bending motion of a nanowire with sufficiently large amplitudes, it can no longer be described by a linear equation of motion. Instead, the nanowire follows the, qualitatively different, nonlinear dynamics of a Duffing oscillator [53] as described in the previous chapter. A Duffing nonlinearity can give rise to complex motion of an oscillator, such as hysteresis, cascades of period-doubling, and chaotic motion [54]. In the quantum regime, Duffing nonlinearities have recently been studied in the context of mechanical squeezing [55]. Furthermore, we find that when applying two driving frequencies, the nanowire motion in the nonlinear regime contains components at frequencies other than the two driving frequencies, as a result of mechanical mixing.

Furthermore, a small asymmetry in the cross-section of a nanowire leads to the formation of two non-degenerate orthogonal modes. By driving one mode in its nonlinear regime of motion, the other mode is observed to shift in frequency. We then proceed to investigate nonlinear coupling of orthogonal flexural modes of these GaAs nanowires. In a ringdown-type experiment, this leads to a distinct beating pattern in the time domain, where the beating period decreases with time. We will proceed to show that the mode coupling and nonlinearity can be exploited for the implementation of frequency modulation, amplitude to frequency conversion and logical operations.

2.2 GaAs Nanowires

The nanowires under investigation here were grown perpendicularly to their GaAs growth substrate and are still attached to this substrate (see Fig. 2.1). Using the nanowires as they are grown minimizes the introduction of defects and maintains good clamping of the nanowires to the substrate. Both factors should decrease damping of the mechanical resonance of the nanowires.

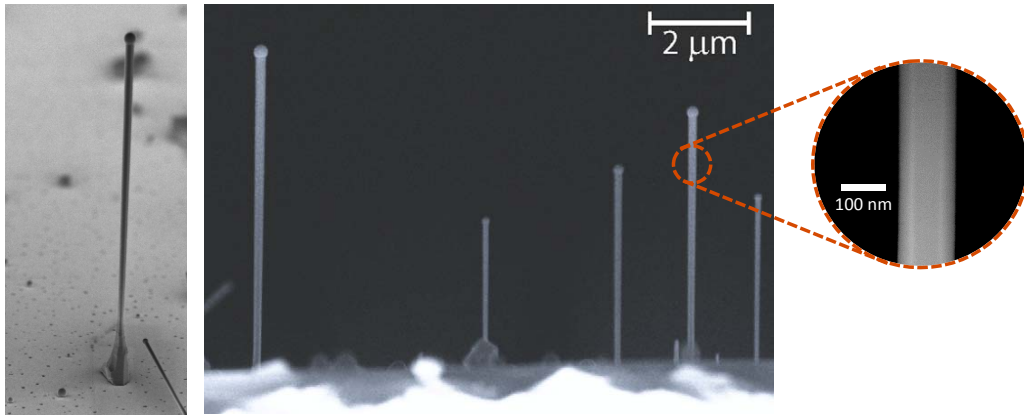


Figure 2.1 | Scanning electron micrographs (SEM) of a substrate containing multiple GaAs nanowires, taken at a different section of the same wafer that was used in the experiments. Inset: close-up of a single nanowire, showing a faceted structure due to its hexagonal cross-section.

The nanowires were grown on a 4 nm SiO_x coated (111)B GaAs substrate by the catalyst-free Gallium-assisted method [56] in a DCA P600 solid source molecular beam epitaxy system. Growth has been done under a rotation of 7 rpm, with a growth rate of 0.5 \AA/s and a substrate temperature of 630°C . The nanowires mostly exhibit zinc-blende crystal structure, and therefore have hexagonal cross-sections, with typical diameters of 100 nm and lengths up to $25 \mu\text{m}$. The diameter of individual nanowires is constant, except for the tip where a Gallium droplet is formed during growth and the base, where small anomalous structures can be present. Keeping the nanowires pristine is important, as further processing can significantly degrade their structural and mechanical properties. Avoiding post-processing of the nanowires minimizes the introduction of surface defects and ensures the rigid clamping of the nanowires to their substrate. Indeed, mechanical dissipation rates in grown nanowires have been reported to be much lower than for similar cantilevers produced in a top-down manner [1]. These GaAs nanowires are of particular interest, since the same structures are straightforwardly coated by subsequent growth steps with a AlGaAs/GaAs shell hosting self-assembled optical quantum dots [57].

2.3 Displacement detection

2.3.1 Introduction

To detect the motion of nanoresonators various techniques with different advantages are available. The displacement of a mechanical element can be

detected by the means of an optical lever, where the light is deflected by an angle proportional to the angular displacement of the resonator. It is also possible to detect (and drive) the displacement electrostatically by using the mechanical element as one plate of a capacitor. In optical interferometry, instead, the mechanical element is used as one end of a Fabry-Perot interferometer and this technique is sensitive primarily to the translation of the element [58]. The latter is our choice, as this technique has been proven to reach high sensitivity and its compactness makes the implementation possible in systems operating in extreme conditions such as UHV and low temperatures.

2.3.2 Optical fiber interferometer

In our setup, the light emitted by a fiber coupled laser diode is directed into an arm of an asymmetrical 95–5 2x2 fiber coupler where the light is split and 95% of it is diverted on one of the two outputs of the coupler and is collected by a photodetector that we use as a power monitor. The remaining 5% goes into the sensing fiber that is terminated with a perpendicular cleave. Part of the light is then reflected at the vacuum-fiber interface while the rest of the light is then focused on a single nanowire by the means of an aspherical lens. The nanowire reflects part of the incident light which is then refocused into the fiber creating interference (see Fig.2.2). This light is guided back to the coupler and 95% of it is collected by another photodetector that produces a voltage proportional to the signal power. The displacement of the nanowire modulates the interference and can be obtained from the collected signal.

If we assume that the light gets reflected only once inside the cavity formed between the fiber and the nanowire (assumption that is valid considering that the beam spot is larger than the diameter of the nanowire), then we can express the intensity of the light coming back in the fiber as:

$$I(x) = I_0 + I_1 \cos(4\pi x/\lambda), \quad (2.1)$$

where x is the position of the cantilever with respect to the optical fiber, λ is the wavelength of the incident light, and I_0 is a constant arising from the fact that more light is returned from the fiber glass/air interface than from the resonator. I_1 is the amplitude of the modulation of the oscillation fringes. The oscillation of the cantilever can be described as:

$$x(t) = x_0 + x_1 \sin(\omega t), \quad (2.2)$$

where x_0 is the equilibrium distance of the resonator from the end of the fiber, x_1 is the amplitude of the oscillations, and $\omega/2\pi = \nu$ is the frequency

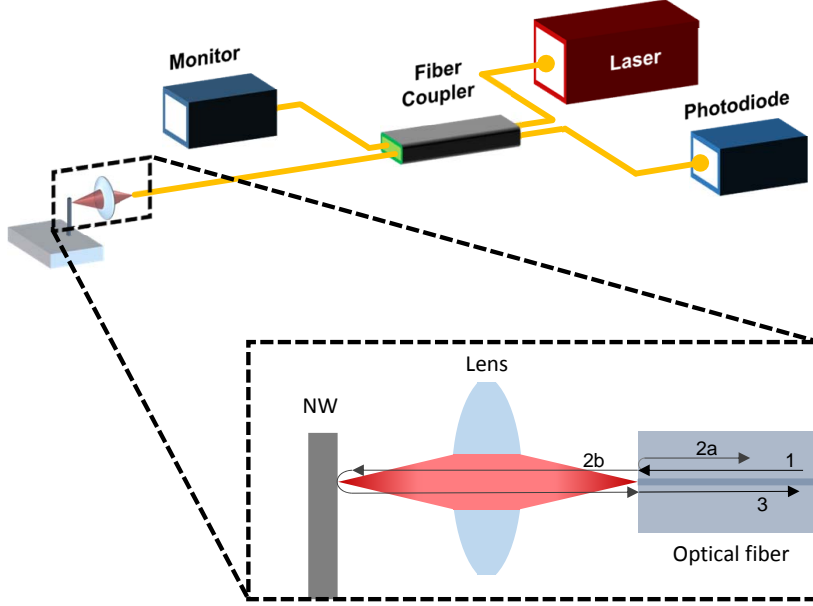


Figure 2.2 | Scheme of the interferometer setup. In the inset the reflections leading to the interference are highlighted.

of oscillation of the cantilever motion. By substituting Eq. 2.2 into Eq. 2.1 we obtain:

$$I(t) = I_0 + I_1 \cos(4\pi(x_0 + x_1 \sin(\omega t))/\lambda). \quad (2.3)$$

Eq.2.3 can be Fourier expanded in:

$$I(t) = I_0 \sum_{n=odd} \cos\left(\frac{4\pi x_0}{\lambda}\right) J_n\left(\frac{4\pi x_1}{\lambda}\right) \cos(n\omega t) - I_0 \sum_{n=even} \sin\left(\frac{4\pi x_0}{\lambda}\right) J_n\left(\frac{4\pi x_1}{\lambda}\right) \sin(n\omega t), \quad (2.4)$$

where $J_n(z)$ is the n^{th} regular Bessel function of z . An oscillation at frequency ν produces a modulation at all harmonics of ν with the amplitude of the n^{th} harmonic proportional to the n^{th} Bessel function of the amplitude of the motion of the resonator. The odd harmonics are stronger when the lever is near to an odd multiple of $\lambda/4$, and the even harmonics are stronger when it is near to an even multiple of $\lambda/4$. One consequence of this nonlinear behaviour of the interferometer is that the signal cannot be increased arbitrarily by just increasing the amplitude of oscillation of the resonator. In fact, the maximum signal that can be reached is $0.5819I_1$, which occurs when $x_1 = 1.842\lambda/4\pi$ (when the first Bessel function J_1 is at its maximum). On the positive side we

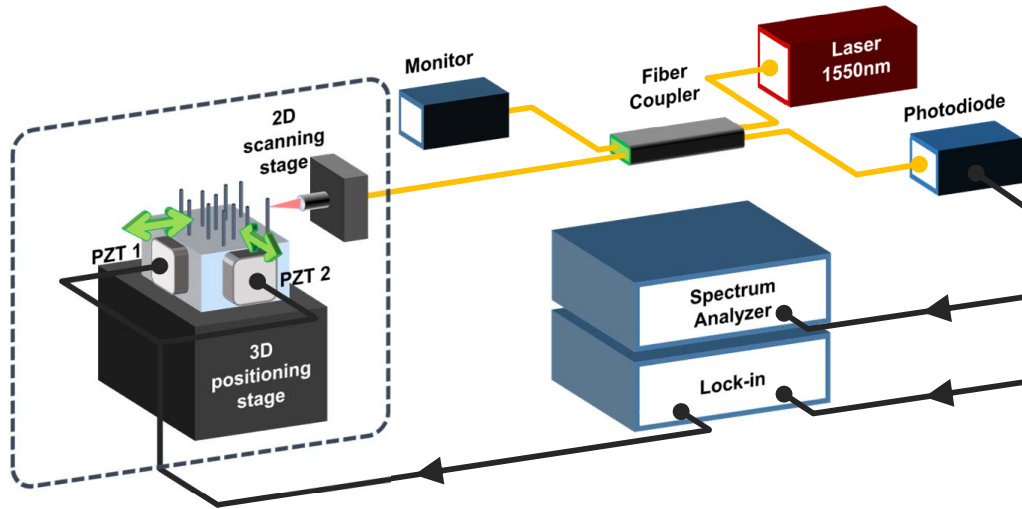


Figure 2.3 | Schematic diagram of the measurement setup.

find that by looking at the peak of the Bessel function is possible to calibrate the amplitude of the oscillation of the resonator.

2.4 Experimental results

2.4.1 Setup

Fig. 2.3 shows a scheme of the setup used to study the motion of the nanowires. A cleaved portion of a wafer with NWs described in Section 2.2 is mounted on a stack of positioning stages for three-axis translation control, allowing a single nanowire of choice to be positioned in the focal plane of an objective placed in front of the single-mode fiber. A voltage-controlled piezoelectric transducer (PZT) attached to the sample holder is used to drive oscillatory bending motion of the nanowires along the optical axis of the interferometer. A fiber coupler is used to inject light from a laser with a wavelength of 1550 nm into the interferometer. This wavelength is chosen in order to avoid spurious heating of the GaAs nanowires through absorption. The coupler diverts 5% of the laser power towards the nanowire, resulting in a maximum power incident on the nanowire of $\sim 5\mu\text{W}$. Varying the laser power slightly did not qualitatively change the measurements, ensuring that no significant heating of the nanowire is taking place. The light reflected by the interferometer is collected by a photodiode with a dynamic range of 5 MHz. The oscillator of a lock-in amplifier actuates the PZT and the same lock-in amplifier demodulates the response of the photodiode. Sample and microscope are placed inside a vacuum can, which in turn is mounted inside a liquid helium

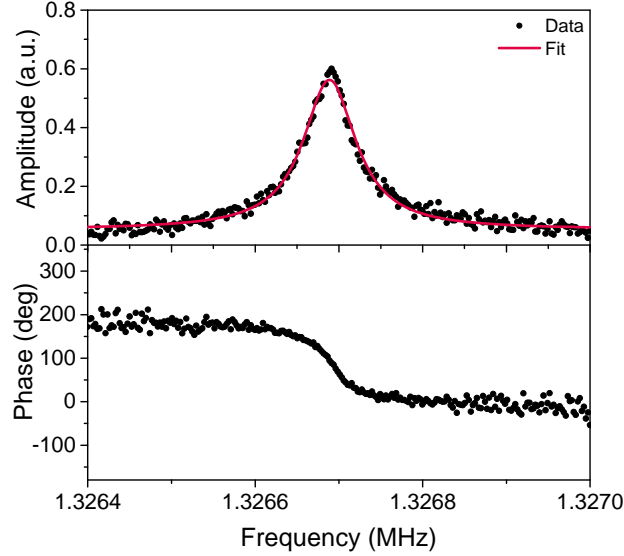


Figure 2.4 | Amplitude (top) and phase (bottom) of a driven nanowire in the linear regime. Black dots represent experimental data while the red solid line is a Lorentzian fit.

bath cryostat.

2.4.2 Linear and nonlinear response

The nanowires investigated here have their fundamental mechanical resonances at frequencies of $f_0 = 1.2 - 1.35$ MHz (some nanowires show two closely spaced resonances, which we attribute to two transverse flexural modes that are non-degenerate due to a slight asymmetry of the nanowire cross-section). Numerical calculations following the same method as used in Ref. [8] confirm that these resonances indeed correspond to the fundamental flexural modes of the singly-clamped nanowires.

Furthermore, these resonances exhibit quality factors of up to 37,000 (at a temperature of 4.2 K and pressure below 10^{-6} mbar), as determined from the width of the resonance as well as from ringdown measurements. Many factors contribute to limiting the quality factor of nanomechanical resonators, including lattice defects, which would at this scale likely be dominated by surface defects, surface oxides, clamping losses, and coupling to other mechanical modes [59, 60]. The quality factors observed for the as-grown nanowires studied here are up to an order of magnitude larger than for similar GaAs-based nanowires [9], which is a possible indication of the degrading effect of post-processing on the mechanical quality factor. Figure 2.4 shows the measured displacement and relative phase of a nanowire for a small driving amplitude. The relative small driving amplitude assures that the nanowire is maintained in its linear regime as the amplitude in the

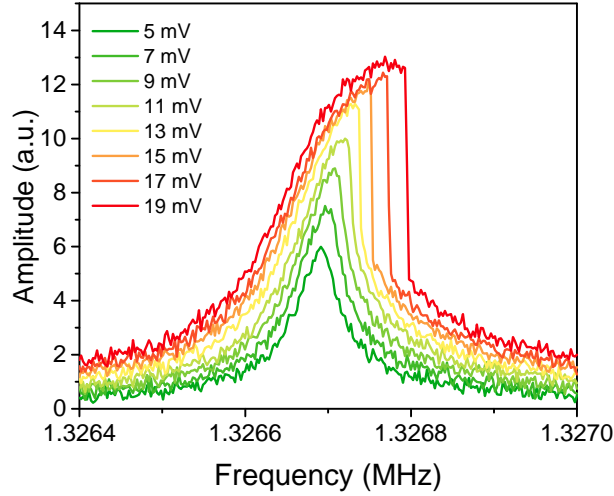


Figure 2.5 | Response amplitude as a function of driving frequency, for various driving amplitudes. Note that the slight depression around the maximum response for the highest driving amplitude is caused by the limited linear range of the interferometer.

frequency domain can be fitted with a lorentzian curve.

As the driving amplitude is increased, the resonance becomes broader assumes a characteristic shark-fin shape when entering the nonlinear regime as shown in Fig. 2.5, where the frequency associated with maximum displacement increases and moves away from the resonator eigenfrequency $\omega_0 = 2\pi f_0$. Such behavior is typical for a Duffing oscillator and can be described by the Duffing equation of motion as described in Section 1.4.3 (including nonlinear damping):

$$\ddot{a}(t) + \gamma\dot{a}(t) + \omega_0^2 a(t) + \alpha a^3(t) + \gamma_N a(t) (\dot{a}^2(t) + a(t)\ddot{a}(t)) = Q(t). \quad (2.5)$$

Here a is the displacement, γ and γ_N the linear and nonlinear damping constants, and $Q(t)$ the time-dependent driving force, here taken to be sinusoidal. The coefficient α parametrizes the strength of the cubic Duffing nonlinearity. When α is positive, as it is in our case, the Duffing nonlinearity increases the effective spring constant with increasing driving amplitude, thus stiffening the motion. The observed lineshape at higher driving amplitudes is a consequence of Eq. 2.5 having two stable solutions within a certain frequency range. This bistability leads to the switching phenomena seen at the right flank of the response peak (Fig. 2.5). Which of the two solutions is realized, is determined by the initial conditions, and mechanical hysteresis can be observed when adiabatically sweeping the driving frequency or driving amplitude up and down (Figures 2.6(a) and (b)). The strength of the nonlinearity α can be estimated from the shift of the frequency f_{max} at which the maximum response amplitude occurs, using the relation [53]:

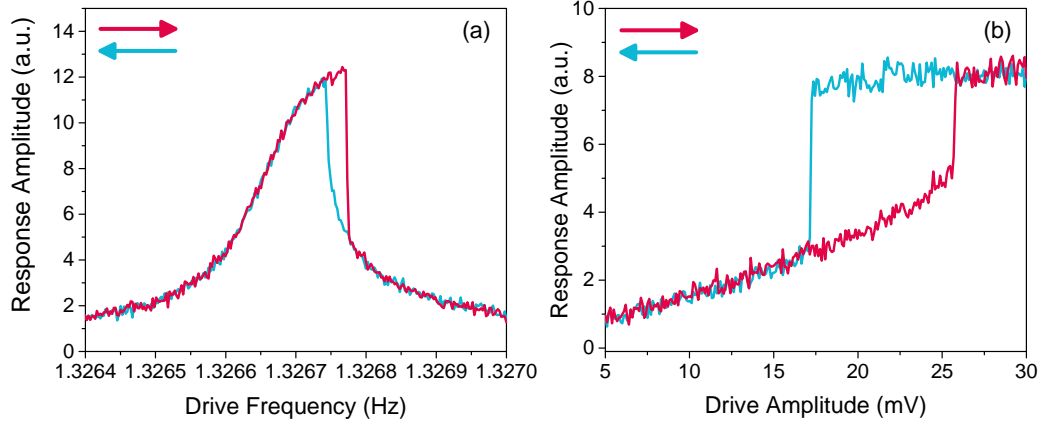


Figure 2.6 | (a) Response amplitude as a function of driving frequency (at a driving amplitude of 17 mV), for two sweep directions (as indicated by arrows). (b) Response amplitude as a function of driving amplitude (at a driving frequency of 1326770 Hz), for two sweep directions.

$\alpha = \frac{32}{3}\pi^2 f_0(f_{max} - f_0)/a^2$. Our interferometer becomes nonlinear for larger driving amplitudes (see Fig. 2.5), since then the displacement becomes comparable to the width of the interferometer fringes. We use this to infer [61] a value for the displacement a of ~ 250 nm, for a driving amplitude of 19 mV (Fig. 2.5). We can then estimate α to be of order $10^{23} \text{ m}^{-2}\text{s}^{-2}$ for this nanowire. Nonlinear damping could arise in the presence of a Duffing nonlinearity and linear damping [19]. We briefly discuss this and show that in our case nonlinear damping does not play a significant role. The nonlinear damping term has the effect of decreasing the shift of the frequency of maximum response amplitude due to the Duffing nonlinearity, as well as decreasing the size of the hysteresis loop. The coefficient for nonlinear damping γ_N can be estimated from the critical frequency, which is the frequency at which the system, with sufficient driving strength, turns from being monostable to being bistable. This critical frequency has a minimum when nonlinear damping is absent, which corresponds to $\sqrt{3}f_0/2Q$ [24]. This yields ~ 52 Hz in our case, agreeing very well to the value of 49 Hz determined from the measurements, indicating that here γ_N is negligible.

2.4.3 Mechanical Mixing

Next, we show that the nonlinearity can be used to turn a nanowire into a mechanical mixer [26, 27]. Upon excitation with two driving frequencies, $Q(t) = Q_1 \cos(2\pi f_1 t + \phi_1) + Q_2 \cos(2\pi f_2 t + \phi_2)$, the response shows sidebands additional to the motion at the driving frequencies, as shown in Figure 2.7(a). We observe up to twelve such sidebands, spaced around the driving frequencies with splittings equal to the detuning between the two driving frequencies,

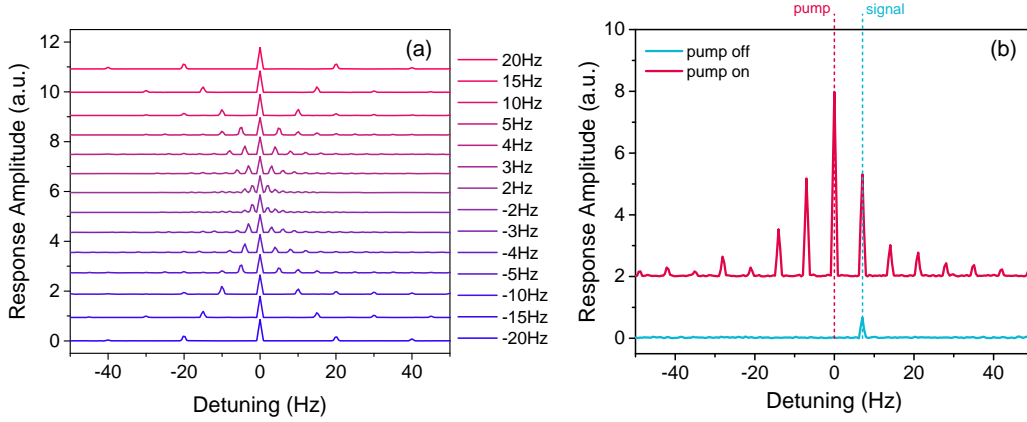


Figure 2.7 | (a) Spectral response amplitudes of the nanowire motion upon application of two driving frequencies, for various values of the detuning of the signal frequency from the pump frequency. The curves have been offset for clarity. The spectral response is given as a function of the detuning from the pump frequency, which is 1287890 Hz. The pump and signal amplitudes are 250 mV and 50 mV, respectively. The first mechanical mode of this nanowire has a resonant frequency of 1287780 Hz. (b) Spectral response with pump excitation (1287913 Hz, 250 mV) off (lower curve) and on (upper curve) for a signal detuned from the pump frequency by 7 Hz and with amplitude 35 mV. The curves have been offset for clarity.

$\Delta f = f_2 - f_1$. Note that the results shown in Fig. 2.7 were obtained by measuring on a second nanowire. Measurements on both nanowires were very similar, but the signal to noise ratio varied.

This response can be understood from Eq. 2.5 by taking the cubic term to be a perturbation to the driving force and solving the equation iteratively [53, 62]. One then obtains new terms in the response at the intermodulation frequencies $f_1 - n\Delta f$ and $f_2 + n\Delta f$ (where n is an integer) for each iteration. The amplitudes of these new intermodulation terms have coefficients proportional to $\sum_n (f_0^2 - f_1^2)^{-k} (f_0^2 - f_2^2)^{-l}$, with k and l positive integers and $k + l = n$. Hence, intermodulation terms are smaller for driving frequencies that are more detuned from resonance. Since the mixing occurs due to the cubic term in Eq. 2.5, for the intermodulation terms to be present, at least one of the driving amplitudes needs to be large enough to have an appreciable nonlinear response.

It is evident from Fig. 2.7 that the energy that is injected into the nanowire oscillator by the driving is distributed among the various intermodulation terms. This redistribution also occurs when one drive (signal) is much smaller than the other (pump), in which case amplification of the signal can take place [24]. The signal here is formed by a driving voltage supplied to the PZT, but it could be any force driving the nanowire with a frequency close to the resonance. Fig. 2.7(b) shows the spectral response of the nanowire motion with the signal drive always on, but with the pump excitation off in

one case and on in the other. It is clear that amplification of the signal takes place when the pump excitation is switched on in the form of an increase in amplitude of the response at the signal frequency. Additionally, the appearance of the intermodulation terms, which is conditional on the presence of a signal, provides extra amplification. The total gain can be defined to be the ratio between the summed response amplitudes of all peaks present with pump drive, excluding the peak at the pump frequency itself, and the response amplitude with no pump drive. We observe a maximum gain of 26 dB. Although higher gain might be expected [24] in the limit of vanishing detuning between pump and signal frequencies, detection of the signal then becomes impractical. The observation of mechanical frequency mixing is furthermore limited by the onset of nonlinearity of the detection interferometer for high displacement amplitudes. If the interferometer response becomes significantly nonlinear, multiple frequencies in the mechanical response can also lead to new frequency components in the detected signal. However, we already observe intermodulation frequency components for small excitation amplitudes, large enough to reach the mechanical nonlinear regime, but small enough to generate mechanical displacements of up to only 10 nm. For these displacements, the second- and third-order terms in the optical response are smaller than 2 % and 0.02 % of the first-order term, respectively. The amplitude of any optically generated sidebands is therefore very small, indicating the mechanical origin of the observed sidebands.

2.4.4 Mode Coupling

As hinted in Section 1.3.2, a small asymmetry can be present in the cross-section of a grown nanowire, as shown also schematically in Figure 2.8(a). Such an asymmetry leads to the formation of two non-degenerate flexural modes along the indicated directions (purple and orange arrows). As shown in Figure 2.8(b), the two modes of a third nanowire have resonant frequencies at $f_1 = \omega_1/2\pi = 1.194$ MHz and $f_2 = \omega_2/2\pi = 1.200$ MHz, which are reproduced numerically for a wire with a similar geometry, requiring an asymmetry in the cross-section of only 0.5%. From ringdown measurements, as discussed later, we determine quality factors of 4300 and 5500, respectively, for the two modes at room temperature.

The flexural motion of small structures like nanowires and carbon nanotubes enters the nonlinear Duffing regime already for modest driving amplitudes [39, 63] and consequently also strong coupling between flexural modes can be easily reached. To describe the nonlinear motion of the nanowire in this case, we refer to the adimensional equations describing the amplitude a of steady-state motion of one of the two perpendicular modes for a small driving force at frequency ω , with resonance frequency in the linear regime

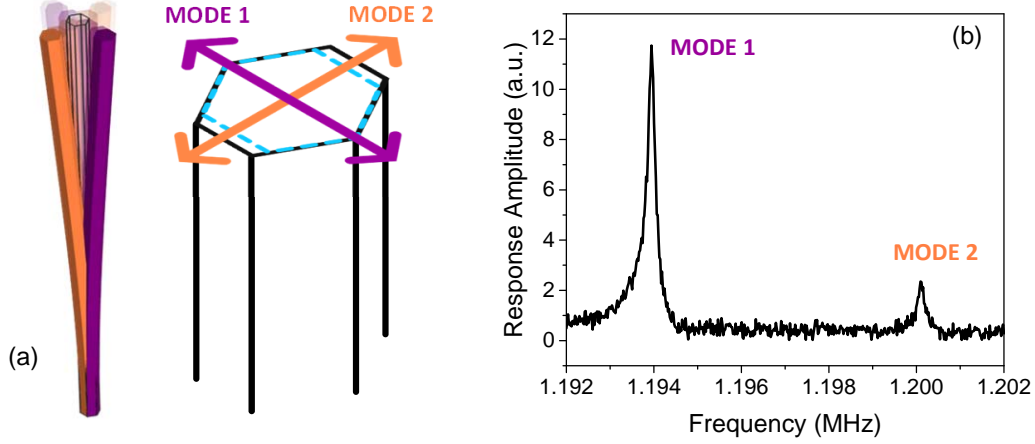


Figure 2.8 | (a) Scheme of the direction of the two modes in a nanowire with a small asymmetry in the cross-section (for reference the blue dashed line indicates a symmetric hexagon). (b) Frequency sweep at low driving amplitude showing the two mode resonances. The difference in the amplitude of the modes is related to the detection direction.

ω_1 and damping rate γ_1 derived in Section 1.5.4:

$$(\omega_1^2 - \omega^2 + i\gamma_1\omega + \tilde{\alpha}a^2 + \tilde{\alpha}b^2)a = Q_1. \quad (2.6)$$

A symmetric equation can be written for the time varying displacement of the second mode $b(t)$ with linear resonant frequency ω_2 and damping rate γ_2 . Here, $\tilde{\alpha} \equiv \left(\frac{d_1}{L}\right)^2 \int_0^1 \tilde{u}_1 (\tilde{u}_1' (\tilde{u}_1' \tilde{u}_1''))' d\tilde{s}$ is the dimensionless version of the coupling coefficient α as defined in the previous chapter, L is the length, and d_1 the diameter of the nanowire, respectively. The first flexural mode shape is denoted by $\tilde{u}_1(\tilde{s})$, where \tilde{s} is the normalized spatial coordinate along the nanowire axis. The driving term Q_1 is scaled by $C_5 \equiv \int_0^1 \tilde{u}_1(\tilde{s}) d\tilde{s}$. Note that in this equation we can neglect the other nonlinear terms proportional to b^2 with coefficient C_2 and C_3 present in Eq. 1.82 due to the fact that the cross section of our wire is almost symmetrical and thus the two bending stiffnesses in the two direction are nearly equal.

The expression between parentheses on the left-hand side of Eq. 2.6 forms a frequency-dependent response factor to the driving, where the last two terms are due to the geometrical nonlinearity and shift the resonance frequency of mode 1. The a^2 term results in a frequency shift Δf_d which is a quadratic function of the displacement of the same mode 1. This is the same frequency shift one observes for a single-mode Duffing oscillator [63]. The b^2 term describes the mode coupling and result in a frequency shift Δf_c of mode 1, which varies quadratically with the displacement of the other mode 2 [65]. A symmetric description applies to mode 2. For this wire, we calculate $\alpha = 6.4 \cdot 10^4 \text{ nm}^{-2} \text{ s}^{-2}$. A similar value of coupling coefficient was

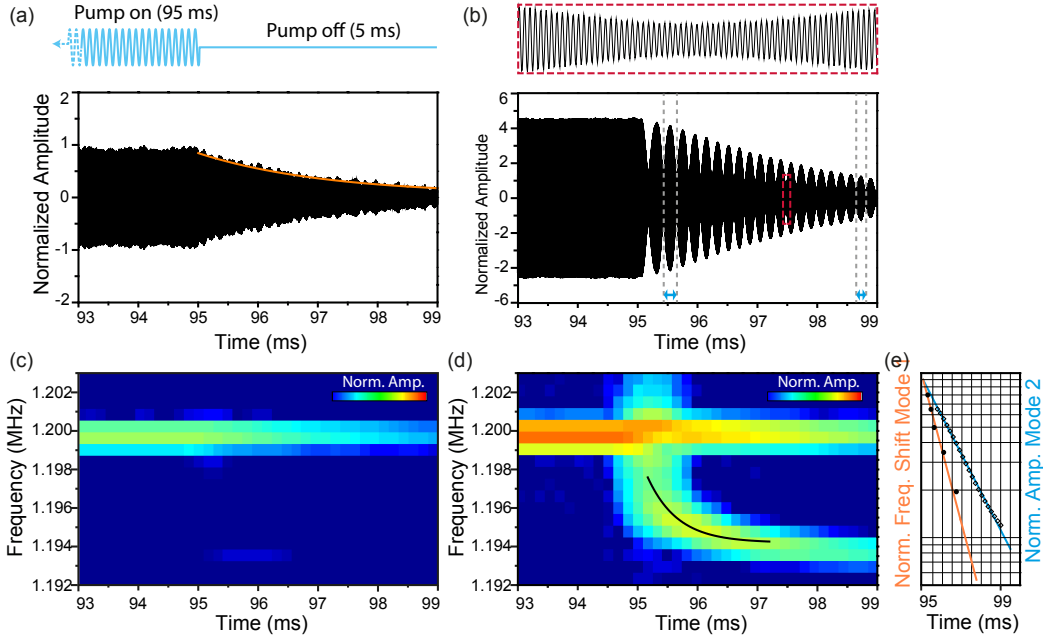


Figure 2.9 | (a) Top: excitation scheme of the ringdown measurement. Bottom: ringdown with excitation at f_2 of 100 mV. An exponential fit to the decay is given by the orange curve. (b) Ringdown measurement with excitation at frequency f_2 and amplitude 2400 mV. Blue arrows highlight the varying beating period. The top panel shows a closeup of the displacement oscillations. (c) and (d) Short time Fourier transforms of the low and high amplitude ringdown measurements of (a) and (b), respectively. In (d), as the excitation is stopped, mode 2 is in its nonlinear regime as evidenced by the broadening of the peak and a slight shift towards higher frequencies. (e) Semi-log plot of the normalized amplitude of mode 2 and the normalized frequency shift of mode 1.

found for other GaAs nanowires [63] and a slightly lower one can be found in literature for silicon nanowires [23]. This value gives a coupling strength of 2.5 kHz for an amplitude in mode 2 of just 10 nm. By comparing this value with the 250 Hz linewidth of mode 1 we can state that we are in a regime of strong coupling.

2.4.5 Mode coupling in the time domain

The frequency shift Δf_c can be clearly observed in a ringdown experiment (See top panel Figure 2.9(a)). In these measurements, a pump excitation is first applied at fixed amplitude and fixed frequency for 95 ms and then switched off, after which the decay of the excitation is observed for 5 ms. The measurement is then repeated and the results are averaged. Ringdown measurements with low driving amplitude show simple exponential decay and confirm the quality factors for both modes that were discussed before (Fig. 2.9(a)). Next, we perform ringdown measurements at a higher driv-

ing amplitude at frequency f_2 . Now a clear beating pattern is visible in the averaged time trace (See Fig. 2.9(b)). The frequency of the beating is not constant in time, but tends towards $f_2 - f_1$ at the end of the decay. Qualitatively, this beating can be understood as follows: for high enough driving amplitudes, mode 1 is shifted enough in frequency through the coupling to overlap the pump frequency. Hence this mode is also excited at the pump frequency. During the second part of the ringdown measurement, both modes decay at their own, time-dependent characteristic frequencies, resulting in beating. At the beginning of the decay, mode 2 oscillates at a high amplitude, causing mode 1 to be pulled to a higher frequency, i.e. closer to f_2 , thus reducing the beating frequency. As the amplitude of mode 2 decays, mode 1 moves back towards f_1 and the beating frequency therefore increases towards $f_2 - f_1$.

In Figs. 2.9(c) and (d) short-time Fourier transforms of the ringdown measurements are plotted. For low driving amplitude only a frequency component at f_2 is present, during both the excitation and decay parts of the measurement. For high driving amplitude, an additional frequency component develops at the time the excitation is stopped. This component is spectrally broad in the beginning, but over time narrows and shifts towards f_1 , making it clear that it corresponds to an excitation of mode 1. As described by Eq. 2.6, Δf_c is a quadratic function of the amplitude of mode 2, which decays exponentially with time constant $\tau_2 = 1/\gamma_2$. In Figure 2.9(e) the frequency shift of mode 1, as well as the amplitude of mode 2, is plotted as a function of time. Indeed, we find that Δf_c decays as e^{-2t/τ_2} , i.e. twice as fast as the amplitude of mode 2, confirming the nonlinear nature of the observed mode coupling.

When the pump excitation is applied on resonance with mode 1, no beating pattern is observed, regardless of driving amplitude. This is consistent with the previous explanation, since in this case the pump drive pushes mode 2 away from f_1 , leading to no overlap of that mode with the excitation.

2.4.6 Frequency swept Pump-probe measurements

To investigate the dependence of Δf_c on the displacement of the pumped mode in more detail, we perform pump-probe measurements. In the leftmost panel of Figure 2.10, the response of mode 1 is probed by sweeping with a weak excitation, while mode 2 is driven with a pump excitation, which is high enough to reach the nonlinear regime. Stepping the pump frequency changes the displacement of the pumped mode according to its frequency response function and, through the mode coupling, maps this response function onto the frequency shift of the other mode. In the right panel of Fig. 2.10 the squared and normalized frequency response of mode 2 is plotted (black

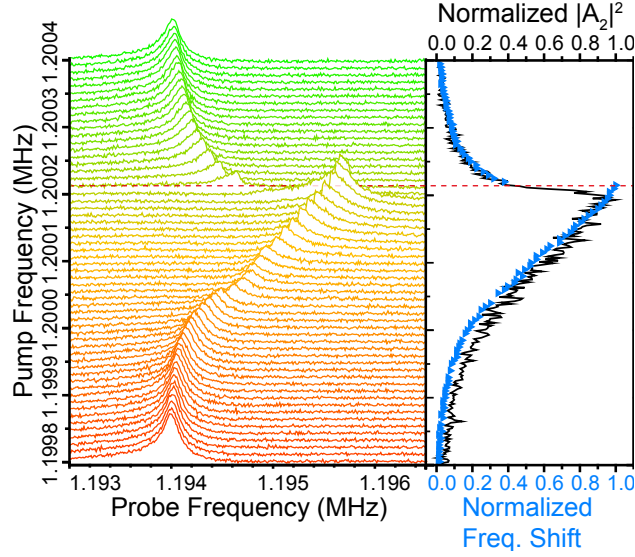


Figure 2.10 | Left Panel: Frequency response of mode 1 for different pump frequencies around f_2 , with driving amplitude 600 mV. Right Panel: Squared and normalized frequency response of mode 2, at driving amplitude 600 mV (black curve). Plotted on top are frequency shifts for maximum displacements of the mode 1 extracted from the left panel (blue triangles).

curve), for the same driving amplitude as used in the left panel. Plotted on top of this (blue triangles) are the frequency shifts of the maximum response of mode 1, as shown in the left panel. The agreement between the curves confirms the quadratic dependence of the frequency pulling effect.

The shape of the resonance of the probed mode changes as the pump frequency is stepped. This provides a way to tune the effective nonlinearity of one mode by precisely controlling the motion in the other, orthogonal mode. Using perturbation theory, one can write the effective nonlinearity constant of a mode in terms of the derivative of the squared displacement in the other mode with respect to the driving frequency:

$$\tilde{\alpha}_{\text{eff}} = \tilde{\alpha} \left(1 - \tilde{\alpha} \frac{\partial |b|^2}{\partial \omega} \right) \quad (2.7)$$

Mode 2 shows a jump in its response around the frequency indicated in Fig. 2.10 by the red dashed line. Due to this effect, the last term in Eq. 2.7 changes sign at this frequency, resulting in a negative effective nonlinearity (sharkfin-shape with jump on lower flank) of the probed mode for lower pump frequencies and a positive effective nonlinearity (sharkfin-shape with jump on higher flank) for higher pump frequencies.

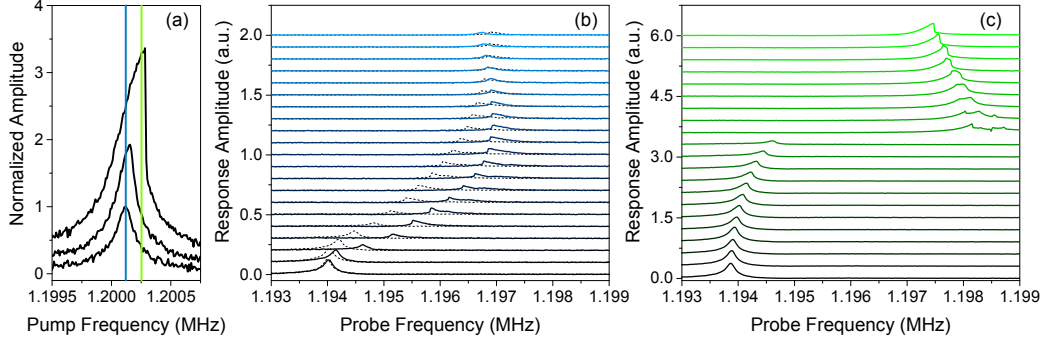


Figure 2.11 | (a) Pump-probe measurement scheme with the pump drive at two different fixed frequencies: at the resonance frequency of mode 2 in the linear regime (blue line) and at a frequency higher than the critical frequency of mode 2 in the nonlinear regime (green line). (b) Frequency response sweeps of the probed mode with the pump amplitude increasing from bottom to top. The solid and dashed black lines correspond to pumping with PZT2 and PZT1 (see Fig. 2.3), respectively. (c) Frequency sweeps of the probed mode with the pump drive frequency as indicated by the dashed green line in (a)

2.4.7 Amplitude swept Pump-probe measurements

Similarly, the amplitude response function of the pumped mode can be mapped onto the frequency shift of the other mode by stepping the pump amplitude at fixed frequency. Figure 2.11(a) displays the frequency response functions of mode 2 in the linear and nonlinear regime. Fixing the pump frequency at f_2 and varying the pump amplitude, results in frequency shifts of mode 1 as shown in Fig. 2.11(b). In Fig. 2.11(c), the pump frequency is set to a value higher than f_2 . Varying the pump amplitude initially results in a small, quadratic frequency shift of mode 1. As the pump amplitude is increased, mode 2 enters its nonlinear regime and becomes bistable, showing a jump in its response at a frequency that increases with increasing pump amplitude. For high enough amplitude, this frequency reaches the pump frequency, allowing mode 2 to jump to its high-amplitude branch. This jump is observed as a corresponding jump in frequency shift of mode 1.

For relatively low displacements of mode 2, the frequency shift in both cases shows a quadratic dependence (see Fig. 2.12). The deviations from this behavior at higher pump amplitudes are most likely related to optical compression in the interferometric detector, as well as mechanical mixing due to the presence of both pump and probe drives, and possibly due to the wire entering a strong bending regime of motion [66]. We confirm the orthogonal nature of the two modes by using two perpendicularly mounted PZTs to drive the pump excitation (as shown in Fig. 2.3). From the magnitude of the frequency shifts (solid and dashed data sets in Fig. 2.11(b), for PZT2 and PZT1, respectively) we infer that PZT2 drives mode 2 more than PZT1.

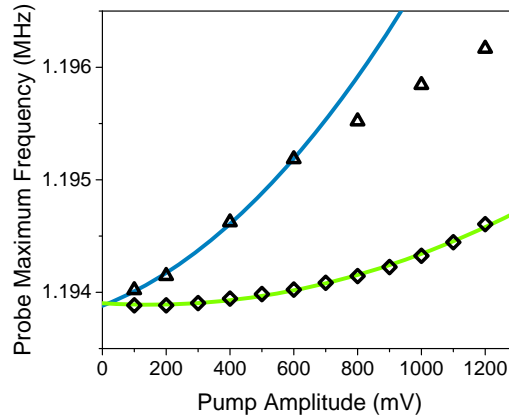


Figure 2.12 | Frequency of maximum response of probed mode plotted as function of pump amplitude, for relatively low pump amplitudes. The two solid lines are a fits to a quadratic function.

Similarly, by probing the response of mode 1 with each PZT, we determine that PZT1 drives mode 1 harder than PZT2.

2.5 Mechanical Logic

The ability to map the displacements and oscillation frequencies of one mode onto the frequency of another mode can be used to implement amplitude to frequency conversion, frequency modulation, and frequency tuning. This type of mode coupling and nonlinearity can also be used to perform mechanical logic. As a proof-of-principle, we demonstrate mechanical OR and NOR gates. The hysteresis due to the nonlinearity of the modes also provides a straightforward way to store these logical output states [31, 32].

Due to the Duffing nonlinearity, when sweeping the driving amplitude at fixed frequency f_2 , we observe a high jump between two levels in the response amplitude of mode 2, at a critical driving amplitude. These two levels in the response are used to encode logical 0 and 1 output states. The two inputs correspond to two signal voltages which are summed and subsequently applied to the driving PZT. Logical 0 and 1 input states are defined by low and high driving voltages, respectively (See Fig. 2.13(a)). As shown in Fig. 2.13(b) (upper panel), we obtain a high response when one or both inputs are high (01, 10, or 11) and a low response when both input signals are low (00). This is therefore a realization of a logical OR gate. This OR gate is converted into a NOR gate by taking as output the response amplitude of mode 1 at f_1 (lower panel Fig. 2.13(b)). When mode 2 is at the low level (for input 00) there is almost no interaction between the two modes and we have the maximum response (logical 1) of mode 1 at the readout frequency.

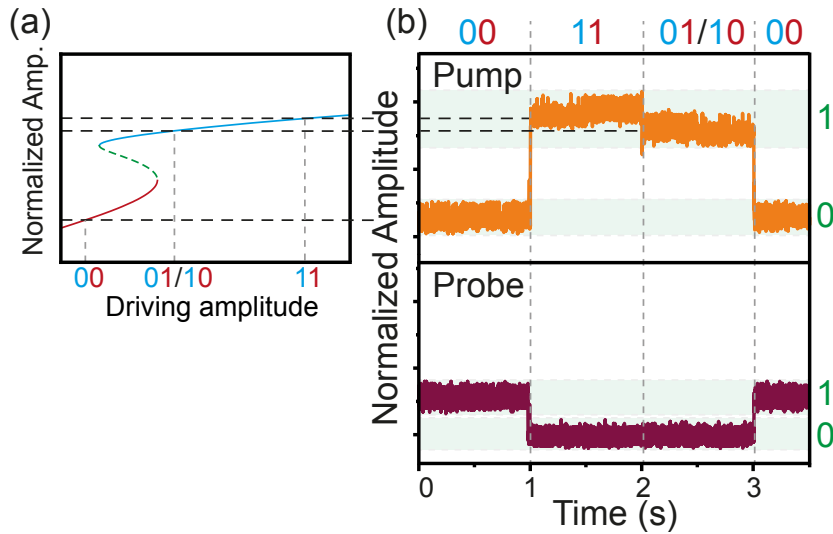


Figure 2.13 | (a) Simulated amplitude response curve of a Duffing oscillator, displaying its bistable regime of motion. Dashed black lines highlight the driving amplitudes needed to create OR and NOR gates. (b) Top panel: response amplitude of mode 2 as a function of time, for the four combinations of two logical inputs, as indicated by the numbers on top. Bottom panel: response amplitude of mode 1 as a function of time, for the same logical inputs.

When instead the amplitude of mode 2 is high (for 01, 10, and 11), mode 1 shifts to a higher frequency and the logical output is 0.

2.6 Vectorial scanning with GaAs nanowires

2.6.1 Introduction

The duality of the fundamental flexural modes of a single nanowire can also be exploited in the linear regime leading to interesting applications in scanning probe microscopy. In the pendulum geometry, when the long axis of the nanowire is perpendicular to the scan surface (see Fig. 2.14), these modes can be used for the simultaneous detection of in-plane forces and spatial force derivatives along two orthogonal directions [28]. Although one-dimensional (1D) dynamic lateral force microscopy can be realized using the torsional mode of conventional AFM cantilevers [67–71], the ability to simultaneously image all vectorial components of nanoscale force fields is of great interest. Not only would it provide more information on tip-sample interactions, but it would also enable the investigation of inherently 2D effects, such as the anisotropy or non-conservative character of specific interaction forces.

In the case of high-Q resonators such as our nanowires, the splitting between the modes, is likely to be many times their linewidths, a property observed

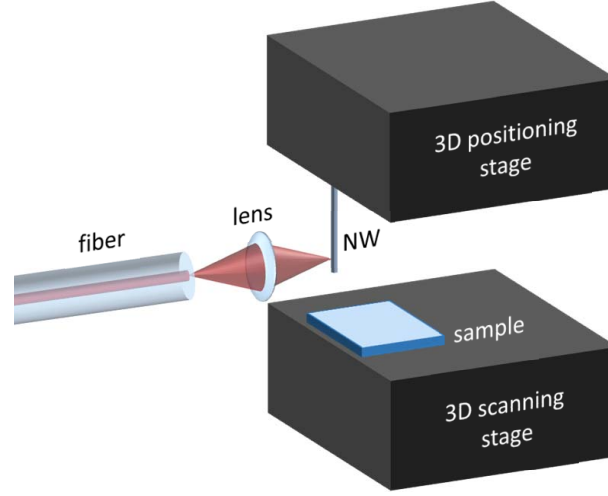


Figure 2.14 | Sketch of the setup used for the vectorial scanning with NWs.

in several measured NWs. We can resolve the two first-order flexural modes with different signal-to-noise ratio as already seen in Fig. 2.8(b), given that the principal axes of the displacements $u(s, t)$ and $v(s, t)$ of the modes are rotated by some angle θ_0 with respect to the optical detection axis x_d [1]. Although we only measure NW displacement projected along x_d , displacement along other directions in the xy -plane are also accessible by aligning the interferometer beam slightly off-center with respect to the NW's central axis [28, 72]. Experimentally we find that when the optical detection axis is aligned with the NW's central axis, thermal motion in a direction perpendicular to the detection axis falls below our detection sensitivity. Hence, the total measured displacement is $x(t) = a(t) \sin \theta_0 + b(t) \cos \theta_0$, where a and b represent the displacement of each flexural mode. The mean square displacement generated by uncorrelated thermal noise is then $\langle x^2 \rangle = P_1 + P_2$, where $P_1 = \langle a^2 \rangle \sin^2 \theta_0$ and $P_2 = \langle b^2 \rangle \cos^2 \theta_0$ represent the integrated power of each measured resonance in the spectral density. Given that the motional mass of the two orthogonal flexural modes is the same, using the equipartition theorem, we find the ratio of their mean-square thermal displacements $\langle a^2 \rangle / \langle b^2 \rangle = f_2^2 / f_1^2$. Therefore, from the measured thermal peaks in the spectral density, we calculate the angle $\theta_0 = \arctan \left(\frac{f_1}{f_2} \sqrt{\frac{P_1}{P_2}} \right)$ between a and x_d . Furthermore, since $k_1 = k_B T / \langle a^2 \rangle$ and $k_2 = k_B T / \langle b^2 \rangle$, we obtain the spring constants of each flexural mode, which are typically on the order of 10 mN/m. These parameters yield mechanical dissipations $\Gamma_i = k_i / (2\pi f_i Q_i)$ with $i = 1, 2$ and thermally limited force sensitivities $S_{F_i}^{1/2} = \sqrt{4k_B T \Gamma_i}$ around 100 pg/s and 5 aN/ $\sqrt{\text{Hz}}$, respectively.

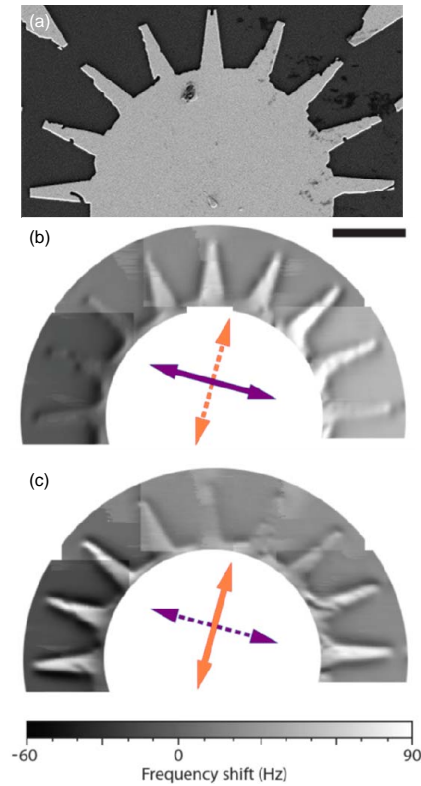


Figure 2.15 | (a) SEM image of the sample used for scanning. Gold fingers are patterned radially on a semicircle on a Si substrate. (b) and (c) frequency shift of Mode 1 and 2 respectively. It appears clear how topographic features perpendicular to the direction of oscillation of each mode are better resolved. The scale bar is $5\mu\text{m}$.

2.6.2 Two-mode scanning probe microscopy

In order to use the NW as a scanning probe, we approach the sample and scan it in a plane perpendicular to the axis and in proximity of the NW tip. By monitoring the NW's mechanical properties, i.e. the frequency, dissipation, and orientation of its doublet modes, we image the sample topography via the tip-sample interaction. Such microscopy can be accomplished by measuring the NW thermal displacement spectral density as the sample surface is scanned below it. Although such a measurement provides a full mechanical characterization of the modes, it is time-consuming due to the small displacement. A technique more amenable to fast spatial scans uses the resonant excitation of the doublet modes through two independent phase-locked loops (PLLs) to track both frequencies simultaneously. Fig. 2.15 shows the frequency shifts $\Delta f_1(x, y)$ and $\Delta f_2(x, y)$ of the doublet modes as a sample is scanned below the tip of NW1. The sample consists of nine $5\text{-}\mu\text{m}$ long and 200-nm thick finger gates of Au on a Si substrate, radially disposed and

equally spaced along a semicircle. The finger gates and their tapered shape are intended to provide edges at a variety of different angles, highlighting the directional sensitivity of the orthogonal modes. The measurement in Fig. 2.15 is performed using the PLLs with an oscillation amplitude of 6 nm. The spatial scan is performed at a distance of 70 nm from the Au surfaces without feedback to maintain a constant tip-sample separation, i.e. in "open-loop". The Au gates are grounded during the measurement. The frequency shift images clearly delineate the topography of the patterned sample, with each mode showing stronger contrast for features aligned along orthogonal directions. Edges, i.e. large topographical gradients, pointing perpendicular (parallel) to the mode oscillation direction appear to produce the strongest (weakest) contrast. Tip-sample interactions producing the frequency shifts in non-contact Atomic Force Microscopy (AFM) can include electrostatic, van der Waals, or chemical bonding forces depending on the distance. In our case, because of the large spacing, they are dominated by electrostatic forces [73].

2.7 Coherent dynamics in a NW

In coupled two-level systems, energy can be coherently exchanged between the two states. While coherent dynamics of coupled systems has been studied mainly in the regime of quantum physics, many concepts have counterparts and can be translated in the classical regime. When coupled, the two fundamental modes of our NW make a perfect example of a classical system where coherent dynamics can take place. When an electric field is applied in proximity of the NW, additional forces due to charges on the NW and its polarizability are acting on the NW. The gradient of these force fields modify the dynamics of the wire, effectively producing a controllable coupling between the mode doublet. For certain conditions of the field it is possible to observe hybridization of the modes and avoided crossing. Avoided crossing with a splitting larger than the sum of the linewidths of the individual resonances is a signature of strong coupling. By achieving strong coupling between the two modes of our NWs, it is then possible to exchange energy between the modes through the quantum analogue of driven Rabi oscillations. Rabi oscillations in a coupled two-level system, can be achieved through periodic modulation of the frequency detuning [74]. By applying a time-varying voltage with frequency close to the frequency difference between the two modes it is possible to achieve a coherent oscillation in the mode population by applying definite pulse sequences. Coherent pulse sequences analogue to quantum control techniques can be applied offering advantages in different applications, including sensing. For example, coherent pulse sequences offer

the potential to increase the stability of mechanical resonators, increasing their sensitivity. In recent reviews, in fact, it has been observed that frequency fluctuations in silicon nanoresonators remain much higher than the thermal limit [75]. Dynamical decoupling pulse sequences could offer a way to reduce these frequency fluctuations, potentially reaching the thermal limit.

3 | Optomechanics with photonic wires

3.1 Introduction

Coupling a microscopic mechanical resonator to a nanoscale quantum system enables control of the mechanical resonator via the quantum system and vice-versa. The coupling is usually achieved through functionalization of the mechanical resonator, but this results in additional mass and dissipation channels. An alternative is an intrinsic coupling based on strain. In this Chapter we are going to study the intrinsic coupling within a monolithic semiconductor system: the nanoscale quantum system is a semiconductor QD located inside a nanowire.

Position read-out of the mechanical resonator is usually carried out by incorporating the mechanical resonator in an optical cavity [76] as we have seen also in the previous Chapter. We pursue an alternative here, position read-out by embedding a single photon emitter into the mechanical resonator itself.

A coupling between a QD exciton (an electron-hole pair) and a mechanical oscillator was observed in two recent experiments [8,9]. There, the read-out signal resulted from the non-resonant excitation of the QD. This is not an ideal situation since the quality of the emitted photons is low (as inferred from a large spectral linewidth and low indistinguishability). The mechanical resonator was driven externally and shifts in the QD's luminescence spectrum were demonstrated. While this non-resonant excitation scheme is sufficient for a first characterization of the coupling strength, it severely limits the potential of the device in sensing applications, and cannot be exploited to manipulate the mechanical oscillator.

3.2 Photonic Trumpet

GaAs is a natural choice of material also for this endeavour. First, GaAs mechanical resonators are easy to make and have good mechanical proper-

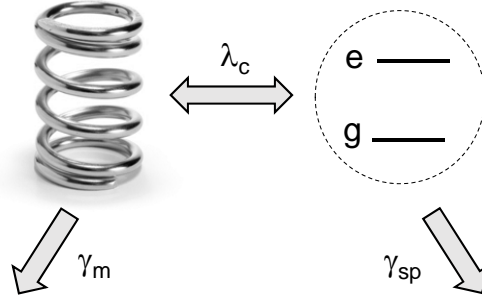


Figure 3.1 | Sketch of the hybrid system: a mechanical oscillator is coupled to a two-level quantum system. The coupling rate λ_c competes with the dissipation rates of both components: the intrinsic phonon relaxation rate γ_m and the spontaneous emission rate of a photon γ_{sp} .

ties [77, 78]. Second, a self-assembled QD in GaAs represents an excellent single photon emitter. At low temperature with resonant excitation, a quantum dot is a fast, bright and pure source of single photons [79–84], outperforming any other solid-state emitter. A crucial feature is that the quantum dot transition frequency is sensitive to the strain induced by a deformation of the host material: there is an inherent coupling between the mechanics and the optical properties of the single photon emitter [13]. Our quantum emitter consists of a self-assembled InAs QD grown by molecular beam epitaxy. It is embedded 110 nm away from the sharp end of a $12\mu\text{m}$ long conical photonic wire (PW) standing on a gold substrate [85], see Fig. 3.2. At the QD position, the small diameter enhances the coupling of the emitter to the guided modes while screening its coupling to lateral free-space modes [86]. As the top facet is approached, the progressive increase in diameter allows for an adiabatic expansion of the guided modes allowing good matching to a Gaussian mode in free-space [87] leading to large coupling with optical fiber, resulting in very large photon extraction efficiencies. While it is possible to obtain gaussian profiles in free space also with a tip-like wire (where the tapering reduces the diameter of the wire approaching the top end), the photonic trumpet’s performance is more robust to variations of fabrication parameters. Importantly, we note that the large and flat top facet, which neither clips nor depolarizes the excitation beam, allows for excellent suppression of the back-scattered light from the resonant laser. This solves an important challenge associated with the resonant spectroscopy of nano-sized (sub-wavelength) structures as will be also discussed later in Section 3.3. The mechanical system, a semiconductor nanowire with a conical taper, a “photonic trumpet” [85], has been carefully selected to optimize both mechanical and optical properties simultaneously. The extra mass located at the end facet of the nanowire produces large strains in the “stem” of the nanowire

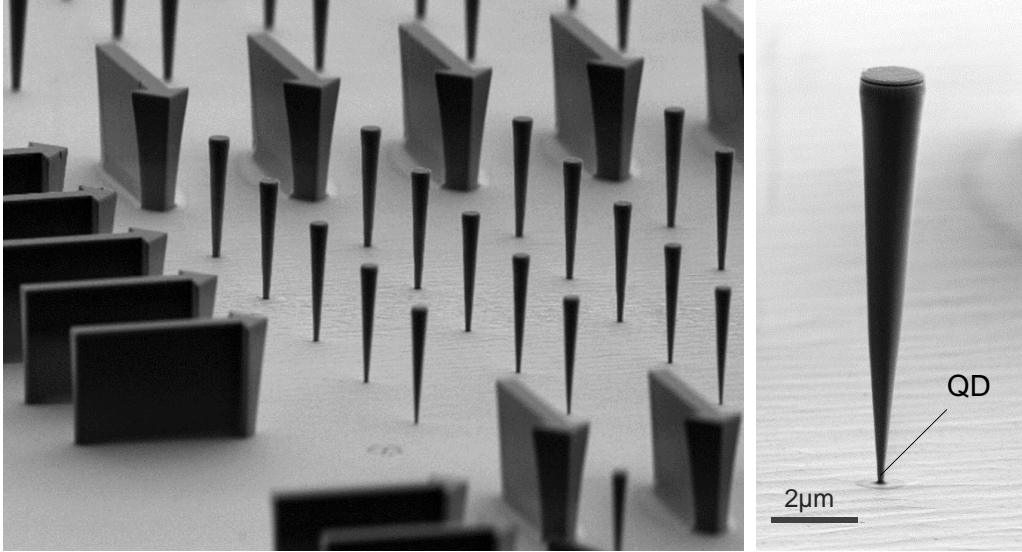


Figure 3.2 | SEM images of the photonic trumpets. A QD is embedded close to the bottom of a micrometer-sized mechanical resonator. The coupling originates from strain as the nanowire oscillates.

where the QD is located, resulting in large couplings between the QD and the mechanical resonator. These conical wires, in contrast to the NWs studied in Chapter 2, are obtained through a top-down approach. Using e-beam lithography, a Ni hard mask consisting of arrays of disks with variable diameters is defined. This is followed by a deep plasma etch conducted in a reactive ion-etching chamber. Finally, the remaining Ni mask is removed in a diluted nitric acid solution. A Si_3N_4 anti-reflection coating maximizes the transmission through the top facet. The wire is then clamped to a bottom gold-silica mirror via a flip-chip procedure [85].

3.3 Experimental Results

3.3.1 Resonant spectroscopy of a QD coupled to a mechanical resonator

The QD–mechanical coupling manifests itself as a time-dependent frequency shift of the QD transition as the resonator oscillates. The frequency shift is determined by the strain coupling λ_c [8, 9] (Fig. 3.1). This is described by the interaction Hamiltonian

$$\hat{H}_{\text{int}} = \frac{\hbar\lambda_c}{u_{\text{zpf}}} \hat{u} \hat{\sigma}_z, \quad (3.1)$$

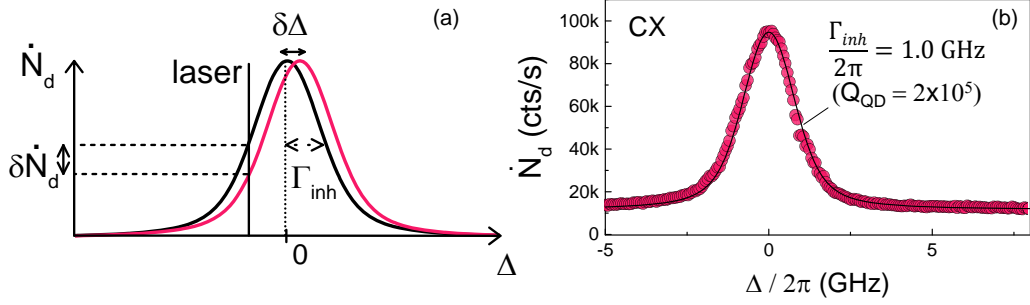


Figure 3.3 | (a) Effect of the coupling: a displacement u of the nanowire produces a shift $\delta\Delta$ in the QD frequency, modifying the detuning between the QD and the laser. Γ_{inh} is the linewidth of the QD, inhomogeneously broadened by spectral fluctuations. (b) Resonance fluorescence signal from the charged exciton (CX) as a function of laser detuning (fluorescence wavelength: 945.6 nm). $\Omega_R \simeq \gamma_{sp} = 1.1$ GHz. The fit uses a Voigt profile with a contribution to the linewidth of 0.45 GHz from the Lorentzian part, and 0.70 GHz from the Gaussian one.

where the Pauli operator $\hat{\sigma}_z = \frac{1}{2}(|e\rangle\langle e| - |g\rangle\langle g|)$ acts on the QD two-level system, \hat{u} is the operator representing the nanowire's displacement, u_{zpf} corresponds to the quantum zero-point fluctuations and $\lambda_c = \frac{\partial\Delta}{\partial u}u_{zpf}$. To read out the displacement of the mechanical resonator, we drive the optical transition of an embedded QD with a linearly polarized narrow band laser and collect the scattered light in the orthogonal polarization [88]. By doing so we detect the resonance fluorescence (RF) from the QD and limit the amount of back-scattered laser light. The challenge with resonant spectroscopy is to distinguish between the fluorescence signal and the back-scattered laser light. For this we use a dark-field microscope based on cross-polarized excitation and detection. This technique ensures extinction ratios as high as 10^7 upon reflection on a flat surface [88]. The situation is however more complex when the QD environment is processed below the micro-meter scale: a small object in the focus of the incident laser causes depolarization of the reflected beam and prevents efficient rejection. The photonic trumpet here assumes a crucial role, as it assures the need for a flat facet with the nano-scale environment of the QD. For the specific photonic trumpet studied here (bottom diameter 300 nm, top diameter $1.62\mu\text{m}$, see Fig. 3.2(b)), we achieve a laser suppression > 40 dB over a 29 GHz frequency span with fixed settings of the polarizers. This results in a signal to noise ratio $S : N = 125$ at a driving amplitude $\Omega = \gamma_{sp}$.

A displacement u of the mechanical oscillator results in a detuning Δ of the QD with respect to the constant frequency laser and translates into a change $\delta\dot{N}_d$ in the detected RF count rate (Fig. 3.3(a)). Assuming small

optical detunings due to the mechanical oscillation,

$$\delta\dot{N}_d = \frac{\alpha_c \hbar \lambda_c}{u_{zpf}} u, \quad (3.2)$$

where $\alpha_c = \partial\dot{N}_d/\partial\Delta$ depends on the spectral profile of the emitter.

The typical spectrum from a QD inside our wire is shown in Fig. 3.3(b). It is obtained from an excitation with two lasers: a very weak non-resonant laser is used to stabilize the QD's charge environment [89] while a second laser scans the QD transition. We observe a maximum in the resonance fluorescence as the second laser hits the QD resonance ($\Delta = 0$), on top of a photoluminescence background associated with the non-resonant pump. In order to reach the best sensitivity of the QD to the mechanical motion, we have to maximize the count rate while maintaining a small linewidth. For this we operate at the onset of power broadening (Rabi coupling $\Omega_R \simeq \gamma_{sp}$, with $\gamma_{sp} = 1.1$ GHz, the spontaneous emission rate of the QD). This results in a linewidth $\Gamma_{inh}/2\pi = 1.0$ GHz (Fig. 3.3(d)) corresponding to an ‘‘optical quality factor’’ $Q = 2 \times 10^5$.

3.3.2 Resonance Fluorescence noise spectrum

One measurement technique to detect the mechanical motion is to record a time-trace $\dot{N}_d(t)$ of the QD RF at a fixed laser detuning Δ , Fig. 3.3(a), and perform a Fourier analysis on the data [90]:

$$\bar{S}_{NN}(f) = 2 \text{FT} \left[\frac{\dot{N}_d(t)}{\langle \dot{N}_d(t) \rangle} \right]^2 \frac{t_{\text{bin}}^2}{T}, \quad (3.3)$$

where t_{bin} is a post-selected binning time, T is the total integration time and $\langle \dot{N}_d(t) \rangle$ is the average number of counts per bin. Fig. 3.4(a) shows $\bar{S}_{N_d N_d}$, the normalized noise power spectral density (NPSD), computed from a 20 minute time-trace recorded at $\Delta = \Gamma_{inh}$. The spectrum reveals two sharp resonances, labeled F_{1y} and F_{1x} , at $\omega_{m,F_{1y}}/2\pi = 512.8$ kHz and $\omega_{m,F_{1x}}/2\pi = 607.9$ kHz, respectively. These resonances, which are absent in the bulk sample, correspond to the thermally-driven mechanical resonances, i.e. the Brownian motion at 4 K. Specifically, we observe the two first order flexural modes, whose degeneracy is lifted by a slightly anisotropic cross section.

From the assumption that the oscillator is fully thermalized with the surrounding He bath we determine the strength of the strain coupling. Using the equipartition theorem,

$$\langle u^2 \rangle = \frac{k_B T}{m_{\text{eff}} \omega_m^2} = u_{\text{th}}^2. \quad (3.4)$$

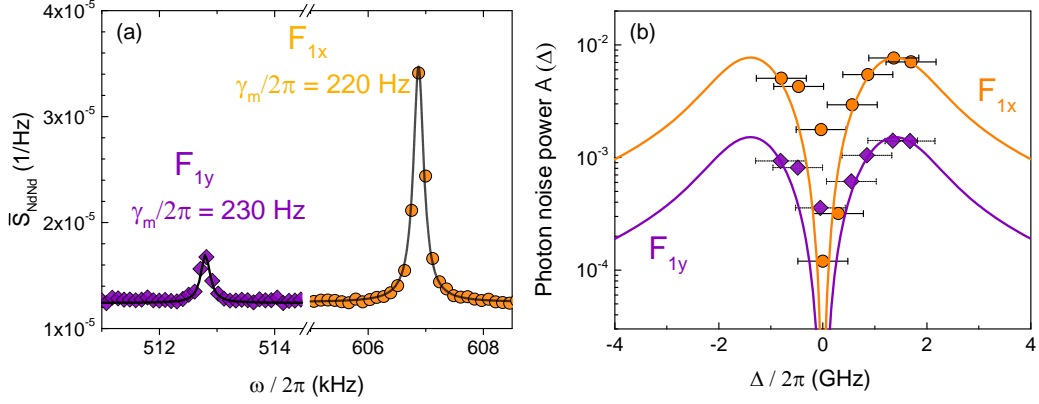


Figure 3.4 | (a) Photon noise power spectral density (NPSD) recorded at detuning $\Delta = \Gamma_{inh}$ (integration time 20 min). The resonances correspond to Brownian motion of the first order flexural modes. The background corresponds to the shot noise level. (b) Photon noise power \mathcal{A} as a function of laser detuning for F1x (orange circles) and F1y (purple diamonds). The solid lines are fits to the experimental data with λ_c as the only free parameter.

In addition, we have from Eq. 3.2

$$\langle u^2 \rangle = \frac{u_{zpf}^2}{\alpha_c^2 \lambda_c^2} \langle \delta \dot{N}_d^2 \rangle, \quad (3.5)$$

with α_c the derivative of the QD spectrum. We introduce the normalized photon noise spectrum \bar{S}_{NN} ,

$$\langle \delta \dot{N}_d^2 \rangle = \langle \dot{N}_d \rangle^2 \int \bar{S}_{NN}(f) df, \quad (3.6)$$

where $\int \bar{S}_{NN}(f) df = \mathcal{A}$ is the photon noise power. We obtain \mathcal{A} for each mode from the area below the corresponding peak in the power noise spectrum (Fig. 3.4(a)). This yields the equation to describe the experimental data in Fig. 3.4(b):

$$\mathcal{A}(\Delta) = \left(\lambda_c \frac{u_{th}}{u_{zpf}} \frac{\alpha_c(\Delta)}{\langle \dot{N}_d(\Delta) \rangle} \right)^2, \quad (3.7)$$

which only depends on λ_c . We point out that the approximation is not only realistic (our sample is located in He exchange gas) but also verified using the QD itself, which represents a sensitive thermometer. In particular, we observe no shift of the resonance as we increase the power of resonant and non-resonant lasers up to saturation. We note that u_{th} and u_{zpf} , corresponding to the thermal and zero-point fluctuations respectively, depend in particular on the characteristics of the mechanical resonator, namely its mode frequency and motional mass. The former is obtained from our measurement while the latter is determined through a finite element simulation of

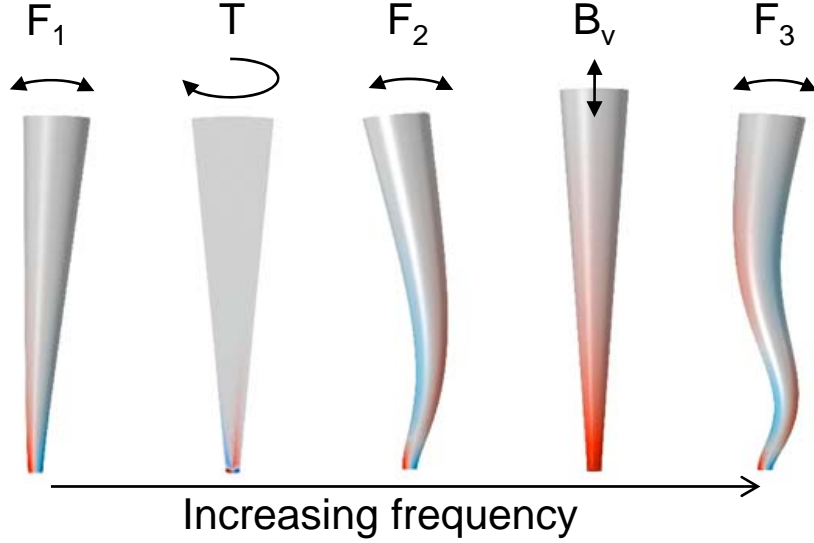


Figure 3.5 | The mechanical modes: F_1 , F_2 and F_3 correspond to the first, second and third order flexural modes; T to a torsional mode and B_v to a vertical breathing mode. The colour map represents the strain along the vertical axis within the trumpet (red: tensile, blue: compressive). The black arrows represent the displacement of the nanowire's top facet.

the resonator. u_{th} depends on the mode temperature, taken as 4 K assuming thermalization of the oscillator to the He bath (see also section 3.3.5). For the first flexural mode we find $u_{zpf} = 2.3 \times 10^{-14}$ m and $u_{th} = 1.2 \times 10^{-11}$ m. The detuning dependence of $\langle \dot{N}_d(\Delta) \rangle$ and $\alpha_c(\Delta)$ are obtained from a fit of the RF spectrum in Fig. 3.4(a) so that Eq. 3.7 eventually only depends on the strain coupling λ_c . Using $\lambda_{c,F_{1x}}/2\pi = 280$ kHz and $\lambda_{c,F_{1y}}/2\pi = 55$ kHz, we find good agreement with the experimental data. The bandwidth of this measurement protocol is limited by the detector's dead-time. In our case, this means a cut-off at a frequency of 10 MHz.

3.3.3 FEM simulations

To confirm the origin of the resonances in our noise spectrum, we calculate the mechanical eigen-frequencies of the resonator using a commercial finite-element analysis software (Comsol). We simulate a $12\mu\text{m}$ long GaAs wire, with a bottom diameter of approximately 300 nm and a tapering angle of $\theta = 3^\circ$. In order to adjust the mechanical frequencies to the experimental values, we allow a 5% variation in the length of the wire (arising from flux inhomogeneities over the wafer surface in the molecular beam epitaxy chamber). To account for the observed splitting of the first flexural mode, we also introduce a small asymmetry in the QD plane. In practice, the nanowire has a round top diameter but an elliptic base, the consequence of a slightly

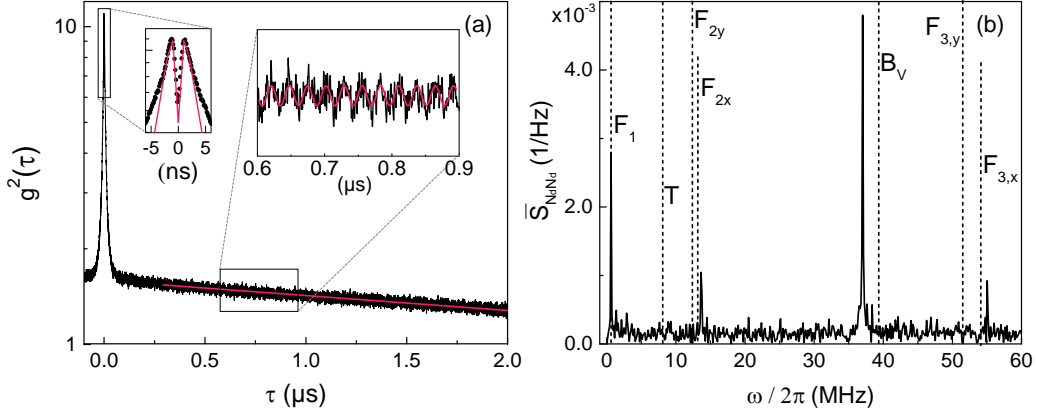


Figure 3.6 | (a) Auto-correlation function recorded at $\Delta \simeq \Gamma_{\text{inh}}$ (the entire data extends over $8\mu\text{s}$). The oscillation in the right inset results from the mechanically induced modulation in count rate (the fit is a sine with a period of 27 ns). The fit in the left inset (red solid line) corresponds to a perfect single photon emitter subject to blinking ($\Omega_R = \gamma_{\text{sp}}$) and includes the timing jitter of the detectors (500 ps). (b) In black, the noise power spectral density obtained from the Fourier transform of the auto-correlation measurement. The black dotted lines correspond to the resonance frequencies obtained from a simulation.

anisotropic etching process ($\Delta\theta = \theta_x - \theta_y$). Fig. 3.5 shows the results for a $11.4\mu\text{m}$ long wire, with a top diameter of $1.62\mu\text{m}$ and a bottom section with minor axis $b_{d,y} = 260\text{ nm}$ and major axis $b_{d,x} = 320\text{ nm}$ ($\Delta\theta = 0.15^\circ$, corresponding to the estimation of the anisotropy in the etching process [9]).

3.3.4 Auto-correlation function

To probe the strain coupling in the MHz range, we record the auto-correlation function $g^{(2)}(\tau) = \frac{\langle \dot{N}_d(t)\dot{N}_d(t+\tau) \rangle}{\dot{N}_d(t)^2}$ of the RF signal with two detectors in a Hanbury Brown-Twiss configuration [91]. Fig. 3.6(a) shows the result from a 70 min measurement recorded at $\Delta = \Gamma_{\text{inh}}$. The dip at zero delay is the signature of single photon emission from the QD. Its moderate depth is a consequence of the timing jitter of the detectors (note that the dip is narrowed by the unresolved Rabi oscillations induced by the amplitude of the drive, $\Omega_R \sim \gamma_{\text{sp}}$). The bunching peak at short delays ($\tau < 100\text{ ns}$) is related to a blinking in the QD emission [92]. The peak value increases as the on:off ratio in the QD emission diminishes; the decay time of the bunching is a measurement of the correlation time of charge fluctuations in the QD environment [93]. In addition to these features, we observe a small oscillation, with a period of about 25 ns, which runs over the entire $8\mu\text{s}$ time-span of the experiment. This oscillation corresponds to the signature of the strain coupling in the photon counting regime.

Mode	ω_m (MHz)	u_{th} (pm)	ϵ_{zz}	ϵ_{yy}	ϵ_{xx}
F _{1x}	0.61	12	4.5×10^{-8}	-1.3×10^{-8}	-1.5×10^{-8}
T	8.2	1.2	1.4×10^{-11}	-1.1×10^{-11}	-7.5×10^{-12}
F _{2x}	13.4	0.45	3.0×10^{-8}	-8.1×10^{-9}	-9.7×10^{-9}
B _v	40.0	0.14	7.0×10^{-8}	-2.1×10^{-8}	-1.9×10^{-8}
F _{3x}	55.0	0.10	2.3×10^{-8}	-6.3×10^{-9}	-7.6×10^{-9}

Table 3.1 | The QD is located 35 nm away from the centre (black star in Fig. 3.7(a)). The strain values are given for a displacement of the top facet equal to the time-averaged displacement u_{th} at $T = 4.2$ K.

A Fourier analysis of the intensity correlation data at $\tau > 0.25\mu\text{s}$ is shown in Fig. 3.6. The spectrum reveals a whole series of resonances corresponding to different modes of the mechanical resonator. In particular, the lower frequency mode corresponds to the first order flexural mode (F₁) already evidenced in Fig. 3.4, and the pronounced peak at 37 MHz corresponds to the vertical breathing mode (B_v) immediately visible in the time-dependent data. Complete mode assignment is obtained from the numerical simulation already described in Section 3.3.3. With fine adjustment of the trumpet's dimensions we are able to reproduce the spectrum within a maximum error of 7.5% in the exact frequency (vertical dotted lines in Fig. 3.6(b)). In particular, we find that an ellipticity in the base diameter of 20% accounts for the splitting observed in Fig. 3.4(b), in good agreement with earlier work [9]. Quite remarkably, we observe a pronounced amplitude for B_v despite the smaller phonon population associated with this high frequency mode ($u_{\text{th}} = 1.4 \times 10^{-13}$ m). This is the consequence of the large strain field associated with this specific mode. Quantitatively, this translates into a coupling $\lambda_{c,B_v}/2\pi = 3.6$ MHz, much larger than the values obtained for the mode F₁. The dissipation rate of B_v also significantly increases, reaching $\gamma_{m,B_v}/2\pi = 0.14$ MHz.

The measured noise spectrum may be translated into an equivalent displacement noise spectrum. For F₁, this results in a sensitivity to the displacement of the top facet of 2.6×10^{-13} m·Hz^{-1/2} ($\sqrt{S_{uu}} = 6.5 \times 10^{-14}$ m·Hz^{-1/2} for B_v). At present, this value is limited by charge noise in the device. For our system, this nevertheless represents reading displacement amplitudes equal to the zero-point fluctuations in just 70 s.

3.3.5 Quantum dot position determination

As a first application of the sensing capabilities of our device, we use the QD's sensitivity to the local strain to determine the exact location of the QD inside the photonic wire. This is a non-trivial task, important for the

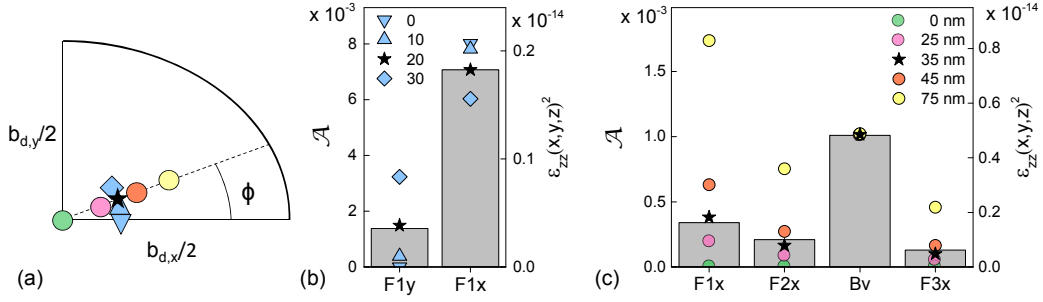


Figure 3.7 | (a) One quadrant of the QD plane (x and y correspond to the long and short axis of the ellipse, respectively). Coloured symbols correspond to various QD positions which result in the spectral signatures in (b) and (c). The black star corresponds to the position of QD1. (b) Gray bars, left axis: experimental data obtained in 3.3.2. Symbols, right axis: simulated strain along the z -axis for four different angles (in degrees) and a fixed distance ($r = 35$ nm) to the centre (a different distance results in a linear scaling of the right axis). (c) Comparison between results from 3.3.4 and simulated strain along the z -axis for various QD distances to the centre ($\phi = 20^\circ$).

coupling of two emitters via optical modes [94]. To do so, we use the thermal excitation of a series of modes. The idea is that each mode is driven equally by the thermal noise and produces a specific strain at a given location in the wire. By comparing the relative amplitude of the measured resonances, it is possible to extract the position of the QD inside the wire. We simulate the strain corresponding to a unit displacement of the top facet for a QD at a fixed distance of 110 nm from the base. In our case, the situation is simplified by the fact that we already know the precise location of the QD layer in the z -direction from the growth. We then compute the exact displacement associated with each mode, which corresponds here to the average displacement resulting from the Brownian motion at 4 K. From this proportionality factor, we obtain the strain corresponding to the Brownian motion. Table 3.1 shows the results for a QD located on the x -axis, at a 35 nm distance from the centre (black star in Fig. 3.7(a)). We observe that for all modes except T, the strain ϵ_{zz} in the vertical direction dominates over the other components. In fact we find that $\epsilon_{xx} \approx \epsilon_{yy} \approx -\nu_P \epsilon_{zz}$, where $\nu_P = 0.31$ is the Poisson ratio: to a good approximation, the QD experiences a uniaxial stress along the z -direction [87, 94]. This results in $\bar{S}_{NN} \propto \epsilon_{zz}^2$. To determine the QD's position, we first vary the in-plane angle ϕ for a fixed distance of the QD to the centre, and calculate the relative amplitude of the first order flexural modes (F_{1x} and F_{1y}). This is shown in Fig. 3.7(b) where we plot the results for four different values of ϕ and scale it to the experimental result. In a second step, we vary the radial position until we get good agreement with the amplitudes of the entire series of higher order modes, Fig. 3.7(c). This technique allows for an accurate positioning of the QD, modulo a sym-

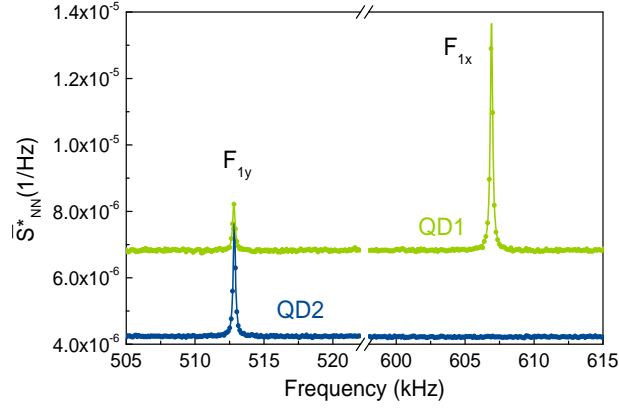


Figure 3.8 | QD noise spectrum for two different QDs. The shot noise has been subtracted: $\bar{S}_{NN}^* = \bar{S}_{NN} - \bar{S}_{NN}^{\text{shot}}$. QD1 corresponds to the QD studied in details. QD2 belongs to the same nanowire and its noise spectrum is recorded under similar conditions: $\Omega_R \simeq \gamma_{\text{sp}}$, $\Delta = \Gamma$, integration time of 20 mins.

metry versus the x and y axes (this experiment does not resolve positive and negative coordinates). We find that QD1 is located 35 nm away from the axis of the trumpet, with an angle $\phi = 20^\circ$ (black star in Fig. 3.7).

Some comments are in order. First, the assumption that the system is at bath temperature is tested *in-situ*: the quantum dot is an excellent thermometer and we observe, in particular, no laser-induced heating. Second, a related idea was introduced recently in Ref. [94]. In this work, the authors measure a shift in the QD energy as they drive the motion of the wire (addressing F_{1x} and F_{1y} successively). From the calibration of the induced displacement, and previous knowledge of QD response to strain, it is possible to determine the position of the QD. In the present situation, the use of a series of modes, all driven by thermal noise, allows for a more direct analysis with no need for an external calibration of the QD sensitivity to strain. (Note that B_v , in particular, produces a constant strain for all QDs in a given cross section plane of the wire and is very conveniently used as a reference point.) Furthermore, our technique requires in principle no previous knowledge of the location of the QD within the z -axis and could thus be used for a full 3D-mapping of the QD position.

3.3.6 Measurement on a second QD

In Fig. 3.8 we present results from the noise spectroscopy on a second QD in the same nanowire (QD2). Here we have removed the contribution from shot noise [88]. The different spectral signature is attributed to a different location of QD2 in the nanowire. In particular, the absence of a resonance at 607 kHz means that QD2 is located on the neutral (zero-strain) axis of

F_{1x} . We point out that amplitude of the peak is not a direct measurement of the relative coupling strength, since the QD linewidths may be different. In the present case, QD2 has a larger FWHM (not shown) which lowers its sensitivity. The reduced noise floor is associated to this lower sensitivity, possibly combined with a less noisy charge environment around QD2.

3.4 Discussion

A quantum emitter in a nanowire has potential for various quantum applications. On the one hand, dielectric nanowires are used as waveguides to realize high fidelity single photon sources in quantum optics [79, 80, 95, 96]. In this context, the strain coupling represents an additional dephasing channel with potential impact on the photon indistinguishability. Indeed, the coupling to mechanical modes introduces noise which leads to a broadening of the QD transitions for integration times longer than the mechanical oscillation period, i.e the coupling reduces the indistinguishability for photons separated by times larger than the oscillation period. The amplitude of the energy shift induced by the Brownian fluctuations of the nanowire is given by

$$\delta\Delta_{\text{th}} = \lambda_c \frac{u_{\text{th}}}{u_{\text{zpf}}}. \quad (3.8)$$

In the present situation, we find $\delta\Delta_{\text{th},F_{1x}}/2\pi = 0.15$ GHz and $\delta\Delta_{\text{th},B_v}/2\pi = 0.24$ GHz for F_{1x} and B_v respectively. For our device, this represents a slow ($\omega_m \ll \gamma_{\text{sp}}$) and negligible dephasing ($\delta\Delta_{\text{th}} \ll \Gamma_{\text{inh}}$). The values however compare with the minimum dephasing rate achievable (0.17 GHz), set by the spontaneous decay rate. We can also evaluate the expected QD frequency shift from the calculated strain. Neglecting confinement effects, this reads $\hbar\delta = g_a\epsilon_h + \frac{g_b}{2}\epsilon_{\text{sh}}$, where $\epsilon_h = \epsilon_{xx} + \epsilon_{yy} + \epsilon_{zz}$ and $\epsilon_{\text{sh}} = 2\epsilon_{zz} - \epsilon_{xx} - \epsilon_{yy}$ correspond to the hydrostatic and shear strains respectively, and g_a and g_b are material dependent deformation potentials [87]. Including the effect of both tensile and compressive strain, this results in a mechanically induced dephasing $\Delta_{\text{th}} = 2\delta$. (Note that in Eq. 3.8 this factor 2 is included in the definition of λ_c .) Assuming the QD is mainly composed of GaAs [97], $g_a = -8.33$ eV and $g_b = -2.0$ eV [87], we find $\Delta_{\text{th}}^{F_{1x}}/2\pi = 0.16$ GHz and $\Delta_{\text{th}}^{B_v}/2\pi = 0.20$ GHz, in excellent agreement with our results. More generally, we stress that such a coupling cannot be turned off and is present in the large majority of QD devices involving micro-fabrication, unless a specific engineering is used [98, 99] as we will demonstrate in Chapter 4. Recent results have shown that QDs in micropillars could be used for the generation of close to indistinguishable single photons with high collection efficiency [83, 84, 100]. Our simulations indicate that while the QD-mechanical coupling is strongly suppressed for flexural modes, the vertical breathing mode still leads to sizable

dephasing (few tens of MHz for a $2\mu\text{m}$ high pillar with $1.5\mu\text{m}$ diameter) on very short time scales (in this example the resonance frequency for B_v is 0.5 GHz). These results reveal the importance of considering the mechanical properties of any device designed for perfect single photon emission.

On the other hand, the large strain couplings suggest further applications using the nanowire as a quantum resonator. To this end, B_v stands out as a very interesting mode, with a cooperativity $\mathcal{C} = \lambda_c^2 / \gamma_{\text{sp}} \gamma_m = 0.6$. In the present experiment, the number of phonons in the mode is still high ($n_{\text{th}, B_v} \simeq 2200$). Cooling the system down to 20 mK would result in $n_{\text{th}} \simeq 11$, corresponding to a quantum cooperativity $\mathcal{C}_Q = \mathcal{C} / n_{\text{th}} = 0.06$. While this does not yet allow for coherent exchange between the QD and the mechanical resonator, the resonant excitation demonstrated here also opens the possibility of using the embedded QD to further cool the mechanical oscillator [13]. To that end, smaller structures with larger mechanical frequencies leading to the resolved side-band regime will facilitate operation. This does not represent a technological obstacle, meaning that such experiments are within reach. We emphasize that the present device could already be used to generate coherent mechanical vibrations from the QD excitation, as suggested by Auffèves and Richard in a recent proposal [12]. In this case, only the mechanical damping is important: the number of coherent phonons created through the optical driving of the two-level system depends on $(\lambda_c / \gamma_m)^2$. For both F_1 and B_v , $\lambda_c \gg \gamma_m$. For F_1 , applying this scheme to the present device, we predict a QD induced rms displacement as large as 80 pm while the thermal motion at 4 K represents an rms displacement of 12 pm.

Finally, we speculate that the Heisenberg limit in displacement sensitivity is achieved for an emitter driven close to, but below, saturation provided that the emitter has a transform limited linewidth and that the photons are collected and detected with perfect efficiency. Given the recent progress in QD micropillars [83], this limit is within experimental reach.

4 | Fiber-coupled QD

4.1 Introduction

As explored in Chapter 3, semiconductor QDs are attractive single photon sources: they are robust, compact and provide on-demand single photons at rates in the GHz range [101–103]. Their potential in the context of quantum optics however relies on the fulfillment of several demanding criteria [104]: high efficiency, high photon purity and simple operation. Recent progress has nevertheless brought QDs close to such applications. Single-photon operation has been obtained in a compact, table-top Stirling machine [105], offering a low-cost and user-friendly solution. Thanks to the increasing quality of the epitaxial material, spectrally pure emission has been demonstrated [90]. The last challenge that needs to be addressed is to efficiently couple the emitted light into a single mode fiber. Large progress in this direction has been made with the integration of QDs into micro and nano-scale photonic structures, such as cavities and waveguides, which allow the control of spontaneous emission [86, 106, 107]. In the last few years, important efforts to position the QD in an optimal way [80, 108] and to minimize the diffraction of light at the output of photonic nanowires [109] have pushed the collection efficiencies to values 75% while maintaining a Gaussian spatial profile [85, 110]. These impressive results require however the use of objective lenses with large numerical apertures. In parallel, different strategies to couple the emitted light directly into a single mode fiber have emerged [111–113]. In this Chapter, we report the direct coupling of QD single photons to an optical fiber with a new approach. Our device, the quantum fiber-pigtail, consists of a QD embedded in a PW, that is directly attached to the cleaved end of a single mode fiber. Thanks to the adiabatic expansion of the guided mode confined in the PW, we achieve an external collection efficiency of 5.8% at the output of the fiber-pigtail. The result represents a proof-of-principle for an easy-to-operate single photon source. We discuss realistic improvements and show that an efficiency exceeding 70% is within reach with current technology. Furthermore, easily addressable QDs at the end of a nanometer-scale tip have obvious potential as scanning probes. Possible applications include single

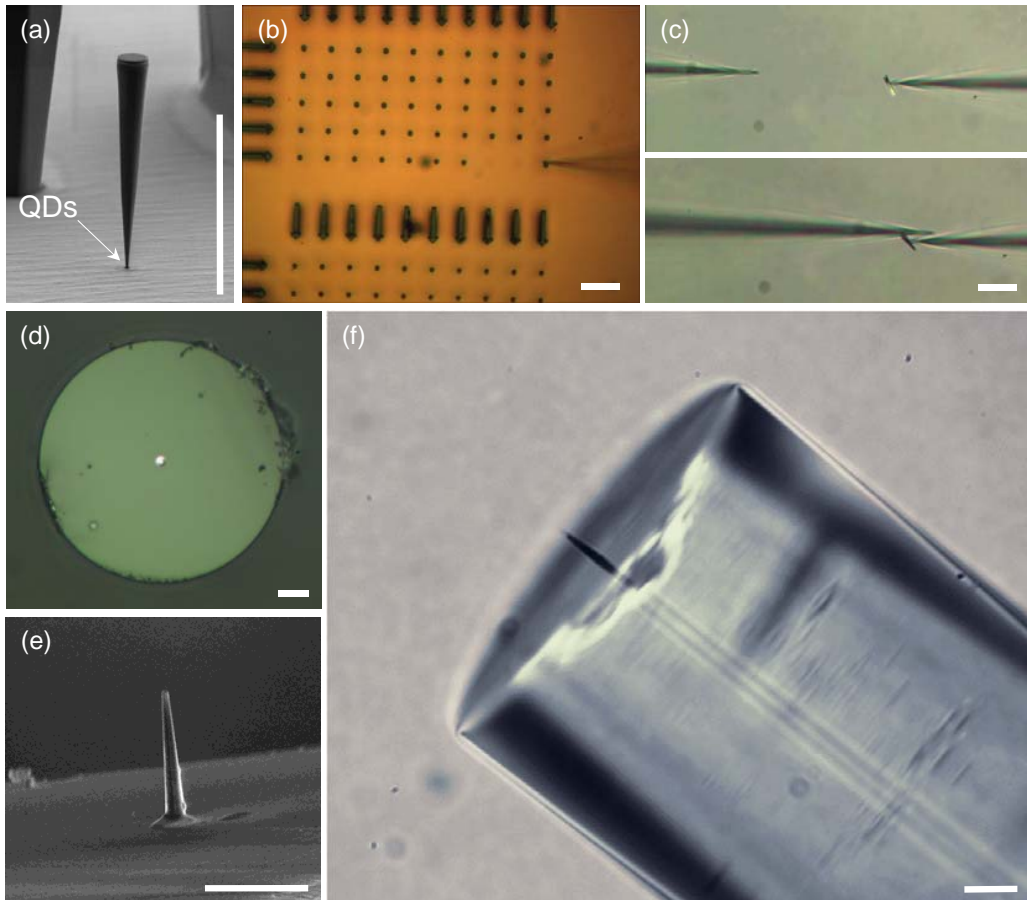


Figure 4.1 | (a) SEM picture of the photonic trumpet after etching and removal of the Ni mask. (b) Removing a single PW from its original substrate with glass micro-manipulator (right side). (c) Orientation of the PW for subsequent gluing onto the fiber. (d) Top view of the bare fiber with a drop of UV glue (bright spot) deposited at its center. (e) SEM picture of the fiber-wire connection. The drop of glue can be seen at the base of the PW. (f) Side view of the final device (optical microscope image). The white scale bars represent $10\mu\text{m}$.

photon near-field microscopy [114], deterministic quantum plasmonics [115] or electric field sensing [116]. We then proceed to show the proof-of-principle application of such an optical fiber-coupled semiconductor QD as a scanning electric field sensor. By tracking the induced energy shift on the peak of a single transition of a QD, we are able to map the vertical component of an external applied field. With the help of numerical simulations, we also investigate the unavoidable perturbation of the external field due to the dielectric nature of the probe, pointing toward geometric improvements to reduce this effect and increase the sensitivity of the device.

4.2 Fabrication

In order to realize a direct coupling between the photonic trumpet and a single mode fiber, we pick up an individual wire (described in Section 3.2) and glue it to the core of a standard fiber ($d_{\text{core}} = 4.4 \mu\text{m}$, $n_{\text{core}} = 1.4563$ and $n_{\text{cladding}} = 1.4513$), as illustrated in Fig. 4.1(a). Initially, we fabricate micro-manipulators by tapering a glass needle down to a few micron thickness. The micro-manipulator is then used to pick up one wire at a time thanks to a combination of electrostatic and Van der Waals forces (see Fig. 4.1(b)). Observations with a SEM indicate that the cleaving point lies at the interface between the PW and the substrate, within an estimated error of $\pm 10 \text{ nm}$ (the instrument's resolution). With a second micromanipulator we re-orient the PW into the appropriate direction (top facet facing downwards), Fig. 4.1(c). We then approach the cleaved facet of a fiber-pigtail, and deposit a drop of low fluorescence UV glue onto its core, Fig. 4.1(d). Finally, we bring the wire and the fiber into contact with an alignment precision on the order of $1 \mu\text{m}$ and illuminate with UV light to harden the glue. The resulting structure is shown in Figs. 4.1(e) and 4.1(f). It is robust and resistant to cycling to cryogenic temperatures (we performed up to 3 cycles with the same device without loss of signal), two important points for future applications. A link to a video of the process is available in Ref. [117].

4.3 Characterization

The device is tested at cryogenic temperature by plunging it directly into liquid He. The QDs are excited non-resonantly with a CW laser diode and the photoluminescence (PL) is analyzed with a spectrometer and a high efficiency Si-based CCD camera ($\eta_{\text{det}} = 27\%$ at $\lambda = 950 \text{ nm}$), see Fig. 4.2. A typical spectrum is shown in Fig. 4.3(a) for an excitation in the bulk ($\lambda_{\text{laser}} = 780 \text{ nm}$). We identify a peak associated to the GaAs nanowire and a series of sharp lines corresponding to several QDs. Importantly, we observe significant heating as we increase the non-resonant power. This is evidenced as a quadratic shift of the QD energies in Fig. 4.3(b), and indicates a poor heat dissipation in the device, despite the surrounding liquid He. A simple way to avoid this problem is to create electron-hole pairs directly in the InGaAs wetting layer connecting the QDs ($\lambda_{\text{laser}} = 830 \text{ nm}$). In this case, we minimize the amount of absorbed light and observe no heating effect over the range of useful excitation powers (see Fig. 4.3(b)). This second scenario was used for all the following measurements.

We focus on a PW featuring a diameter of 440 nm at the QD's position and $1.8 \mu\text{m}$ at the top facet. The wire sustains the guided modes associated

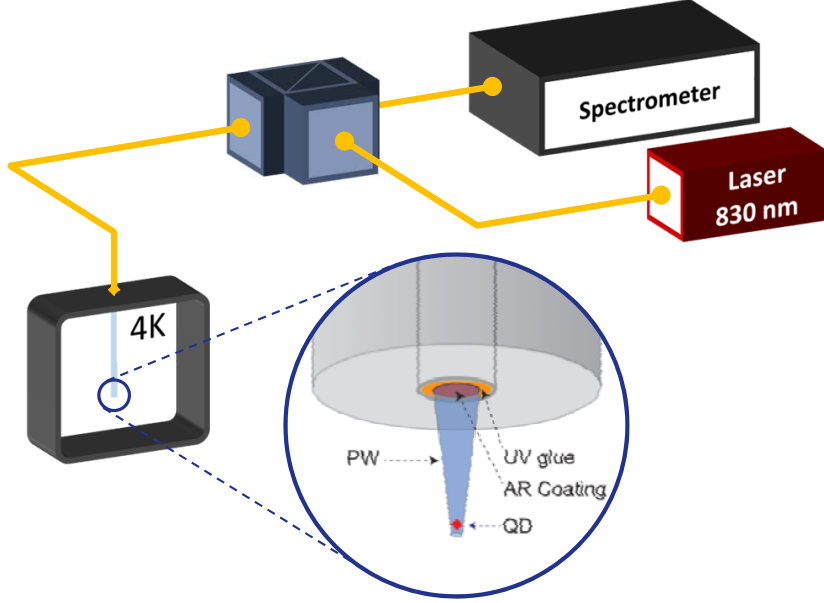


Figure 4.2 | The quantum fiber-pigtail is cooled down to 4 K in liquid He. The QDs are excited with a CW laser diode ($\lambda = 830$ nm / optionally 780 nm). The photoluminescence (PL) is analyzed with a spectrometer and a CCD camera (not shown).

with the first six orders and contains approximately 50 QDs distributed over a spectral bandwidth of about 50 nm. In the low energy tail, we identify in particular a bright complex labeled QD1, which consists of an excitonic transition X (possibly a charged exciton) and a red-shifted biexciton XX at high power (see Fig. 4.4(a)).

To confirm the quantum nature of the emitted signal, we perform an auto-correlation measurement on the exciton using a standard Hanbury-Brown Twiss experiment with a set of two avalanche photo-diodes. The result, shown in Fig. 4.4(b), reveals a pronounced dip at zero delay, characteristic of anti-bunched emission. The data are very well reproduced by the auto-correlation function of a perfect 2-level emitter with a lifetime of $1/\gamma_X = 1.2$ ns convoluted with the detector's response (Gaussian with full-width-half-maximum of ~ 400 ps).

To evaluate the extraction efficiency ϵ_e of our quantum fiber-pigtail, we record the PL intensity as we increase the excitation power. As we saturate the X transition, we observe a maximum count rate of ~ 40 kcts/s, Fig. 4.4(c). The data is fitted using a simple three-level model that takes the biexciton into account. Denoting γ_X and γ_{XX} the decay rates for the exciton and the biexciton, the detected PL intensity is given by [118]

$$I_{X,\text{det}}(P) = \frac{I_{\text{sat}}}{1 + \frac{\alpha_p P}{\gamma_X} + \frac{\gamma_{XX}}{\alpha_p P}}, \quad (4.1)$$

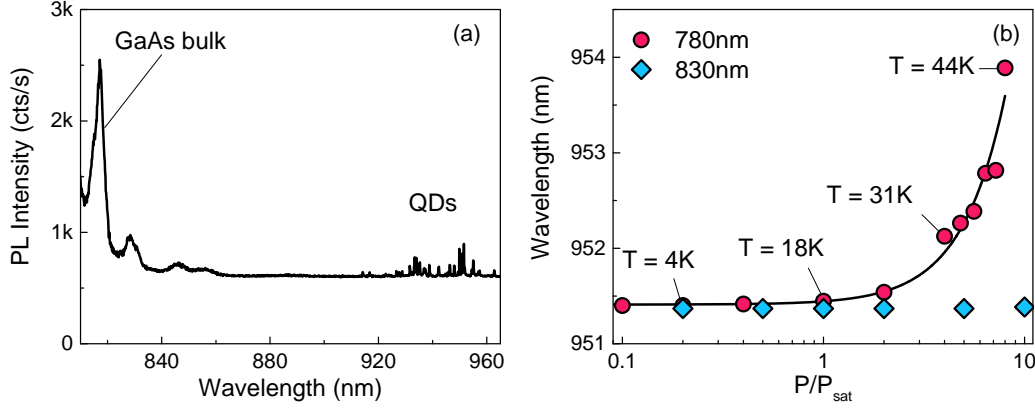


Figure 4.3 | (a) Typical PL spectrum for excitation in the GaAs bulk. (b) Power-induced heating of the PW for excitation in the GaAs bulk (red circles). Excitation in the wetting layer (blue diamonds) results in negligible heating. The abscissa has been normalized to the saturation power P_{sat} . The solid line is a quadratic fit to the data.

with I_{sat} the intensity at saturation, and α_p a coefficient which translates the measured excitation power into an effective pumping rate. Using $\gamma_X = 0.84$ GHz from the auto-correlation measurement and $\gamma_{XX} \sim 2\gamma_X$, we obtain very good agreement with our experimental data for $I_{\text{sat}} = 149$ kcts/s and $\alpha_p = 2.5 \times 10^{-3}$ GHz/ μ W. The relationship between the detected flux and the emission rate simply reads

$$I_{\text{sat}} = \epsilon_e \eta_t \eta_{\text{det}} \gamma_X, \quad (4.2)$$

where η_t corresponds to the overall transmission between the fiber-pigtail and the detector. Using a reference tunable laser diode set at 970 nm, we find $\eta_t = 6\% \pm 3.5\%$, which yields a collection efficiency $\epsilon_e = 5.8\% \pm 3.3\%$. The given value includes all losses, for instance the finite coupling of the QD to the waveguide-modes propagating in the upward direction, the imperfect wire-to-fiber mode matching and the transmission losses. This result can still be improved, but we stress that it is already more than one order of magnitude superior to the value one would obtain from QDs in the bulk. It therefore constitutes a proof-of-principle for our approach of integrating a quantum light source to a standard optical fiber.

We estimate the quality of the fabrication by evaluating the expected maximum efficiency at the output of the fiber-pigtail with numerical simulations. For this we evaluate the fraction of power radiated through the top facet for a dipole point source embedded in a PW using Lumerical FDTD Solutions. The result is multiplied by the overlap between the mode of the fiber and the profile of the electromagnetic field at the output of the PW. For a PW with the above-mentioned dimensions and a QD on axis, we find $\epsilon_e = 9.2 \pm 2.1\%$, where the error bar comes from the ± 10 nm uncertainty on

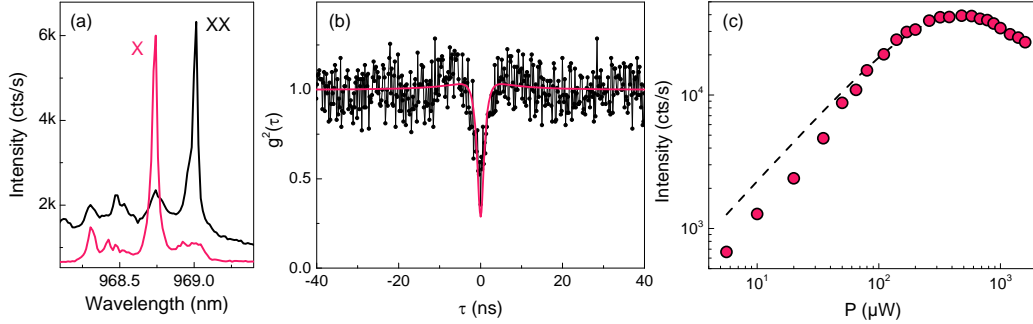


Figure 4.4 | (a) QD1 spectra at low ($P = 125 \mu\text{W}$, in red) and high ($P = 1.2 \text{ mW}$, in black) powers. X and XX correspond to the exciton and the biexciton. (b) Auto-correlation signal of X ($P = 64 \mu\text{W}$). The data are normalized to the average coincidence counts per time bin. The dip at zero delay is the signature of a single quantum emitter. The red solid line is a fit to the 2-level atom result including the detector time-jitter ($\sim 400 \text{ ps}$). (c) Power dependence of the exciton PL intensity. The dashed line is a fit using Eq. 4.1.

the distance between the QD and the cleaved facet. Our experimental result is in qualitative agreement with the theoretical prediction. This calculation shows that we have met the main challenges, namely positioning the QD close to the axis and aligning the center of the PW with the core of the fiber.

4.3.1 Discussion

We believe that the proposed device has the potential to relax some of the constraints associated with the use of single QDs in quantum optics experiment. Integrating it into a compact closed cycle cryostat would result in a quantum light source taking the form of a "black-box", with single photons directly available at the output of a standard single mode fiber. To be useful in a quantum optics context, a single photon source should be spectrally pure (usually a challenge for solid-state emitters) and present high collection efficiencies, typically higher than $\simeq 70\%$ for a quantum repeater protocol based on single photons [104]. Such a quantum pigtail is not out of reach. Recent experiments indicate that the coherence of photons emitted by QDs embedded in such photonic wires does not suffer from the presence of nearby etched surfaces. Though these experiments were not carried out on the highest quality material (bulk QD linewidth ~ 7 times the Fourier transform limit), the results are very encouraging. We shall now show that high efficiencies are reachable with realistic improvements.

To optimize ϵ_e , a natural strategy is to operate the tapered PW in the single mode regime. This choice simultaneously ensures high emission probabilities into the fundamental guided mode (HE_{11}) and optimum mode matching between the PW and the fiber. In a PW with a diameter $0.22 < D/\lambda < 0.31$,

more than 95% of the QD spontaneous emission is funneled into HE_{11} [86]. For such a symmetric waveguide, the emission is evenly distributed between the upward and downward directions. The fraction of photons emitted in the guided mode propagating towards the fiber can be increased up to $\beta_{\text{up}} \sim 72\%$ by exploiting the reflectivity associated with a simple cleaved facet [119]. This value can be further enhanced to $\beta_{\text{up}} \sim 92\%$ by depositing a metallic post mirror on the facet [119]. In both cases, the QD should be located at an anti-node of the electric field to benefit from constructive interference [119]. To optimize the mode matching between the PW and the fiber, the diameter of the PW's top-facet should be adjusted. We find a mode overlap $\mathcal{O} > 86\%$ when the top-facet diameter exceeds $7\mu\text{m}$. Importantly adiabatic conditions have to be maintained along the taper to minimize coupling to higher order modes propagating in the PW. As an example, we consider a $78\mu\text{m}$ long single mode PW with a tapering angle of 5° ensuring a transmission of the fundamental mode $\mathcal{T}_{\text{HE}_{11}} = 90\%$. The top facet has a diameter of $7\mu\text{m}$, and the cleaved apex is covered with a silver mirror [119]. With the active layer located 110 nm above the mirror, we obtain a total efficiency $\epsilon_{\text{th}} > 71\%$. Remarkably, the simple cleaved facet with no additional mirror already results in an efficiency of $\epsilon_{\text{th}} > 54\%$. To conclude, we stress that one may also tailor the properties of the fiber and relieve some constraints on the PW geometry.

4.3.2 Potential applications

The very nature of our device, with a ultra-sensitive element, such as a semiconductor QD, placed right at the tip of a nanowire, suggests applications in the field of scanning probe microscopy. Different applications are possible in this configuration: one possibility concerns quantum plasmonics. Surface plasmon polaritons (SPPs) represent a possible way of building integrated quantum optics circuits at the nanoscale. Our device could be used to transfer quantum information from the QD to propagative SPPs simply by bringing the sharp tip of our photonic wire into close proximity with a metallic nanostructure ($d < \lambda/2$). Compared to previous work, this solution presents more flexibility and would allow scanning of the sample surface or bringing the quantum emitter to a specific location, while controlling its exact distance to a given metallic antenna. The possibility of positioning our probe at will presents a significant advantage to explore the effect of the near-field environment on the emission properties of a QD. In particular, recent experiments have shown that control over the distance (as well as over the QD orientation) could lead to launching plasmons with probabilities approaching 50%. As we believe however that the present device is thus likely to find applications in the field of quantum plasmonics, in particular when more complex plasmonic circuits come to the fore. Another of the most straightforward applications

that comes to mind for our device is electric field sensing. In the next section, we will explore the potential of our device as a sensor for electric fields.

4.4 Electric Field sensing with QDs

Recently, there have been developments in electric field sensing with QDs as in 2015, Wagner et al. used a noncontact atomic force / scanning tunneling microscope (NC-AFM/STM) functionalized with a single molecule to image the dipole field of an ad-atom on a surface [46]. This first demonstration of scanning quantum dot microscopy (SQDM) registered single electron charging events of a molecular QD to produce three-dimensional images of the local electrostatic potential with sub-nanometer resolution. In transport experiments, gate-defined QDs have been employed as single charge detectors [120, 121] and self-assembled QDs have been employed as all-optical electrometers, demonstrating a sensitivity of $5 \text{ (V/m)}/\sqrt{\text{Hz}}$ [116]. These kind of QDs were also used to determine the position of single defect charges within 100 nm of a QD with a precision of 5 nm [122]. Electric fields in QDs produce large Stark shifts, which, due to a built-in electric dipole, are nearly linear around zero field. Nevertheless, a scanning electric field sensor based on an optically active semiconductor QD has not yet been realized. Such SQDM has the potential for a very large bandwidth, which unlike electronic and mechanically addressable sensors, is limited only by the spontaneous emission rate of the QD and could therefore approach the GHz range.

4.4.1 Setup

In order to investigate the performance of our probe as a sensor of electric field, we mount it in a low-temperature scanning probe microscope. The QDs at the end of the photonic wire are excited non-resonantly with a CW laser diode at 830 nm, which excites carriers directly in the wetting layer and avoids heating of the GaAs wire [98] as seen in Section 4.3. The PL from the QDs is guided into the fiber by the photonic wire and analyzed with a spectrometer equipped with a CCD camera. The fiber-coupled photonic tip is then positioned over one of two parallel Au electrodes, to which we apply the voltage V while the other is fixed to ground, as shown in Fig. 4.5(c). The tip-sample distance d is set to 10 nm from the gate surface with zero defined by the quenching of PL from the QD, most likely due to strain induced by contact. This distance as well as the lateral position of the tip are controlled by piezoelectric scanners without feedback to stabilize the position. The electrodes, shown schematically in Fig. 4.5(b) and (c), are deposited on a Si/SiO₂ substrate and are 80-nm-thick, 2- μm -wide, and 2- μm -apart from each other.

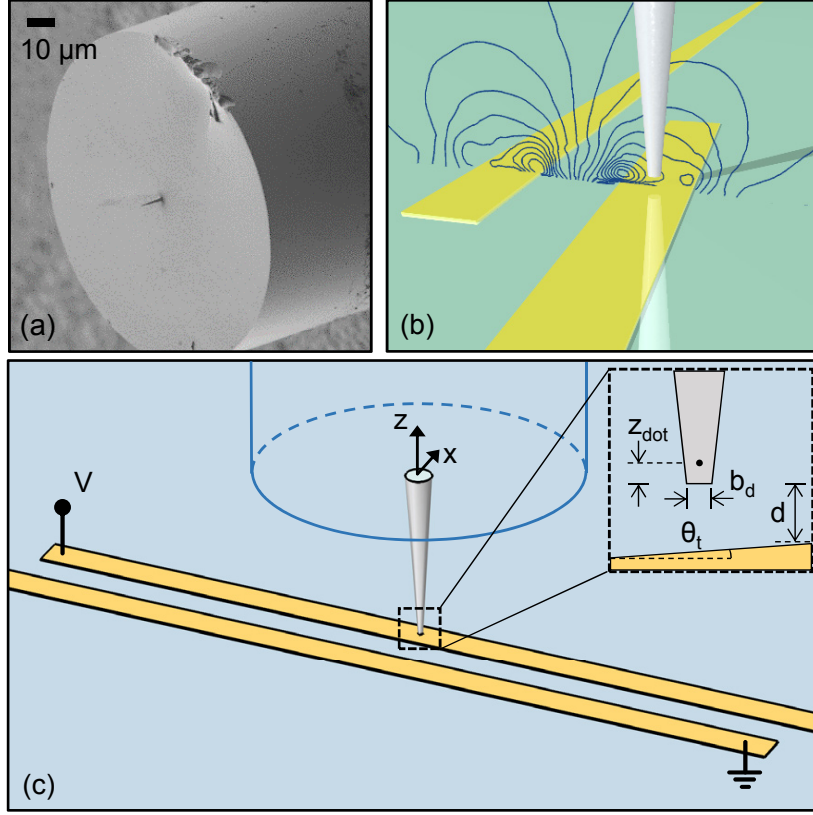


Figure 4.5 | (a) SEM of the fiber-coupled photonic wire. (b) Render of the tip with the simulated field produced by the electrodes in a planecut passing through the middle of the wire. (c) Schematic of the measurement setup. Inset: cross section of the xz -plane highlighting the relevant geometrical parameters: tip-sample distance d , bottom tip diameter b_d , distance of QD from the tip base z_{dot} , and sample tilt angle θ_t .

The resulting electric field tilts the energy bands of the semiconductor and, due to the quantum-confined Stark effect [123, 124], the transition energies of each QD are shifted to lower energy. Here we focus on a bright peak centered at 956.4 nm with a line-width of 100 μeV , which we attribute to an excitonic transition in a single QD. By sweeping the applied voltage V from -40 to $+40$ V we observe a shift in the energy of the emitted PL that is well-described by a quadratic function of the applied voltage, and therefore of the applied electric field, as shown in Fig. 4.6:

$$\xi_E = \xi_0 - p_{\parallel} E_{\parallel} + \beta_{\parallel} E_{\parallel}^2 + \beta_{\perp} E_{\perp}^2, \quad (4.3)$$

where ξ_0 is the unperturbed energy and p_{\parallel} is the static electric dipole of the QD exciton parallel to the wire axis. This axis coincides with the QD growth direction. Due to the in-plane symmetry of the QDs, there is no dipole term perpendicular to the axis [125, 126]. β_{\parallel} (β_{\perp}) and E_{\parallel} (E_{\perp}) are

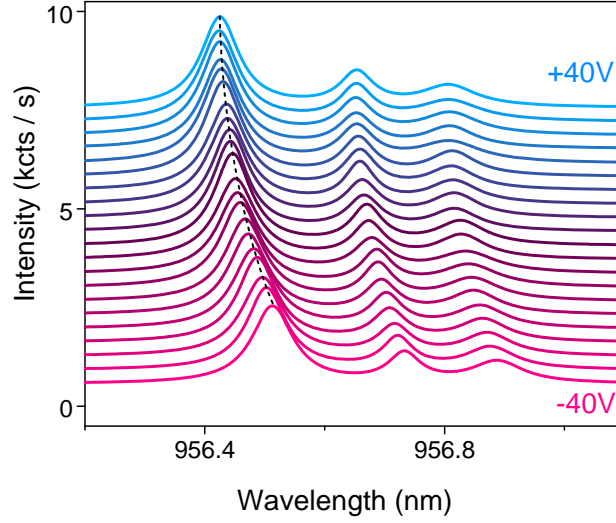


Figure 4.6 | Lorentzian fits of the investigated part of the PL spectrum showing excitonic lines associated with one QD for different values of V and $d = 10$ nm. The graphs are offset for clarity.

the polarizability of the QD exciton and the applied electric field, parallel (perpendicular) to the wire axis, respectively.

4.4.2 FEM Simulations

It is important to note that the presence of the photonic wire, due to its dielectric nature, reduces the field at the QD position and significantly perturbs the external applied field. In the simplest approximation, a thin dielectric cylinder with a uniform and unidirectional polarization strongly suppresses electric fields applied perpendicular to its long axis, while leaving parallel fields largely unchanged.

To better understand this effect we can consider the more simple case of a cylindrical dielectric wire in a uniform electric field. This will produce a depolarization field inside the wire. This effect is shown in Figure 4.7. Under the hypothesis of a uniform polarization of the dielectric parallel to the external field, the electric field at a point s along the long axis of the wire is reduced by a depolarization field anti-parallel to the external field. This reduction is substantially different for external fields parallel and perpendicular to the wire axis.

In order to calculate this effect, we define the angles $\psi_{1,2}(s)$ as shown in Fig 4.8 (a):

$$\cos(\psi_1) = \frac{s}{\sqrt{(b_d/2)^2 + s^2}}, \quad \cos(\psi_2) = \frac{L - s}{\sqrt{(D/2)^2 + (L - s)^2}} \quad (4.4)$$

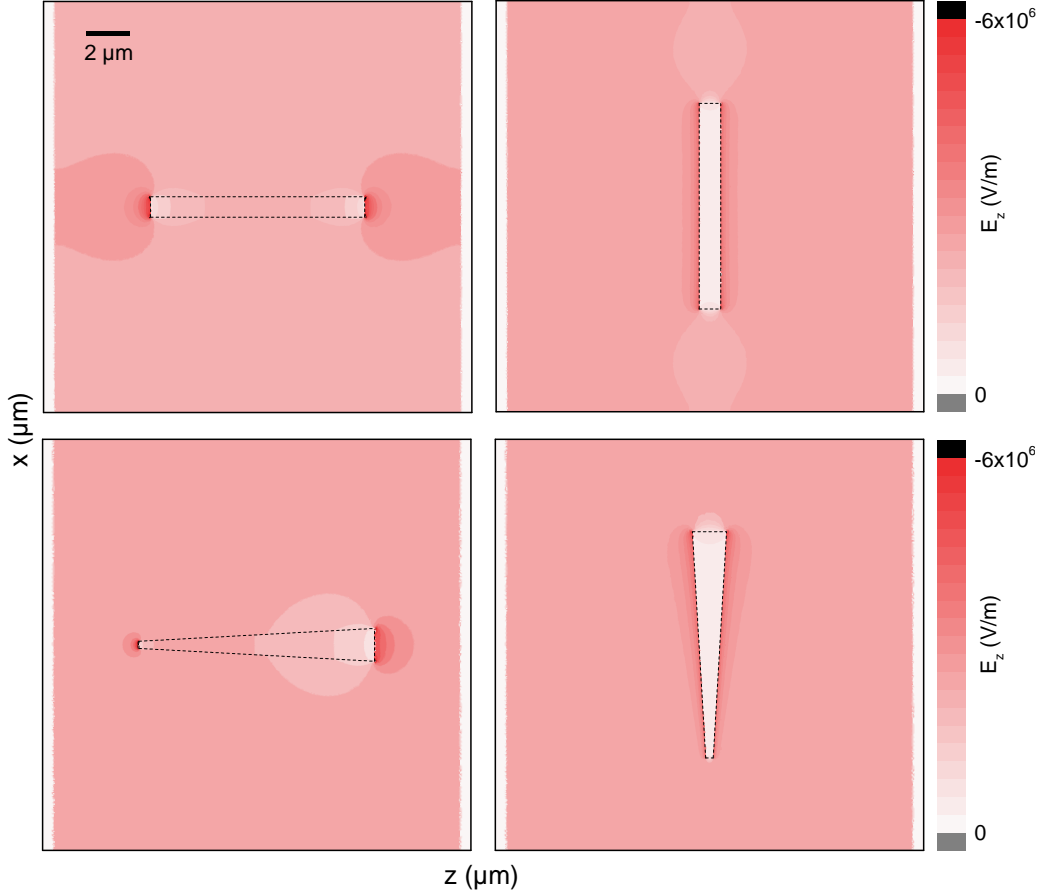


Figure 4.7 | Simulated values of E_z for a $11 \mu\text{m}$ long GaAs wire between two planar electrodes $20 \mu\text{m}$ apart. Plots show the xz -plane, which cuts through the center of the wire. A cylindrical wire with its axis (a) parallel and (b) perpendicular to the external field and a tapered wire with its axis (c) parallel and (d) perpendicular to the field.

where b_d and D are the diameter of the bottom and top facets, respectively. By integrating over the entire surface of the wire, we obtain a compact formula for the reduced electric field \mathbf{E} along the axis of the wire as a function of the position s along the axis (for more details see Appendix A):

$$\mathbf{E}(\psi_{1,2}) = \frac{1}{\chi(\psi_1, \psi_2)(\varepsilon_r - 1) + 1} \mathbf{E}_0 \quad (4.5)$$

where $\varepsilon_r = 12.9$ is the dielectric constant of the wire, $\chi(\psi_1, \psi_2) = \frac{1}{4}(\cos(\psi_1) + \cos(\psi_2)) \equiv \chi^\perp$ for the external field perpendicular to the axis of the cylinder and $\chi(\psi_1, \psi_2) = \sin^2\left(\frac{\psi_1}{2}\right) + \sin^2\left(\frac{\psi_2}{2}\right) \equiv \chi^\parallel$ for the field parallel to the axis.

In a real system, however, the hypothesis of the uniform and unidirectional polarization does not hold. As a result, the solution deviates from the analytical description of Equation 4.5. A finite element simulation (Com-

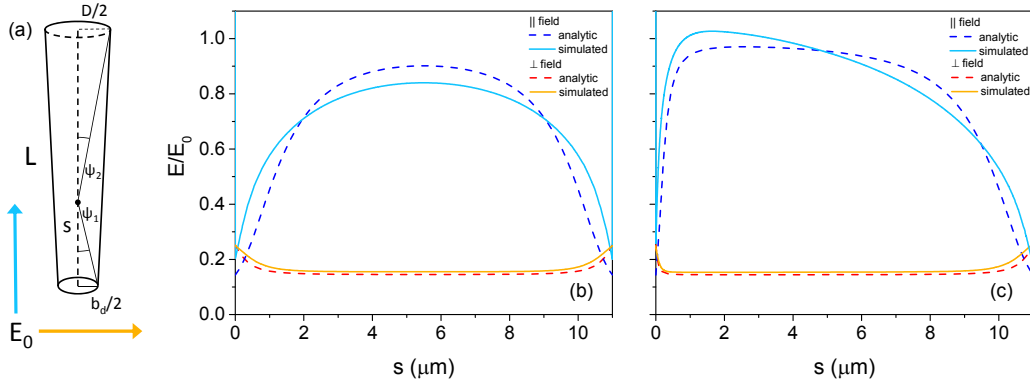


Figure 4.8 | (a) geometry of the wire and definition of the angles $\psi_{1,2}$. (b),(c) Normalized values of the electric field inside a cylindrical wire (b) with $L = 11 \mu\text{m}$ and $D = 1.5 \mu\text{m}$, and tapered wire (c) with $b_d = 250 \text{ nm}$, as a function of position along the axis of the wire. The solid lines correspond to exact simulations, while dashed lines are values given by Equation 4.5. Red and orange curves correspond to the perpendicular configuration and blue lines correspond to the parallel one.

sol) can produce a more realistic result without this simplifying assumption (Figure 4.8 (b) and (c)). The simulated (solid lines) and theoretical (dashed lines) values of the electric field inside a cylindrical and tapered wire are plotted as a function of s in the case of the external field parallel (blue) and perpendicular (orange and red) to the wire axis.

In the case of our experimental setup, however, the field is also not uniform along z . In a first approximation, the electric field inside the wire is obtained by just replacing the uniform field \mathbf{E}_0 in Eq. 4.5 with a space decaying form. A situation more similar to the one of our experimental configuration, with the field produced by two parallel electrodes, has been simulated and is shown in Fig. 4.9. Also in this scenario, it appears clear that the wire's narrow radial cross-section results in an efficient screening of E_{\perp} , while E_{\parallel} is less affected. At the QD position $z_{dot} = 110 \text{ nm}$ above the bottom facet, this directional screening effectively projects the unperturbed electric field along z . As we have seen, the magnitude of the effect depends on the diameter of the facets, the length of the wire, the position of the QD, and the direction of the field with respect to the long axis of the wire. In our experiment, the field at the dot position reaches values of 60% and 20% of the applied external field in the z and x direction, respectively.

4.4.3 2D mapping of local Electric Field

We then proceed to map the spatial dependence of the electric field produced by the gates by scanning the photonic wire tip and sweeping the applied voltage at every position. At this point, it is important to note that the

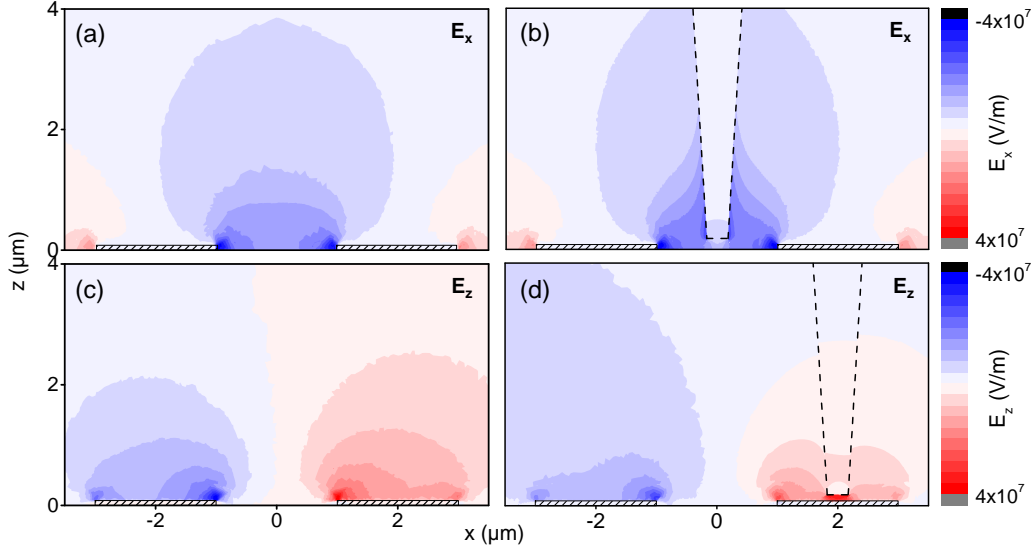


Figure 4.9 | Simulated maps of $\mathbf{E}(\mathbf{r})$ - The components (a) E_x and (c) E_z generated by the pair of electrodes. The left electrode is grounded and the right one is held at $V = 40$ V. (b) and (d) show the same electric field components in the presence of the dielectric tip. Note the pronounced screening of E_x by the photonic tip compared to that of E_z at the position of the QD near the apex of the probe.

electric field at the QD location \mathbf{r} is the sum of two distinct contributions $\mathbf{E}(\mathbf{r}, V) + \delta\mathbf{E}$, where the first term is due to the voltage applied across the electrodes and the second term is due to charges trapped in the vicinity of the QD. We can then write $\mathbf{E}(\mathbf{r}, V) = \boldsymbol{\alpha}_v(\mathbf{r}) \cdot V$, where $\boldsymbol{\alpha}_v(\mathbf{r})$ is a position dependent proportionality constant, which describes the spatial configuration of the electric field produced by the split-gates and the dielectric wire. This term is a single-valued function of \mathbf{r} and V . In contrast, $\delta\mathbf{E}$ is not a single-valued function of \mathbf{r} or V ; it describes a electric field that changes upon the stochastic reorganization of charges near the QD. These sudden, but infrequent rearrangements occur on time-scales on the order of a single voltage scan or longer and are often induced by the rapid changes in voltage or position occurring between scans.

In our geometry, $E_{\parallel} = E_z + \delta E_z$ and $E_{\perp} = \sqrt{(E_x + \delta E_x)^2 + (E_y + \delta E_y)^2}$. We scan above one electrode, where the electric field points nearly exclusively along z . Given the direction and the preferential penetration of the field in the z direction, we can assume E_x to be negligible in this region. E_y vanishes due to the symmetry of the electrode structure. As a result, Eq. 4.3 becomes:

$$\xi_E = \left[\xi_0 - p_{\parallel} \delta E_z + \beta_{\parallel} \delta E_z^2 + \beta_{\perp} (\delta E_x^2 + \delta E_y^2) \right] - \left[p_{\parallel} - 2\beta_{\parallel} \delta E_z \right] E_z + \beta_{\parallel} E_z^2. \quad (4.6)$$

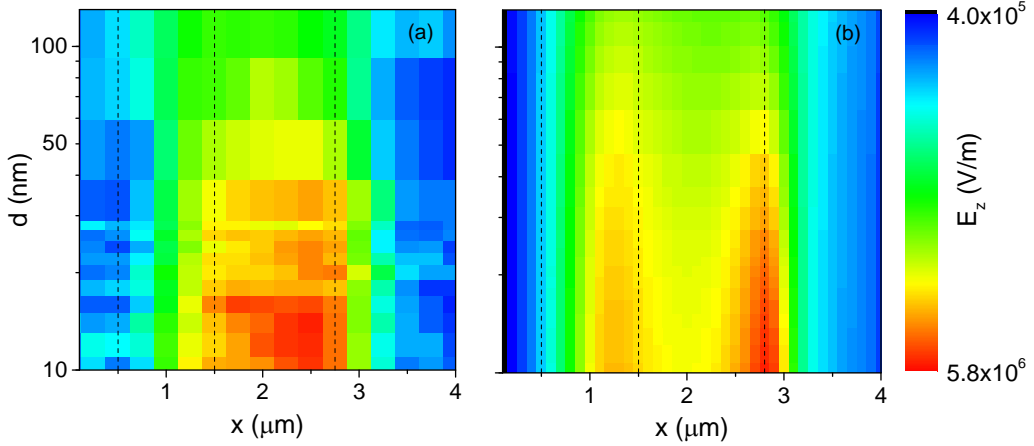


Figure 4.10 | Full maps of E_z as a function of x and d at $V = 40$ V extracted from (a) measurements and (b) simulations. Simulations consider a QD $z_{dot} = 110$ nm from the end of a photonic tip with $b_d = 350$ nm and a tilt angle $\theta_t = 5^\circ$. In (a), each point requires 21 seconds of measurement time; the full map in (a) requires 68 minutes.

Note that both the constant and linear terms in E_z (the first two terms in square brackets) depend on the electric field due to local charge reorganization. These terms are therefore subject to random and infrequent shifts. The quadratic term, on the other hand, depends only on the polarizability along the wire axis.

By collecting PL spectra, we measure the dependence of ξ_E on both voltage and position in the xz -plane. The measured QD exciton energies show a parabolic dependence on V with an offset $a_{f,0}$, a linear coefficient $a_{f,1}$, and a curvature $a_{f,2}$, each depending on position in the xz -plane, as seen in Fig. 4.11(a). As expected from the dependence of the constant and linear terms in Eq. 4.6 on components of the stochastic field $\delta\mathbf{E}$, $a_{f,0}$ and $a_{f,1}$ appear random and are observed to be hysteretic in both voltage and position. They are likely determined by the charging and discharging of defects within the photonic wire, which generate an extra electric field in the vicinity of the QD. On the other hand, $a_{f,2}$ remains constant as a function of voltage and reproducible as a function of position, following what is expected from Eq. 4.6: $a_{f,2}(x, z) = \beta_{\parallel} \alpha_{v,z}(x, z)^2$, where β_{\parallel} is a constant and $\alpha_{v,z}(x, z)$ is set by the configuration of the electrodes.

In order to make a detailed comparison to the experiment, we make a finite element simulation of $\alpha_{v,z}(x, z)$ at the position of the QD as the photonic wire is scanned above the electrode. A corresponding experimental map of this term can be extracted from the fits to the measured data, since $\alpha_{v,z}(x, z) = \sqrt{a_{f,2}(x, z)/\beta_{\parallel}}$. In Figs. 4.10 (a) and (b), we plot the measured and simulated $E_z(x, z)$, respectively, corresponding to an applied voltage of $V = 40$ V. In order to match the spatial dependence of our measurements

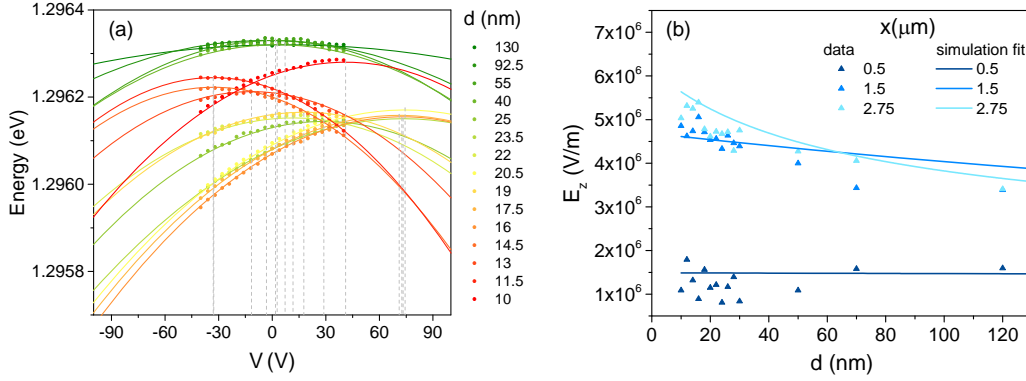


Figure 4.11 | (a) Energy of the leftmost QD emission peak in Fig. 4.6 versus the applied voltage V for different values of tip-electrode distance d . Solid lines are parabolic fits and gray dashed lines indicate the vertices of each parabola. The tip is positioned at the center of the electrode ($x = 2 \mu\text{m}$). (b) Triangles represent E_z as a function of d at $V = 40 \text{ V}$ extracted from the curvature fits for different x -positions (black dashed linecuts in 4.10); solid lines show corresponding simulated values of E_z .

to the simulations, we introduce a tilt angle $\theta_t = 5^\circ$, as shown in the inset of Figure 4.5(b). Such a misalignment between both scanning stages is experimentally reasonable and, in practice, difficult to avoid. A polarizability $\beta_{\parallel} = -0.012 \pm 0.005 \mu\text{eV}/(\text{kV}/\text{cm})^2$ brings the measured and simulated values of $E_z(x, z)$ into numerical agreement, as shown in Fig. 4.10 (a) and (b). Such a polarizability is an order of magnitude smaller than what is typically observed in literature for single exciton transitions in similar QDs under resonant excitation [127–129]. Under non-resonant excitation, as in this case, a variety of groups have observed reduced Stark shifts [130], likely due to the screening of electric fields by the clouds of electron-hole pairs generated around the QD.

The similarity of the measured and simulated maps of $E_z(x, z)$, demonstrates the successful implementation of our QD probe to spatially map the magnitude of a DC electric field along one direction. Nevertheless, the simulation does not capture all of the details of the measured map indicating that the experiment is still affected by charging effects not included in our model. Note that although we fit to full voltage sweeps at each position to extract the electric field configuration, one could reduce noise and speed up the measurement by applying a small AC voltage to the gate and recording the QD's response. Energy shifts at f and $2f$, where f is the frequency of the applied field, would correspond to the linear contribution, arising from the electric dipole of the QD, and to the quadratic contribution, arising from the polarizability, respectively [73]. Similarly, static electric fields generated by arbitrary samples without electrodes could be mapped by dithering the position of the QD sensor at frequency f and measuring the corresponding

response. As a result, one could measure the spatial derivative of E_z along the direction of the dither. In this way, the technique could be generally applied to a variety of samples producing electric fields, including by charge defects on surfaces.

4.4.4 Optimal wire geometry for sensing

One important observation that can be made from Fig. 4.10 (a) and (b) is the rapid decrease in measured electric field as a function of tip-electrode distance d compared to that expected in vacuum. As shown in Fig. 4.12 (a), this effect is a direct consequence of the polarization charge induced on the bottom facet of the photonic wire, which screens the out-of-plane electric field impinging on the QD. Note that this effect must be considered for any electric field sensor based on a dielectric scanning probe. In order to reduce the screening effect for E_z , which decreases the sensitivity of the sensor and distorts the observed field with respect to the unperturbed case, this surface charge density must be minimized. If we exclude replacing the GaAs tip material with one having a dielectric constant closer to the one of the vacuum, the reduction of this screening charge can be achieved by reducing the diameter b_d of the bottom facet. This sharpening of the scanning probe, would also help to increase the screening of E_x , making the QD Stark shift an even closer measure of E_z^2 . In practice, however, b_d is constrained to values higher than 190 nm in order to maintain optimal guiding of the QD PL up the photonic wire and into the optical fiber [119]. The choice of b_d in turn sets a natural minimum tip-sample distance d of the same order, below which both the spatial resolution will not improve and the tip will strongly perturb the local electric field. Once b_d and d are fixed, finite element calculations show that there exists an optimal position for the QD above the bottom facet z_{opt} , as shown by Fig. 4.12(b). This position minimizes the screening effect and hosts the largest measurable field from the electrodes within the tip. The black diamond in Fig. 4.12(b) indicates the position of the QD within the device used in our experiments. For $d = 100$ nm, optimization of b_d and of the position of the QD could result in the ability to measure much weaker fields parallel to the wire axis with almost no tip-induced perturbation of this component. Note that in order to ensure maximum reflection in the upward direction, z_{dot} should be a multiple of $\lambda/2n_r$ from the bottom facet, where λ is the wavelength of the emitted light and n_r the effective index of the fundamental guided mode for a diameter b_d . In general, there is a natural trade off between a scanning probe tip which minimally perturbs the electric field and one that optimally guides the sensor emission.

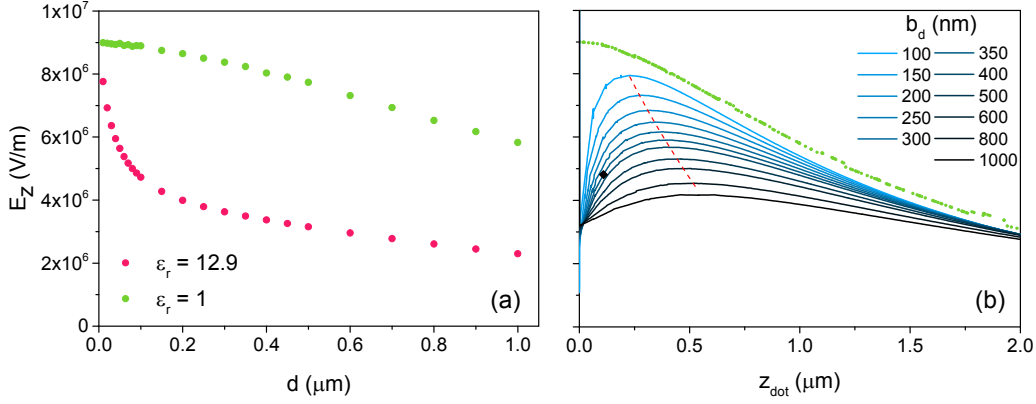


Figure 4.12 | (a) Simulated E_z at $z_{dot} = 110$ nm is plotted in pink as a function of tip-electrode distance d in a GaAs tip with $b_d = 350$ nm. The corresponding condition without screening is plotted in green. (b) E_z values along a z line-cut with the photonic tip at $d = 0.1$ μm for different values of the bottom diameter b_d . We define z_{opt} as the position where E_z is maximum inside the tip. The values of z_{opt} are fitted by the red dashed line for different values of b_d . The black diamond indicates the QD position in our current device, while the green dots are values of E_z in the absence of the trumpet, as a reference.

4.4.5 Discussion

Given a measured polarizability $\beta_{\parallel} = -0.012 \mu\text{eV}/(\text{kV}/\text{cm})^2$, typical count rate of 2.3 kHz, and emission linewidth of 98 μeV , the measurements demonstrate a sensitivity of $1.4 \times 10^6 (\text{V}/\text{m})/\sqrt{\text{Hz}}$. Although such a sensitivity is sufficient to demonstrate the feasibility of electric field microscopy with our fiber-coupled QD sensor, it must be improved in order to approach the performance demonstrated by scanning SETs.

Measuring by resonance fluorescence constitutes a first step: the absence of non-resonant excitation should reduce charge noise near the QD [90], allowing the use of the linear Stark effect. Assuming measured values for the count rate, emission linewidth, and a dipole moment $p_{\parallel}/e = 0.03$ nm, a linear measurement would already yield a sensitivity of $5.6 \times 10^4 (\text{V}/\text{m})/\sqrt{\text{Hz}}$. This worst-case estimate does not consider that measuring by resonance fluorescence would also eliminate screening of the sensor QD by photo-excited electron-hole pairs and decrease the QD emission linewidth. Furthermore, by optimizing the geometry of the photonic wire tip and the position of the QD, higher optical collection efficiencies, resulting in higher count rates, could be combined with better electric field penetration. These additional improvements would lead to reduced distortion of the unperturbed electric fields and higher sensitivity. If charge noise near the sensor could be reduced to levels achieved by QDs buried in bulk semiconductor material, a linear Stark effect measurement could then approach $20 (\text{V}/\text{m})/\sqrt{\text{Hz}}$, assuming $p_{\parallel}/e = 0.3$

nm [116, 122]. This estimate is based on a count rate of 1 MHz and an emission linewidth of $5 \mu\text{eV}$, which were observed in shot-noise-limited resonance fluorescence measurements carried out in photonic-trumpet QDs similar to those measured here [131]. Given that the bandwidth of this type of SQDM is determined by the efficiency of the luminescence collection and limited by the QD's spontaneous emission rate, it could approach the GHz range. These characteristics, combined with a spatial resolution roughly set by the bottom diameter of the tip, are promising for mapping of single charges on surfaces, measuring individual tunneling events, and monitoring charging dynamics in few electron and mesoscopic systems.

5 | Conclusion and Outlook

In this thesis we explored some of the aspects that make NWs very promising for sensing, focusing mainly in Scanning Probe Microscopy applications. NWs have drawn growing interest in the last years due to the incredible versatility and consequent variety of suitable applications. Due to favorable geometry and low mass, NWs present themselves as excellent force transducers. Their almost perfect structure free of defects significantly increases the quality of mechanical resonators based on them. The possibility to control geometrical parameters like diameter and length makes it possible to move the resonance frequency of these objects to higher frequencies so it is easier to decouple them from noise. However, such slender beams are more susceptible to enter non-linear regimes of motion, where the analysis becomes more complex but sometimes difficult to avoid.

For this reason, we studied the nonlinear regime of motion of GaAs NWs. Our results indicate that although nonlinear motion can be non-negligible for NWs, the nonlinearity can also be turned into an advantage using simple measurement schemes. We have then seen how the fundamental mode of our NWs is always split in two orthogonal modes due to a small asymmetry in the cross section and we studied how these modes interact through a non-linear coupling. When driving one mode to high enough amplitudes its displacement affects the motion of the other mode shifting its frequency. This mode coupling was clearly visible in a ringdown measurement and different pump-probe experiments. Such mode coupling could have several applications, including tuning the resonance frequency [29] and quality factor [30] of one mode through driving of the other mode, and implementing quantum non-demolition measurements of mechanical excitation [132]. Another prospective use of the two orthogonal modes in the nanowires lies in bidimensional sensing. We then proceeded to demonstrate how the two modes of the NW in a pendulum geometry could be detected simultaneously giving access to a bidimensional AFM setup when we scan a sample close to the tip of the wire. Moreover, by exploiting the nonlinear regime of motion in each mode, a force sensitivity of ~ 100 zN/ $\sqrt{\text{Hz}}$ [63] could in principle be reached in both orthogonal directions simultaneously. Such a bidimensional sensor has been used before to measure the non-conservative nature of radiation

pressure [28]. Mode coupling could additionally lead to coherent dynamics, where energy can be exchanged between the two modes similarly as it could be done in quantum two-level systems. As a consequence, reaching strong coupling between the modes could allow to reduce frequency fluctuations of the resonators through dynamical decoupling, eventually reaching the thermal limit.

Nonetheless, we are not limited to bidimensional surface interactions: the versatility in the growth of NWs, that can be grown with different structures and materials, opens the gate to a vast range of possible probes suitable to different environments. Functionalization of the NW tip gives access to sensibility to other types of forces. Semiconductor NWs with magnetic tips can then be used as probes for magnetic samples while maintaining a relatively simple and all-optical readout. Stray fields from particular magnetic configurations can interact with the magnetic tip, affecting the detected motion of the wire. We believe that NWs heterostructures offer great tools for sensing. As an example, it has been shown that when subjected to pulsed excitation, III-V core-shell semiconductor NWs, exhibit lasing up to room temperature [133]. While keeping the same NW scanning setup as used in Section 2.6, it would be possible to excite and detect light emitted from the wire. When close to threshold, due to the nonlinearity of the lasing process, these NWs could be used to sense a small change in the dielectric environment close to the wire.

As discussed in Chapter 3, NWs can also be host of quantum objects such as QDs. Semiconductor NWs make excellent waveguiding platforms. As a consequence, an optically active QD embedded in a tailored GaAs NW results in a high fidelity single photon source. Moreover, the QD emission results intrinsically coupled to the nanoresonator through strain, creating effectively a monolithic hybrid system with potential for various quantum applications. By exploiting this coupling, we read the resonance fluorescence signal of the QD to detect sub-picometer displacements of the mechanical modes at cryogenic temperature by measuring the fluctuations in the single photon count rate, an amelioration in position sensitivity by four orders of magnitude compared to previous results [8,9]. As an application of the sensing capabilities of our device, we used the thermal excitation of a series of mechanical modes to determine the location of the QD within the nanowire. Finally we discussed the impact of the strain coupling on the coherence of the single photon emitter, introducing extra noise and dephasing in the QD emission, and, as a consequence, reduces the indistinguishability of the photons.

To this end, we developed a new device, a quantum-fiber pigtail, where we directly couple a QD to an optical fiber eliminating the need for complex optical setup and at the same time reducing the strain coupling that leads

to dephasing of the QD emission. The prototype of our device resulted to be a robust and compact single photon source but with relative low collection efficiency. In this direction, with the support of numerical simulations, we demonstrated how the efficiency of our device can be increased by one order of magnitude with no subversive changes of the wire. Photonic wires with geometries closer to what we found to be the optimal values have been already developed [134]. This, in combination with suspended photonic trumpets [99], allowing to control better the distance of the QD to the tip of the wire, could greatly improve the performance of our device with minimal effort. Last, due to the favorable geometry of our device, we demonstrated how it can be implemented as sensor for local electric fields. As a first proof-of-principle, we map the vertical component of the electric field produced by two parallel gold electrodes. As the PW was not originally designed for scanning applications and direct coupling to an optical fiber, the sensitivity of our device has not reached our initial expectations. This device, however, has proven to be an excellent starting point for sensing electric fields. The first step in optimization corresponds in re-designing our tip for our specific purpose. With the help of FEM simulations we found the optimal geometry for the optimal scanning PW. While it is true that the dielectric nature of our probe reduces the effective field at the QD position, the major limitation for our devices resulted to be charge noise inside the wire, close to the QD. Implementation of a resonance fluorescence setup as well as the passivation of the surface of the PW will most likely be the major advancement in this technique in the near future. Avoiding rearrangements of charges could make the approach to a surface more reliable and simplify the analysis while at the same time improving the sensitivity of our device.

As a last remark, we note how the geometry of our device results extremely favorable for any sensor based on optical readout combining scanning tip and optical collection into one monolithic fiber-coupled object. This provides efficient and easy optical coupling as well as a convenient scanning geometry and can be adopted to any optically addressable quantum sensor (molecules, Nitrogen-Vacancy (NV) centers in diamond, etc.). The axial access for excitation and detection of the optical element grants no limitation of access to scan sample regions, with the only disadvantage of shining light directly on the sample. While a perpendicular detection setup like the one used in Section 2.6 is definitely possible, it presents few disadvantages when trying to detect an optical active object close to the tip of a probe. First, the NW itself acts as a waveguide along the axial direction (already reducing emitted light perpendicular to it) and, in addition, the investigated sample would produce a shadowing effect, reducing the collected light and limiting the accessibility of the sensor to areas only close to the edge of the sample. This is true not only for QDs in NWs but it is something to keep in

consideration for any scanning setup based on optical readout.

A | Appendix A

A.1 Dielectric wire in uniform field

Here we show the procedure leading to Eq.4.5 where we calculate the value of the electric field along the axis of a dielectric wire in a uniform electric field \mathbf{E}_0 . We can distinguish the two main particular cases where the external field is directed parallel or perpendicular to the axis of the wire. In both cases we consider the following hypothesis: the polarization of the wire is uniform and there are no charges inside the wire. We start for simplicity considering a cylindrical wire aligned along z .

A.1.1 $E_0 \perp z$

If we assume the external field \mathbf{E}_0 directed along the positive x axis, this field will produce a polarization \mathbf{P} in the wire also parallel to the x axis. We will then proceed to calculate the field $E_d(z)$ produced by this polarization on the axis of the wire. In this case the field along the axis is gonna be produced entirely by the surface charges on the cylinder wall while no contribution will be given by the top and bottom facets as they lie parallel to the field. With reference to Fig.A.1, we can write the expression for surface charge σ at a point C on the wall of the cylinder as:

$$\sigma(C) = P \cos \theta_c, \quad (\text{A.1})$$

where P is the polarization of the cylinder (directed along x). The electric field along the axis of the wire is then given by:

$$E_d^\perp(z) = 2 \int_{-\pi/2}^{\pi/2} \int_{-s_1}^{s_2} \delta \mathbf{E}(C) \cdot \mathbf{e}_x dz d\theta, \quad (\text{A.2})$$

where we considered twice the contribution of the semi-surface due to symmetry and $\delta \mathbf{E}(C)$ is the field generated by an infinitesimal surface dS centered in C that can be written as:

$$\delta \mathbf{E}(C) = \frac{1}{4\pi\epsilon_0} \frac{\sigma(C)dS \mathbf{CO}}{OC^2} \frac{\mathbf{CO}}{OC}, \quad (\text{A.3})$$

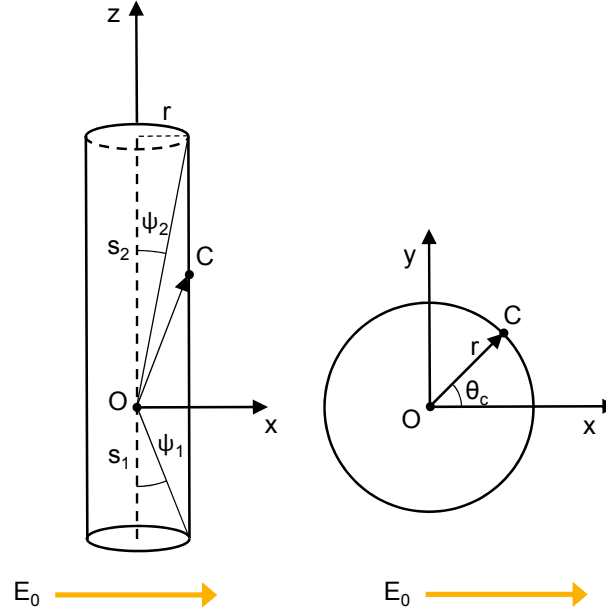


Figure A.1 | Side and top view of a cylindrical dielectric wire in a uniform electric field aligned along x

where $dS = r d\theta dz$ and $OC = \sqrt{r^2 + z^2}$. Since $\mathbf{OC} = r \cos \theta \mathbf{e}_x + r \sin \theta \mathbf{e}_y + z \mathbf{e}_z$ then $\mathbf{OC} \cdot \mathbf{e}_x = r \cos \theta$, substituting in Eq.A.3 we obtain:

$$\delta \mathbf{E}(C) \cdot \mathbf{e}_x = -\frac{1}{4\pi\epsilon_0} \frac{P \cos \theta r d\theta dz}{r^2 + z^2} \frac{r \cos \theta}{\sqrt{r^2 + z^2}}. \quad (\text{A.4})$$

Eq.A.2 then becomes:

$$E_d^\perp(z) = -\frac{2P}{4\pi\epsilon_0} \int_{-\pi/2}^{\pi/2} \cos^2 \theta d\theta \int_{-s_1}^{s_2} \frac{r^2}{(r^2 + z^2)^{3/2}} dz. \quad (\text{A.5})$$

By solving the integrals and defining the angles ψ_1 and ψ_2 so that:

$$\cos(\psi_1) = \frac{s_1}{\sqrt{r^2 + s_1^2}}, \quad \cos(\psi_2) = \frac{s_2}{\sqrt{r^2 + s_2^2}}, \quad (\text{A.6})$$

we obtain:

$$E_d^\perp(z) = -\frac{P}{4\epsilon_0} (\cos \psi_1 + \cos \psi_2). \quad (\text{A.7})$$

A.1.2 $E_0 \parallel z$

In the case where the external field is parallel to the axis of the wire, the polarization is aligned entirely along z and, in particular, we have $\sigma_{\text{sup}} = P$ on the top facet and $\sigma_{\text{inf}} = -P$ on the bottom facet. In an analog way to the

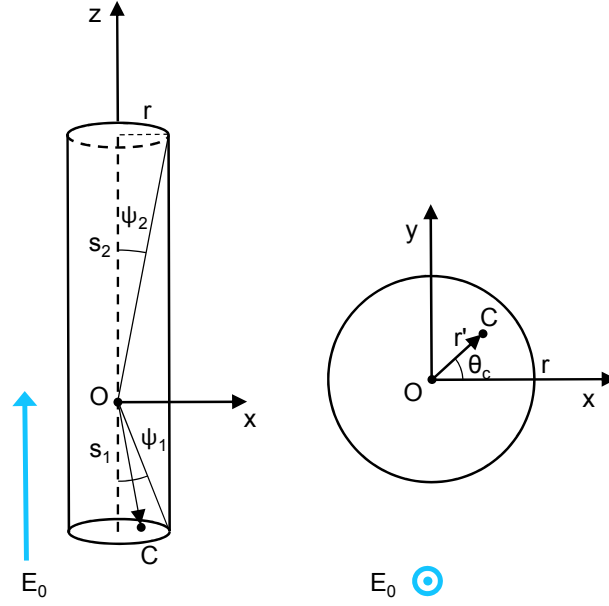


Figure A.2 | Side and top view of a cylindrical dielectric wire in a uniform electric field aligned along z

previous case, we can calculate the field along the axis of the wire produced by charges on the surface (in this case only the top and bottom facet contribute). For the symmetry of the problem we start considering only the bottom facet. For an infinitesimal surface dS centered in C we can write:

$$E_{d,\text{inf}}^{\parallel}(z) = 2 \int_0^{2\pi} \int_0^r \delta\mathbf{E}(C) \cdot \mathbf{e}_z dr' d\theta. \quad (\text{A.8})$$

Similar to before, we use Eq.A.3, but in this case we have: $\sigma_{\text{inf}} = -P$, $dS = r' d\theta dr'$, $OC = \sqrt{s_1^2 + r'^2}$, and $\mathbf{OC} = r' \cos \theta \mathbf{e}_x + r' \sin \theta \mathbf{e}_y - s_1 \mathbf{e}_z$ so that $\mathbf{OC} \cdot \mathbf{e}_z = -s_1$. We can then write:

$$\delta\mathbf{E}(C) \cdot \mathbf{e}_z = -\frac{1}{4\pi\epsilon_0} \frac{Pr' d\theta dr'}{r'^2 + s_1^2} \frac{s_1}{\sqrt{s_1^2 + r'^2}}. \quad (\text{A.9})$$

Substituting Eq.A.9 into Eq.A.8 we obtain:

$$E_{d,\text{inf}}^{\parallel}(z) = -\frac{P}{4\pi\epsilon_0} \int_0^{2\pi} d\theta \int_0^r \frac{s_1 r'}{(s_1^2 + r'^2)^{3/2}} dr'. \quad (\text{A.10})$$

By recalling the definition for ψ_1 given by A.6, we can write:

$$E_{d,\text{inf}}^{\parallel}(z) = -\frac{P}{2\epsilon_0} (1 - \cos \psi_1). \quad (\text{A.11})$$

By symmetry we can write the expression for the field on the axis generated by the top facet as:

$$E_{d,\text{sup}}^{\parallel}(z) = -\frac{P}{2\varepsilon_0} (1 - \cos \psi_2). \quad (\text{A.12})$$

Summing the contribution of the two facets and remembering that:

$$\sin^2 \psi = \frac{1 - \cos(2\psi)}{2}, \quad (\text{A.13})$$

the overall field on the axis is given by:

$$E_d^{\parallel}(z) = -\frac{P}{\varepsilon_0} \left(\sin^2 \left(\frac{\psi_1}{2} \right) + \sin^2 \left(\frac{\psi_2}{2} \right) \right). \quad (\text{A.14})$$

A.2 General case

We can now take into account the total field on the axis of the wire by writing $\varepsilon_r \varepsilon_0 \mathbf{E} = \varepsilon_0 \mathbf{E} + \mathbf{P}$ where $\mathbf{E} = \mathbf{E}_0 + \mathbf{E}_d$ is now the total field at a point along the axis. By expressing $\mathbf{E}_d = -\chi \frac{\mathbf{P}}{\varepsilon_0}$, from Eq.A.7 and A.14 we can write:

$$\mathbf{E} = \frac{1}{\chi(\varepsilon_r - 1) + 1} \mathbf{E}_0, \quad (\text{A.15})$$

where we defined χ for the perpendicular and parallel geometry respectively as:

$$\chi^{\perp} = \frac{1}{4} (\cos \psi_1 + \cos \psi_2), \quad \chi^{\parallel} = (\sin^2 (\psi_1/2) + \sin^2 (\psi_2/2)) \quad (\text{A.16})$$

We can now extend the treatment to a tapered wire of length L , top diameter D and bottom diameter b_d by just using the definition for $\psi_{1,2}$ as in Eq.4.4 where we substituted $s_1 = s$ and $s_2 = L - s$ and r has been replaced by $b_d/2$ and $D/2$ for ψ_1 and ψ_2 respectively.

B | Appendix B

B.1 6 axis scanning NWs Microscope

Images of the microscope used in Chapter 2. The design realized in Solid-works is shown on the left and pictures of the actual microscope are shown on the right.

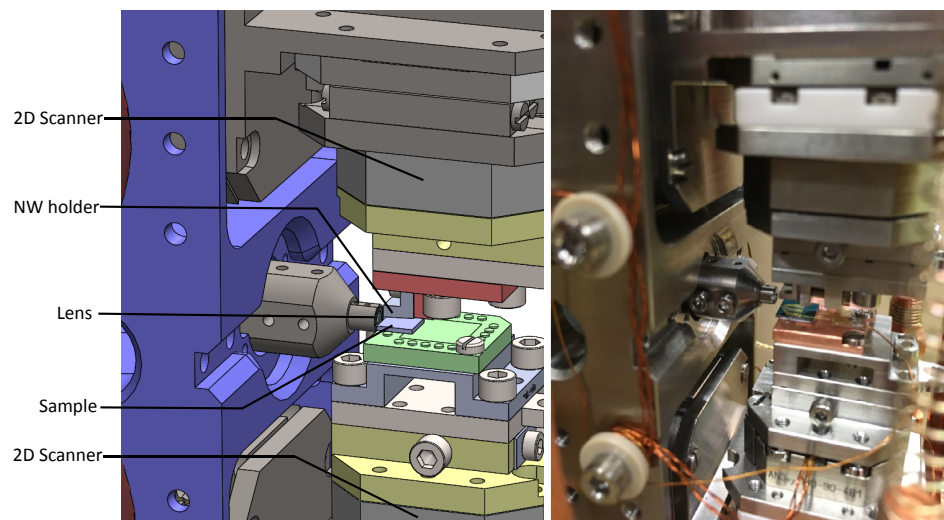


Figure B.1

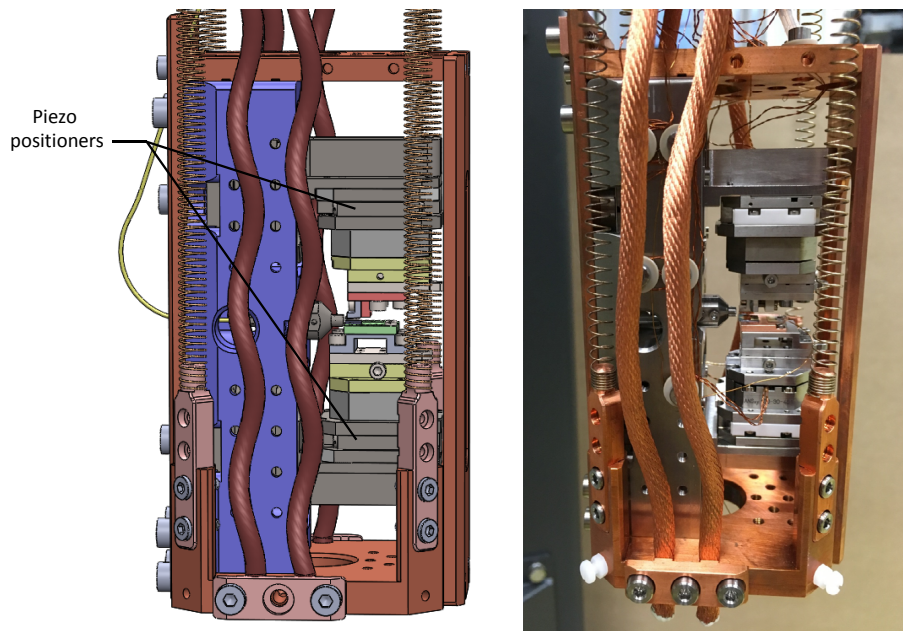


Figure B.2

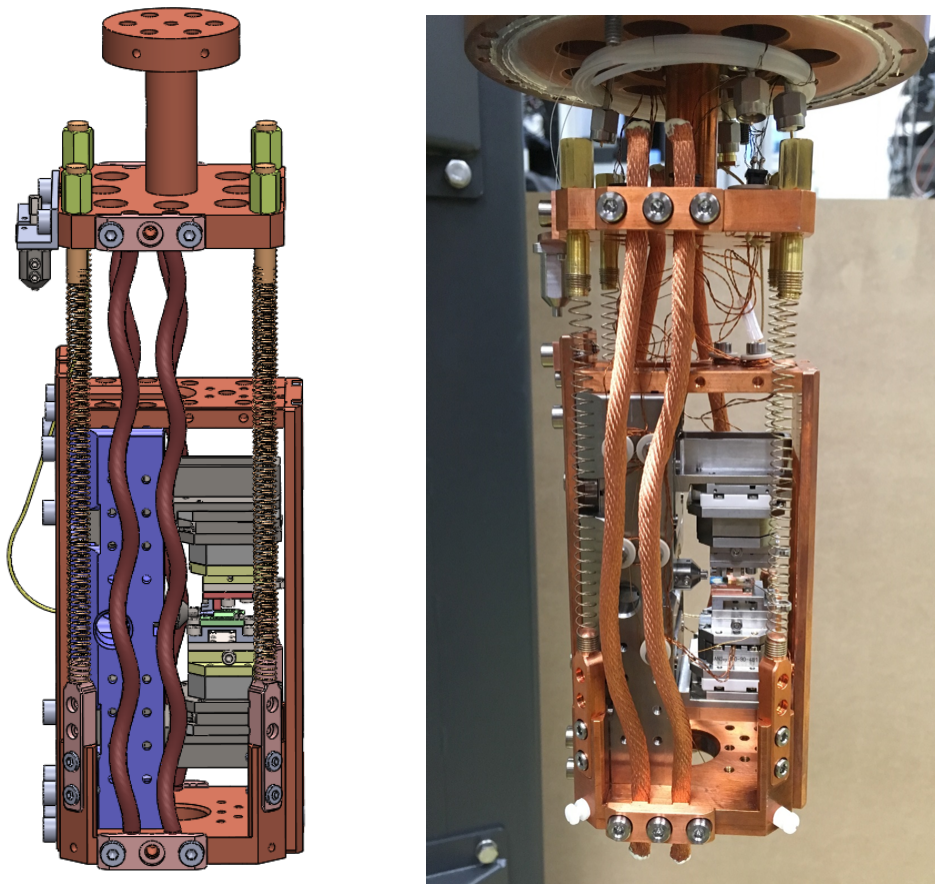


Figure B.3

References

- [1] Nichol, J. M., Hemesath, E. R., Lauhon, L. J. & Budakian, R. Displacement detection of silicon nanowires by polarization-enhanced fiber-optic interferometry. *Appl. Phys. Lett.* **93**, 193110 (2008). <http://aip.scitation.org/doi/10.1063/1.3025305>.
- [2] Nichol, J. M., Naibert, T. R., Hemesath, E. R., Lauhon, L. J. & Budakian, R. Nanoscale Fourier-Transform Magnetic Resonance Imaging. *Phys. Rev. X* **3**, 031016 (2013). <https://link.aps.org/doi/10.1103/PhysRevX.3.031016>.
- [3] Feng, X. L., He, R., Yang, P. & Roukes, M. L. Very High Frequency Silicon Nanowire Electromechanical Resonators. *Nano Lett.* **7**, 1953–1959 (2007). <http://dx.doi.org/10.1021/nl0706695>.
- [4] Poggio, M. Nanomechanics: Sensing from the bottom up. *Nature Nanotechnology* **8**, 482 (2013). <https://www.nature.com/articles/nnano.2013.124>.
- [5] Nichol, J. M., Hemesath, E. R., Lauhon, L. J. & Budakian, R. Nanomechanical detection of nuclear magnetic resonance using a silicon nanowire oscillator. *Phys. Rev. B* **85**, 054414 (2012). <https://link.aps.org/doi/10.1103/PhysRevB.85.054414>.
- [6] Nonnenmacher, M., O’Boyle, M. P. & Wickramasinghe, H. K. Kelvin probe force microscopy. *Appl. Phys. Lett.* **58**, 2921–2923 (1991). <http://aip.scitation.org/doi/10.1063/1.105227>.
- [7] Stipe, B. C., Mamin, H. J., Stowe, T. D., Kenny, T. W. & Rugar, D. Noncontact Friction and Force Fluctuations between Closely Spaced Bodies. *Phys. Rev. Lett.* **87**, 096801 (2001). <https://link.aps.org/doi/10.1103/PhysRevLett.87.096801>.
- [8] Montinaro, M. *et al.* Quantum Dot Opto-Mechanics in a Fully Self-Assembled Nanowire. *Nano Lett.* **14**, 4454–4460 (2014). <http://dx.doi.org/10.1021/nl501413t>.

- [9] Yeo, I. *et al.* Strain-mediated coupling in a quantum dot–mechanical oscillator hybrid system. *Nature Nanotechnology* **9**, 106 (2014). <https://www.nature.com/articles/nnano.2013.274>.
- [10] Treutlein, P., Genes, C., Hammerer, K., Poggio, M. & Rabl, P. Hybrid Mechanical Systems. In Aspelmeyer, M. (ed.) *Cavity Optomechanics, Quantum Science and Technology*, 327, 327–351 (Springer-Verlag, Berlin Heidelberg, 2014).
- [11] Kepesidis, K. V., Bennett, S. D., Portolan, S., Lukin, M. D. & Rabl, P. Phonon cooling and lasing with nitrogen-vacancy centers in diamond. *Phys. Rev. B* **88**, 064105 (2013). <https://link.aps.org/doi/10.1103/PhysRevB.88.064105>.
- [12] Auffèves, A. & Richard, M. Optical driving of macroscopic mechanical motion by a single two-level system. *Phys. Rev. A* **90**, 023818 (2014). <https://link.aps.org/doi/10.1103/PhysRevA.90.023818>.
- [13] Wilson-Rae, I., Zoller, P. & Imamolu, A. Laser Cooling of a Nanomechanical Resonator Mode to its Quantum Ground State. *Phys. Rev. Lett.* **92**, 075507 (2004). <https://link.aps.org/doi/10.1103/PhysRevLett.92.075507>.
- [14] Antonio, D., Zanette, D. H. & López, D. Frequency stabilization in nonlinear micromechanical oscillators. *Nature Communications* **3**, 806 (2012). <https://www.nature.com/articles/ncomms1813>.
- [15] Postma, H. W. C., Kozinsky, I., Husain, A. & Roukes, M. L. Dynamic range of nanotube- and nanowire-based electromechanical systems. *Appl. Phys. Lett.* **86**, 223105 (2005). <http://aip.scitation.org/doi/10.1063/1.1929098>.
- [16] Husain, A. *et al.* Nanowire-based very-high-frequency electromechanical resonator. *Appl. Phys. Lett.* **83**, 1240–1242 (2003). <http://aip.scitation.org/doi/10.1063/1.1601311>.
- [17] Villanueva, L. G. *et al.* Nonlinearity in nanomechanical cantilevers. *Phys. Rev. B* **87**, 024304 (2013). <https://link.aps.org/doi/10.1103/PhysRevB.87.024304>.
- [18] Lifshitz, R. & Cross, M. C. Nonlinear Dynamics of Nanomechanical and Micromechanical Resonators. In Schuster, H. G. (ed.) *Reviews of Nonlinear Dynamics and Complexity*, 1–52 (Wiley-VCH Verlag GmbH & Co. KGaA, 2008). <http://onlinelibrary.wiley.com/doi/10.1002/9783527626359.ch1/summary>.

- [19] Eichler, A. *et al.* Nonlinear damping in mechanical resonators made from carbon nanotubes and graphene. *Nature Nanotechnology* **6**, 339 (2011). <https://www.nature.com/articles/nnano.2011.71>.
- [20] Zaitsev, S., Shtempluck, O., Buks, E. & Gottlieb, O. Nonlinear damping in a micromechanical oscillator. *Nonlinear Dyn* **67**, 859–883 (2012). <https://link.springer.com/article/10.1007/s11071-011-0031-5>.
- [21] Moon, F. C. & Shaw, S. W. Chaotic vibrations of a beam with non-linear boundary conditions. *International Journal of Non-Linear Mechanics* **18**, 465–477 (1983). <http://www.sciencedirect.com/science/article/pii/0020746283900331>.
- [22] Tabaddor, M. Influence of nonlinear boundary conditions on the single-mode response of a cantilever beam. *International Journal of Solids and Structures* **37**, 4915–4931 (2000). <http://www.sciencedirect.com/science/article/pii/S0020768399001973>.
- [23] Nichol, J. M., Hemesath, E. R., Lauhon, L. J. & Budakian, R. Controlling the nonlinearity of silicon nanowire resonators using active feedback. *Appl. Phys. Lett.* **95**, 123116 (2009). <http://aip.scitation.org/doi/10.1063/1.3232232>.
- [24] Almog, R., Zaitsev, S., Shtempluck, O. & Buks, E. High intermodulation gain in a micromechanical Duffing resonator. *Appl. Phys. Lett.* **88**, 213509 (2006). <http://aip.scitation.org/doi/10.1063/1.2207490>.
- [25] Karabalin, R. B. *et al.* Signal Amplification by Sensitive Control of Bifurcation Topology. *Phys. Rev. Lett.* **106**, 094102 (2011). <https://link.aps.org/doi/10.1103/PhysRevLett.106.094102>.
- [26] Almog, R., Zaitsev, S., Shtempluck, O. & Buks, E. Noise Squeezing in a Nanomechanical Duffing Resonator. *Phys. Rev. Lett.* **98**, 078103 (2007). <https://link.aps.org/doi/10.1103/PhysRevLett.98.078103>.
- [27] Erbe, A. *et al.* Mechanical mixing in nonlinear nanomechanical resonators. *Appl. Phys. Lett.* **77**, 3102–3104 (2000). <http://aip.scitation.org/doi/10.1063/1.1324721>.
- [28] Gloppe, A. *et al.* Bidimensional nano-optomechanics and topological backaction in a non-conservative radiation force field. *Nature Nanotechnology* **9**, 920 (2014). <https://www.nature.com/articles/nnano.2014.189>.

- [29] Karabalin, R. B., Cross, M. C. & Roukes, M. L. Nonlinear dynamics and chaos in two coupled nanomechanical resonators. *Phys. Rev. B* **79**, 165309 (2009). <https://link.aps.org/doi/10.1103/PhysRevB.79.165309>.
- [30] Venstra, W. J., Westra, H. J. R. & van der Zant, H. S. J. Q-factor control of a microcantilever by mechanical sideband excitation. *Appl. Phys. Lett.* **99**, 151904 (2011). <http://aip.scitation.org/doi/10.1063/1.3650714>.
- [31] Mahboob, I. & Yamaguchi, H. Bit storage and bit flip operations in an electromechanical oscillator. *Nature Nanotechnology* **3**, 275 (2008). <https://www.nature.com/articles/nnano.2008.84>.
- [32] Yao, A. & Hikiyara, T. Logic-memory device of a mechanical resonator. *Appl. Phys. Lett.* **105**, 123104 (2014). <http://aip.scitation.org/doi/10.1063/1.4896272>.
- [33] Gil-Santos, E. *et al.* Nanomechanical mass sensing and stiffness spectrometry based on two-dimensional vibrations of resonant nanowires. *Nature Nanotechnology* **5**, 641 (2010). <https://www.nature.com/articles/mnano.2010.151>.
- [34] Lulla, K. J. *et al.* Nonlinear modal coupling in a high-stress doubly-clamped nanomechanical resonator. *New J. Phys.* **14**, 113040 (2012). <http://stacks.iop.org/1367-2630/14/i=11/a=113040>.
- [35] Truitt, P. A., Hertzberg, J. B., Altunkaya, E. & Schwab, K. C. Linear and nonlinear coupling between transverse modes of a nanomechanical resonator. *Journal of Applied Physics* **114**, 114307 (2013). <http://aip.scitation.org/doi/10.1063/1.4821273>.
- [36] Faust, T. *et al.* Nonadiabatic Dynamics of Two Strongly Coupled Nanomechanical Resonator Modes. *Phys. Rev. Lett.* **109**, 037205 (2012). <https://link.aps.org/doi/10.1103/PhysRevLett.109.037205>.
- [37] Flowers-Jacobs, N. E. *et al.* Fiber-cavity-based optomechanical device. *Appl. Phys. Lett.* **101**, 221109 (2012). <http://aip.scitation.org/doi/10.1063/1.4768779>.
- [38] Antoni, T. *et al.* Nonlinear mechanics with suspended nanomembranes. *EPL* **100**, 68005 (2012). <http://stacks.iop.org/0295-5075/100/i=6/a=68005>.

- [39] Eichler, A., del Álamo Ruiz, M., Plaza, J. A. & Bachtold, A. Strong Coupling between Mechanical Modes in a Nanotube Resonator. *Phys. Rev. Lett.* **109**, 025503 (2012). <https://link.aps.org/doi/10.1103/PhysRevLett.109.025503>.
- [40] Martin, Y., Abraham, D. W. & Wickramasinghe, H. K. High-resolution capacitance measurement and potentiometry by force microscopy. *Appl. Phys. Lett.* **52**, 1103–1105 (1988). <http://aip.scitation.org/doi/10.1063/1.99224>.
- [41] Gross, L. *et al.* Measuring the Charge State of an Adatom with Non-contact Atomic Force Microscopy. *Science* **324**, 1428–1431 (2009). <http://science.sciencemag.org/content/324/5933/1428>.
- [42] Henning, A. K. *et al.* Two-dimensional surface dopant profiling in silicon using scanning Kelvin probe microscopy. *Journal of Applied Physics* **77**, 1888–1896 (1995). <http://aip.scitation.org/doi/10.1063/1.358819>.
- [43] Dolde, F. *et al.* Electric-field sensing using single diamond spins. *Nat Phys* **7**, 459–463 (2011). <http://www.nature.com/nphys/journal/v7/n6/full/nphys1969.html>.
- [44] Yoo, M. J. *et al.* Scanning Single-Electron Transistor Microscopy: Imaging Individual Charges. *Science* **276**, 579–582 (1997). <http://science.sciencemag.org/content/276/5312/579>.
- [45] Martin, J. *et al.* Observation of electron–hole puddles in graphene using a scanning single-electron transistor. *Nature Physics* **4**, 144 (2008). <https://www.nature.com/articles/nphys781>.
- [46] Wagner, C. *et al.* Scanning Quantum Dot Microscopy. *Phys. Rev. Lett.* **115**, 026101 (2015). <https://link.aps.org/doi/10.1103/PhysRevLett.115.026101>.
- [47] Zimmerli, G., Eiles, T. M., Kautz, R. L. & Martinis, J. M. Noise in the Coulomb blockade electrometer. *Appl. Phys. Lett.* **61**, 237–239 (1992). <http://aip.scitation.org/doi/10.1063/1.108195>.
- [48] Crespo da Silva, M. R. M. & Glynn, C. C. Nonlinear Flexural-Flexural-Torsional Dynamics of Inextensional Beams. I. Equations of Motion. *Journal of Structural Mechanics* **6**, 437–448 (1978). <https://doi.org/10.1080/03601217808907348>.

- [49] Crespo da Silva, M. R. M. & Glynn, C. C. Nonlinear Flexural-Flexural-Torsional Dynamics of Inextensional Beams. II. Forced Motions. *Journal of Structural Mechanics* **6**, 449–461 (1978). <https://doi.org/10.1080/03601217808907349>.
- [50] Meirovitch, L. *Analytical Methods in Vibrations*. (Macmillan, New York, 1967). OCLC: 557777127.
- [51] Cleland, A. N. *Foundations of Nanomechanics: From Solid-State Theory to Device Applications* (Springer Science & Business Media, 2002).
- [52] Pai, P. F. & Nayfeh, A. H. Three-dimensional nonlinear vibrations of composite beams — I. Equations of motion. *Nonlinear Dyn* **1**, 477–502 (1990). <https://link.springer.com/article/10.1007/BF01856950>.
- [53] Nayfeh, A. H. & Mook, D. T. (eds.) *Nonlinear Oscillations* (Wiley-VCH Verlag GmbH, Weinheim, Germany, 1995). <http://doi.wiley.com/10.1002/9783527617586>.
- [54] Barger, V. & Olsson, M. G. *Classical Mechanics: A Modern Perspective* (McGraw-Hill, 1995), 2nd edition edn. OCLC: 473295114.
- [55] Lü, L. *et al.* Modeling a radio-frequency single-electron-transistor scanning probe. *Jpn. J. Appl. Phys.* **53**, 085001 (2014). <http://iopscience.iop.org/article/10.7567/JJAP.53.085001/meta>.
- [56] Colombo, C., Spirkoska, D., Frimmer, M., Abstreiter, G. & Fontcuberta i Morral, A. Ga-assisted catalyst-free growth mechanism of GaAs nanowires by molecular beam epitaxy. *Phys. Rev. B* **77**, 155326 (2008). <https://link.aps.org/doi/10.1103/PhysRevB.77.155326>.
- [57] Heiss, M. *et al.* Self-assembled quantum dots in a nanowire system for quantum photonics. *Nature Materials* **12**, 439 (2013). <https://www.nature.com/articles/nmat3557>.
- [58] Sarid, o. *Scanning Force Microscopy: With Applications to Electric, Magnetic and Atomic Forces*. Oxford Series in Optical and Imaging Sciences (Oxford University Press, Oxford, New York, 1994), revised edition edn.
- [59] Yasumura, K. Y. *et al.* Quality factors in micron- and submicron-thick cantilevers. *Journal of Microelectromechanical Systems* **9**, 117–125 (2000).

- [60] Yang, J., Ono, T. & Esashi, M. Energy dissipation in submicrometer thick single-crystal silicon cantilevers. *Journal of Microelectromechanical Systems* **11**, 775–783 (2002).
- [61] Dobosz, M., Usuda, T. & Kurosawa, T. Methods for the calibration of vibration pick-ups by laser interferometry: I. Theoretical analysis. *Meas. Sci. Technol.* **9**, 232 (1998). <http://stacks.iop.org/0957-0233/9/i=2/a=010>.
- [62] Hutter, C., Platz, D., Tholén, E. A., Hansson, T. H. & Haviiland, D. B. Reconstructing Nonlinearities with Intermodulation Spectroscopy. *Phys. Rev. Lett.* **104**, 050801 (2010). <https://link.aps.org/doi/10.1103/PhysRevLett.104.050801>.
- [63] Braakman, F. R. *et al.* Nonlinear motion and mechanical mixing in as-grown GaAs nanowires. *Appl. Phys. Lett.* **105**, 173111 (2014). <http://aip.scitation.org/doi/10.1063/1.4900928>.
- [64] Malatkar, P. Nonlinear Vibrations of Cantilever Beams and Plates (2003). <https://vtechworks.lib.vt.edu/handle/10919/28301>.
- [65] Westra, H. J. R., Poot, M., van der Zant, H. S. J. & Venstra, W. J. Nonlinear Modal Interactions in Clamped-Clamped Mechanical Resonators. *Phys. Rev. Lett.* **105**, 117205 (2010). <https://link.aps.org/doi/10.1103/PhysRevLett.105.117205>.
- [66] Sapmaz, S., Blanter, Y. M., Gurevich, L. & van der Zant, H. S. J. Carbon nanotubes as nanoelectromechanical systems. *Phys. Rev. B* **67**, 235414 (2003). <https://link.aps.org/doi/10.1103/PhysRevB.67.235414>.
- [67] Pfeiffer, O., Bennewitz, R., Baratoff, A., Meyer, E. & Grütter, P. Lateral-force measurements in dynamic force microscopy. *Phys. Rev. B* **65**, 161403 (2002). <https://link.aps.org/doi/10.1103/PhysRevB.65.161403>.
- [68] Giessibl, F. J., Herz, M. & Mannhart, J. Friction traced to the single atom. *PNAS* **99**, 12006–12010 (2002). <http://www.pnas.org/content/99/19/12006>.
- [69] Kawai, S., Kitamura, S.-i., Kobayashi, D. & Kawakatsu, H. Dynamic lateral force microscopy with true atomic resolution. *Appl. Phys. Lett.* **87**, 173105 (2005). <http://aip.scitation.org/doi/10.1063/1.2112203>.

- [70] Kawai, S., Sasaki, N. & Kawakatsu, H. Direct mapping of the lateral force gradient on Si(111)-(7x7). *Phys. Rev. B* **79**, 195412 (2009). <https://link.aps.org/doi/10.1103/PhysRevB.79.195412>.
- [71] Kawai, S. *et al.* Ultrasensitive detection of lateral atomic-scale interactions on graphite (0001) via bimodal dynamic force measurements. *Phys. Rev. B* **81**, 085420 (2010). <https://link.aps.org/doi/10.1103/PhysRevB.81.085420>.
- [72] Karabacak, D., Kouh, T., Huang, C. C. & Ekinici, K. L. Optical knife-edge technique for nanomechanical displacement detection. *Appl. Phys. Lett.* **88**, 193122 (2006). <http://aip.scitation.org/doi/10.1063/1.2203513>.
- [73] Rossi, N. *et al.* Vectorial scanning force microscopy using a nanowire sensor. *Nat Nano* **12**, 150–155 (2017). <http://www.nature.com/nano/journal/v12/n2/full/nnano.2016.189.html>.
- [74] Frimmer, M. & Novotny, L. The classical Bloch equations. *American Journal of Physics* **82**, 947–954 (2014). <http://aapt.scitation.org/doi/abs/10.1119/1.4878621>.
- [75] Sansa, M. *et al.* Frequency fluctuations in silicon nanoresonators. *Nature Nanotechnology* **11**, 552 (2016). <https://www.nature.com/articles/mnano.2016.19>.
- [76] Aspelmeyer, M., Kippenberg, T. J. & Marquardt, F. Cavity optomechanics. *Rev. Mod. Phys.* **86**, 1391–1452 (2014). <https://link.aps.org/doi/10.1103/RevModPhys.86.1391>.
- [77] Ding, L. *et al.* High Frequency GaAs Nano-Optomechanical Disk Resonator. *Phys. Rev. Lett.* **105**, 263903 (2010). <https://link.aps.org/doi/10.1103/PhysRevLett.105.263903>.
- [78] Nguyen, D. T. *et al.* Improved optomechanical disk resonator sitting on a pedestal mechanical shield. *New J. Phys.* **17**, 023016 (2015). <http://stacks.iop.org/1367-2630/17/i=2/a=023016>.
- [79] Claudon, J. *et al.* A highly efficient single-photon source based on a quantum dot in a photonic nanowire. *Nature Photonics* **4**, 174–177 (2010). <http://adsabs.harvard.edu/abs/2010NaPho...4..174C>.
- [80] Reimer, M. E. *et al.* Bright single-photon sources in bottom-up tailored nanowires. *Nature Communications* **3**, 737 (2012). <https://www.nature.com/articles/ncomms1746>.

- [81] He, Y.-M. *et al.* On-demand semiconductor single-photon source with near-unity indistinguishability. *Nature Nanotechnology* **8**, 213 (2013). <https://www.nature.com/articles/nnano.2012.262>.
- [82] Kuhlmann, A. V. *et al.* Transform-limited single photons from a single quantum dot. *Nature Communications* **6**, 8204 (2015). <https://www.nature.com/articles/ncomms9204>.
- [83] Somaschi, N. *et al.* Near-optimal single-photon sources in the solid state. *Nature Photonics* **10**, 340 (2016). <https://www.nature.com/articles/nphoton.2016.23>.
- [84] Ding, X. *et al.* On-Demand Single Photons with High Extraction Efficiency and Near-Unity Indistinguishability from a Resonantly Driven Quantum Dot in a Micropillar. *Phys. Rev. Lett.* **116**, 020401 (2016). <https://link.aps.org/doi/10.1103/PhysRevLett.116.020401>.
- [85] Munsch, M. *et al.* Dielectric GaAs Antenna Ensuring an Efficient Broadband Coupling between an InAs Quantum Dot and a Gaussian Optical Beam. *Phys. Rev. Lett.* **110**, 177402 (2013). <https://link.aps.org/doi/10.1103/PhysRevLett.110.177402>.
- [86] Bleuse, J. *et al.* Inhibition, Enhancement, and Control of Spontaneous Emission in Photonic Nanowires. *Phys. Rev. Lett.* **106**, 103601 (2011). <https://link.aps.org/doi/10.1103/PhysRevLett.106.103601>.
- [87] Stepanov, P. *et al.* Large and Uniform Optical Emission Shifts in Quantum Dots Strained along Their Growth Axis. *Nano Lett.* **16**, 3215–3220 (2016). <http://dx.doi.org/10.1021/acs.nanolett.6b00678>.
- [88] Kuhlmann, A. V. *et al.* A dark-field microscope for background-free detection of resonance fluorescence from single semiconductor quantum dots operating in a set-and-forget mode. *Review of Scientific Instruments* **84**, 073905 (2013). <http://aip.scitation.org/doi/10.1063/1.4813879>.
- [89] Nguyen, H. S. *et al.* Optically Gated Resonant Emission of Single Quantum Dots. *Phys. Rev. Lett.* **108**, 057401 (2012). <https://link.aps.org/doi/10.1103/PhysRevLett.108.057401>.
- [90] Kuhlmann, A. V. *et al.* Charge noise and spin noise in a semiconductor quantum device. *Nature Physics* **9**, 570 (2013). <https://www.nature.com/articles/nphys2688>.

- [91] Matthiesen, C., Stanley, M. J., Hugues, M., Clarke, E. & Atatüre, M. Full counting statistics of quantum dot resonance fluorescence. *Scientific Reports* **4**, 4911 (2014). <https://www.nature.com/articles/srep04911>.
- [92] Makhonin, M. N. *et al.* Waveguide Coupled Resonance Fluorescence from On-Chip Quantum Emitter. *Nano Lett.* **14**, 6997–7002 (2014). <http://dx.doi.org/10.1021/nl5032937>.
- [93] Jahn, J.-P. *et al.* An artificial Rb atom in a semiconductor with lifetime-limited linewidth. *Phys. Rev. B* **92**, 245439 (2015). <https://link.aps.org/doi/10.1103/PhysRevB.92.245439>.
- [94] de Assis, P.-L. *et al.* Strain-Gradient Position Mapping of Semiconductor Quantum Dots. *Phys. Rev. Lett.* **118**, 117401 (2017). <https://link.aps.org/doi/10.1103/PhysRevLett.118.117401>.
- [95] Kremer, P. E. *et al.* Strain-tunable quantum dot embedded in a nanowire antenna. *Phys. Rev. B* **90**, 201408 (2014). <https://link.aps.org/doi/10.1103/PhysRevB.90.201408>.
- [96] Lagoudakis, K. G. *et al.* Ultrafast coherent manipulation of trions in site-controlled nanowire quantum dots. *Optica, OPTICA* **3**, 1430–1435 (2016). <https://www.osapublishing.org/abstract.cfm?uri=optica-3-12-1430>.
- [97] Munsch, M. *et al.* Manipulation of the nuclear spin ensemble in a quantum dot with chirped magnetic resonance pulses. *Nature Nanotechnology* **9**, 671 (2014). <https://www.nature.com/articles/nnano.2014.175>.
- [98] Cadeddu, D. *et al.* A fiber-coupled quantum-dot on a photonic tip. *Appl. Phys. Lett.* **108**, 011112 (2016). <http://aip.scitation.org/doi/10.1063/1.4939264>.
- [99] Mermillod, Q. *et al.* Harvesting, Coupling, and Control of Single-Exciton Coherences in Photonic Waveguide Antennas. *Phys. Rev. Lett.* **116**, 163903 (2016). <https://link.aps.org/doi/10.1103/PhysRevLett.116.163903>.
- [100] Schlehahn, A. *et al.* An electrically driven cavity-enhanced source of indistinguishable photons with 61% overall efficiency. *APL Photonics* **1**, 011301 (2016). <http://aip.scitation.org/doi/10.1063/1.4939831>.

- [101] Michler, P. *et al.* A Quantum Dot Single-Photon Turnstile Device. *Science* **290**, 2282–2285 (2000). <http://science.sciencemag.org/content/290/5500/2282>.
- [102] Santori, C., Pelton, M., Solomon, G., Dale, Y. & Yamamoto, Y. Triggered Single Photons from a Quantum Dot. *Phys. Rev. Lett.* **86**, 1502–1505 (2001). <https://link.aps.org/doi/10.1103/PhysRevLett.86.1502>.
- [103] Moreau, E. *et al.* Single-mode solid-state single photon source based on isolated quantum dots in pillar microcavities. *Appl. Phys. Lett.* **79**, 2865–2867 (2001). <http://aip.scitation.org/doi/10.1063/1.1415346>.
- [104] Sangouard, N. & Zbinden, H. What are single photons good for? *Journal of Modern Optics* **59**, 1458–1464 (2012). <https://doi.org/10.1080/09500340.2012.687500>.
- [105] Schlehahn, A. *et al.* Operating single quantum emitters with a compact Stirling cryocooler. *Review of Scientific Instruments* **86**, 013113 (2015). <http://aip.scitation.org/doi/10.1063/1.4906548>.
- [106] Gérard, J. M. *et al.* Enhanced Spontaneous Emission by Quantum Boxes in a Monolithic Optical Microcavity. *Phys. Rev. Lett.* **81**, 1110–1113 (1998). <https://link.aps.org/doi/10.1103/PhysRevLett.81.1110>.
- [107] Lund-Hansen, T. *et al.* Experimental Realization of Highly Efficient Broadband Coupling of Single Quantum Dots to a Photonic Crystal Waveguide. *Phys. Rev. Lett.* **101**, 113903 (2008). <https://link.aps.org/doi/10.1103/PhysRevLett.101.113903>.
- [108] Dousse, A. *et al.* Controlled Light-Matter Coupling for a Single Quantum Dot Embedded in a Pillar Microcavity Using Far-Field Optical Lithography. *Phys. Rev. Lett.* **101**, 267404 (2008). <https://link.aps.org/doi/10.1103/PhysRevLett.101.267404>.
- [109] Claudon, J., Gregersen, N., Lalanne, P. & Gérard, J.-M. Harnessing light with photonic nanowires: Fundamentals and applications to quantum optics. *Chemphyschem* **14**, 2393–2402 (2013).
- [110] Gazzano, O. *et al.* Bright solid-state sources of indistinguishable single photons. *Nature Communications* **4**, 1425 (2013). <https://www.nature.com/articles/ncomms2434>.

- [111] Xu, X. *et al.* “Plug and play” single-photon sources. *Appl. Phys. Lett.* **90**, 061103 (2007). <http://aip.scitation.org/doi/10.1063/1.2437727>.
- [112] Haupt, F. *et al.* Fiber-connectorized micropillar cavities. *Appl. Phys. Lett.* **97**, 131113 (2010). <http://aip.scitation.org/doi/10.1063/1.3493187>.
- [113] Tiecke, T. G. *et al.* Efficient fiber-optical interface for nanophotonic devices. *Optica, OPTICA* **2**, 70–75 (2015). <https://www.osapublishing.org/abstract.cfm?uri=optica-2-2-70>.
- [114] Cuche, A. *et al.* Near-field optical microscopy with a nanodiamond-based single-photon tip. *Opt. Express, OE* **17**, 19969–19980 (2009). <https://www.osapublishing.org/abstract.cfm?uri=oe-17-22-19969>.
- [115] Cuche, A., Mollet, O., Drezet, A. & Huan, S. “Deterministic” Quantum Plasmonics. *Nano Lett.* **10**, 4566–4570 (2010). <http://dx.doi.org/10.1021/nl102568m>.
- [116] Vamivakas, A. N. *et al.* Nanoscale Optical Electrometer. *Phys. Rev. Lett.* **107**, 166802 (2011). <https://link.aps.org/doi/10.1103/PhysRevLett.107.166802>.
- [117] Munsch, M. & Cadeddu, D. Quantum fiber-pigtails. https://www.youtube.com/watch?v=E_A3y_K3kRw&feature=youtu.be.
- [118] Munsch, M. *et al.* Continuous-wave versus time-resolved measurements of Purcell factors for quantum dots in semiconductor microcavities. *Phys. Rev. B* **80**, 115312 (2009). <https://link.aps.org/doi/10.1103/PhysRevB.80.115312>.
- [119] Friedler, I. *et al.* Solid-state single photon sources: The nanowire antenna. *Opt. Exp.* **17**, 2095–2110 (2009). <https://www.osapublishing.org/abstract.cfm?uri=oe-17-4-2095>.
- [120] Barthel, C. *et al.* Fast sensing of double-dot charge arrangement and spin state with a radio-frequency sensor quantum dot. *Phys. Rev. B* **81**, 161308 (2010). <http://link.aps.org/doi/10.1103/PhysRevB.81.161308>.
- [121] Arnold, C. *et al.* Cavity-Enhanced Real-Time Monitoring of Single-Charge Jumps at the Microsecond Time Scale. *Phys. Rev. X* **4**, 021004 (2014). <https://link.aps.org/doi/10.1103/PhysRevX.4.021004>.

- [122] Houel, J. *et al.* Probing Single-Charge Fluctuations at a GaAs/AlAs Interface Using Laser Spectroscopy on a Nearby InGaAs Quantum Dot. *Phys. Rev. Lett.* **108**, 107401 (2012). <http://link.aps.org/doi/10.1103/PhysRevLett.108.107401>.
- [123] Fry, P. W. *et al.* Inverted Electron-Hole Alignment in InAs-GaAs Self-Assembled Quantum Dots. *Phys. Rev. Lett.* **84**, 733–736 (2000). <https://link.aps.org/doi/10.1103/PhysRevLett.84.733>.
- [124] Schulhauser, C. *et al.* Magneto-optical properties of charged excitons in quantum dots. *Phys. Rev. B* **66**, 193303 (2002). <https://link.aps.org/doi/10.1103/PhysRevB.66.193303>.
- [125] Stavarache, V. *et al.* Control of quantum dot excitons by lateral electric fields. *Appl. Phys. Lett.* **89**, 123105 (2006). <http://aip.scitation.org/doi/10.1063/1.2345233>.
- [126] Vogel, M. M. *et al.* Influence of lateral electric fields on multiexcitonic transitions and fine structure of single quantum dots. *Appl. Phys. Lett.* **91**, 051904 (2007). <http://aip.scitation.org/doi/10.1063/1.2761522>.
- [127] Warburton, R. J. *et al.* Giant permanent dipole moments of excitons in semiconductor nanostructures. *Phys. Rev. B* **65**, 113303 (2002). <https://link.aps.org/doi/10.1103/PhysRevB.65.113303>.
- [128] Prechtel, J. H. *et al.* Electrically tunable hole g factor of an optically active quantum dot for fast spin rotations. *Phys. Rev. B* **91**, 165304 (2015). <https://link.aps.org/doi/10.1103/PhysRevB.91.165304>.
- [129] Finley, J. J. *et al.* Quantum-confined Stark shifts of charged exciton complexes in quantum dots. *Phys. Rev. B* **70**, 201308 (2004). <https://link.aps.org/doi/10.1103/PhysRevB.70.201308>.
- [130] Faraon, A., Majumdar, A., Kim, H., Petroff, P. & Vučković, J. Fast Electrical Control of a Quantum Dot Strongly Coupled to a Photonic-Crystal Cavity. *Phys. Rev. Lett.* **104**, 047402 (2010). <https://link.aps.org/doi/10.1103/PhysRevLett.104.047402>.
- [131] Munsch, M. *et al.* Resonant driving of a single photon emitter embedded in a mechanical oscillator. *Nature Communications* **8**, 76 (2017). <https://www.nature.com/articles/s41467-017-00097-3>.
- [132] Santamore, D. H., Doherty, A. C. & Cross, M. C. Quantum nondemolition measurement of Fock states of mesoscopic mechanical oscillators.

- Phys. Rev. B* **70**, 144301 (2004). <https://link.aps.org/doi/10.1103/PhysRevB.70.144301>.
- [133] Mayer, B. *et al.* Lasing from individual GaAs-AlGaAs core-shell nanowires up to room temperature. *Nature Communications* **4**, 2931 (2013). <https://www.nature.com/articles/ncomms3931>.
- [134] Stepanov, P. *et al.* Highly directive and Gaussian far-field emission from “giant” photonic trumpets. *Appl. Phys. Lett.* **107**, 141106 (2015). <http://aip.scitation.org/doi/10.1063/1.4932574>.

Curriculum Vitae

Davide Cadeddu

Department of Physics
University of Basel
Klingelbergstrasse 82
CH-4056 Basel, Switzerland

Birth: December 18th 1987 in Milano, Italy

Citizenship: Italian

davide.cadeddu@unibas.ch

Education

2013 - 2018 Ph.D. in Experimental Physics
University of Basel, Switzerland
Advisor: Prof. Martino Poggio

2009 - 2012 M.Sc. in Physics Engineering
Politecnico di Milano, Italy
Thesis: Nanofabrication and characterization of graphene field effect transistor exhibiting over-unity voltage gain.
Advisor: Prof. Roman Sordan

2006 - 2009 B.Sc. in Physics Engineering
Politecnico di Milano, Italy
Thesis: Writing waveguides in fused silica with femtosecond laser pulses.
Advisor: Prof. Roberto Osellame

List of Publications

2014 Boundary between the thermal and statistical polarization regimes in a nuclear spin ensemble

Herzog, B. E., Cadeddu, D., Xue, F., Peddibhotla, P., and Poggio M., *Appl. Phys. Lett.*, **105** 043112 (2014).

Nonlinear motion and mechanical mixing in as-grown GaAs nanowires

Braakman, F. R., Cadeddu, D., Tütüncüoğlu, G., Matteini, F., Ruffer, D., Fontcuberta i Morral, A., and Poggio, M., *Appl. Phys. Lett.* **105** 173111 (2014).

2016 A fiber-coupled quantum-dot on a photonic tip

Cadeddu, D., Tessier, J., Braakman, F. R., Gregersen, N., Stepanov, P., Gerard, J-M., Claudon, J., Warburton, R., Poggio, M., and Munsch, M., *Appl. Phys. Lett.* **108** 011112 (2016).

Time-resolved nonlinear coupling between orthogonal flexural modes of a pristine GaAs nanowire

Cadeddu, D., Braakman, F. R., Tütüncüoğlu, G., Matteini, F., Ruffer, D., Fontcuberta i Morral, A., and Poggio, M., *Nano Lett.* **16** 926931 (2016).

2017 Vectorial scanning force microscopy using a nanowire sensor

Rossi, N., Braakman, F. R., Cadeddu, D., Vasyukov, D., Tütüncüoğlu, G., Fontcuberta i Morral, A., and Poggio, M., *Nat. Nanotechnol.* **12** 150-155 (2017).

Resonant driving of a single photon emitter embedded in a mechanical oscillator

Munsch, M., Kuhlmann, A. V., Cadeddu, D., Gerard, J-M., Claudon, J., Poggio, M., and Warburton, R. J., *Nat. Commun.* **8** 76 (2017).

Electric-field sensing with a scanning fiber-coupled quantum dot

Cadeddu, D., Munsch, M., Rossi, N., Gerard, J-M., Claudon, J., Warburton, R., and Poggio, M., *Phys. Rev. Applied* **8** 031002 (2017).

Acknowledgments

Coming to the end, it comes natural to look back to the journey that lead to writing this last pages. This is the occasion to show my gratitude to all the people that accompanied me through my PhD, contributing to make it a unique and special experience.

First of all I would like to thank Martino, for the brilliant guidance over all these years, always pointing in the right direction and helping getting over each and every possible obstacle. I am particularly thankful for his incredible ability to create a fantastic environment to work in.

I thank Prof. Christian Degen, for accepting to be part of my defense committee and dedicating his time to review my thesis.

My appreciation goes to the Swiss Nanoscience Institute, not only for funding my PhD but also for the organization, making possible to meet other great students and even good friends.

I am truly grateful to all my collaborators, to the group of Anna Fontcuberta i Morral at EPFL and in particular to Gozde for providing the nanowires samples. To Richard Warburton and Jean Tessier in Basel, Julien Claudon and Jean-Michel Gerard in Grenoble for their brilliant scientific insight. To Mathieu, for starting a wonderful collaboration that lead to a big portion of this work and his stunning help during and after the experiments.

Of course all this work would have not been possible without the help of the mechanical and electronic workshops. A special thanks here goes to Sascha Martin, for his precious advise and patience in the design and realization of our microscope.

I would like to thank each member of the PoggioLab with whom I crossed paths, shared knowledge and good times. Thanking, probably in order of appearance: Michele, that introduced me to Lab and being my survival guide in the Basler life. Dennis, for all the laughs, all the beers and all the nights out. Arne with whom I could share my passion for sports and music (and a sprinkle of dark humour). Ben, without whom I would probably be still look-

ing for a place to sleep. Andrea, for her helpfulness and unlimited resources. Floris, with whom I spent a scary amount of time in the first half of my PhD, for all the results obtained together, from the ones in the Lab to the ones in smelliest climbing hall that has ever existed, trying to be serious only when strictly necessary. Denis, for his help realizing the NW microscope, the first of many new systems. Boris, for the good times on the beach court, and for never giving up trying to teach me the wonders of the German language, even if sometimes by means of questionable music. Marcus, that introduced me to squash and to love FCB. A exceptional thanks goes to Nicola, that brought an incredible spark to me and the whole group, for his availability, always making me laugh and helping me more than he can imagine, inside and outside the Lab. Getting to the more recent additions, I would like to thank the other magic Squid guys, Lorenzo and Giulio for all the late aperos in the office. Thanks to the new forces that also represent the future of the group: Panos, Simon, Thibaud, David, and Hinrich, wishing them good luck in making the PoggioLab great again.

Cheers to Jacek and Miguel for corresponding and emphasizing that addiction for snow, and making me always crave for the weekend and for the next shred time together.

I want to shout an enormous thanks to all the extraordinary friends across the border, Paolo, Marco, Giammo, Mez e Corbe, for making me feel like I actually never left Italy.

I am truly thankful to who has been beside me from the beginning, but had to leave and to who joined, even if it was right at the end.

Last, but definitely not least, I want to show all my gratitude to my entire family for their endless love and support, that seems to never stop growing.